

<sup>1</sup> SEARCH FOR  $t\bar{t}Z' \rightarrow t\bar{t}t\bar{t}$  PRODUCTION IN THE MULTILEPTON FINAL STATE IN  
<sup>2</sup>  $pp$  COLLISIONS AT  $\sqrt{s} = 13$  TEV WITH THE ATLAS DETECTOR

<sup>3</sup> By

<sup>4</sup> Hieu Le

<sup>5</sup> A DISSERTATION

<sup>6</sup> Submitted to  
<sup>7</sup> Michigan State University  
<sup>8</sup> in partial fulfillment of the requirements  
<sup>9</sup> for the degree of

<sup>10</sup> Physics — Doctor of Philosophy

<sup>11</sup> 2025

12

## ABSTRACT

13 This dissertation presents a search for a new beyond-the-Standard-Model (BSM) particle  
14 at the Large Hadron Collider (LHC). Many BSM models predict a new heavy vector boson  
15 ( $Z'$ ) that couples primarily to the top quark in both production and decay (topophilic). The  
16 search is performed in multilepton events consistent with four-top-quark ( $t\bar{t}t\bar{t}$ ) production,  
17 due to the distinctive signature of the multilepton final states and its robustness against  
18 common background processes at the LHC. Analysis data was collected by the ATLAS  
19 detector from 2015 to 2018, using proton-proton collisions at the LHC at a center-of-mass  
20 energy of 13 TeV. No statistically significant deviation from Standard Model predictions is  
21 observed. Exclusion limits are set on the production cross section of the targeted topophilic  
22 particle in the mass range between 1 TeV and 3 TeV.

## ACKNOWLEDGMENTS

24        First and foremost, I am deeply grateful for my dissertation advisor and P.I, Professor  
25    Reinhard Schwienhorst, for his support, guidance and tolerance as part of my role in ATLAS  
26    and my doctoral program at Michigan State. Reinhard is the primary driving force in many  
27    exciting opportunities that I've had the chance to experience, and he also provides much-  
28    appreciated support both in knowledge and wisdom in times of need. I am incredibly thankful  
29    that Reinhard is one of the people that plays a part in who I am today.

30        I would like to express sincere gratitude to one of our postdocs in the MSU ATLAS  
31    group, Binbin Dong, who I closely worked with within ATLAS. Binbin is a massive source  
32    of support for physics, technical and ATLAS-specific knowledge that played a pivotal role  
33    during my training with ATLAS, during the analysis in this dissertation, and during my  
34    time at CERN. I would have never been able to find my way through without her help.

35        I am also extremely thankful for the MSU ATLAS group, in particular Professors Wade  
36    Fisher and Daniel Hayden, for their guidance and feedback on my professional and per-  
37    sonal endeavors which helped immensely in my development both scientifically and socially.  
38    I thank Rongqian Qian and Jason Gombas, my fellow advisees that offered great ideas,  
39    knowledge and friendship. I would like to thank Julia Hinds, Stergios Kazakos and Pratik  
40    Kafle for their support and companionship during my time at CERN. I also thank former and  
41    presents members of our group that I've had the pleasure to work with: Joey Huston, Jos  
42    Gabriel Reyes Rivera, Cecilia Imthurn, Xinfei Huang, Ahmed Tarek, Kyle Fielman, Robert  
43    Les and Trisha Farooque. It was a wonderful experience being part of the MSU ATLAS  
44    group and I hope our group continues to grow, even if it makes scheduling weekly meetings  
45    for everyone that much harder.

46 I would like to express my gratitude to my dissertation committee members, Professors  
47 Reinhard Schwienhorst, Johannes Pollanen, Wade Fisher, Remco Zegers and Yuying Xie, for  
48 their guidance, patience and commitment to my growth and success as a researcher and a  
49 person.

50 It has been a pleasure to work with the many outstanding people in ATLAS, especially  
51 the BSM multi-top analysis team. I would like to thank Philipp Gadow, Krisztian Peters,  
52 Frédéric Déliot and Neelam Kumari for their dedication and commitment to fostering a  
53 successful and fruitful collaboration. I also thank Meng-Ju Tsai, Hui-Chi Lin, Thomas  
54 Nommensen, Jianming Qian, Quake Qin, Tomke Schröer, Xilin Wang, Helena Gomez and  
55 Daniela Paredes for their tireless efforts in the analysis. I am truly glad to have had the  
56 chance to work with all of you.

57 Special thanks to my fellow graduate students that I have had the chance to befriend  
58 during my doctoral journey: Daniel Lay, Grayson Perez, Jordan Purcell, Eric Flynn, Isabella  
59 Molina, Mo Hassan, Cavan Maher and Hannah Berg. You all taught me a lot more than I  
60 could ever imagine and helped me more than I could ever asked for, and I look forward to  
61 see where we go from here.

62 Finally, I would like to thank my family, to whom this dissertation is dedicated: my  
63 spouse Allen Sechrist, for encouraging me tirelessly everyday and always being there for me  
64 even when I can't be there for myself; my cat Eddie, for being the best cat anyone could ask  
65 for; my brother Hien Le, my dad Bac Le, and my mom Thuy Cao, for their endless love and  
66 support. Thank you for being the reason that I am where I am today.

## TABLE OF CONTENTS

|     |  |     |
|-----|--|-----|
| 67  | <b>List of Tables . . . . .</b>  | vii |
| 68  | <b>List of Figures . . . . .</b>   | ix  |
| 69  | <b>KEY TO ABBREVIATIONS . . . . .</b>  | xii |
| 70  | <b>Chapter 1. Introduction . . . . .</b>   | 1   |
| 71  | <b>Chapter 2. Theoretical Overview . . . . .</b>                                   | 5   |
| 72  | 2.1 The Standard Model . . . . .   | 5   |
| 73  | 2.1.1 Elementary particles . . . . .   | 5   |
| 74  | 2.1.2 Mathematical formalism . . . . .   | 9   |
| 75  | 2.1.2.1 Quantum chromodynamics . . . . .   | 10  |
| 76  | 2.1.2.2 Electroweak theory . . . . .   | 11  |
| 77  | 2.1.2.3 Higgs mechanism . . . . .  | 14  |
| 78  | 2.2 Beyond the Standard Model: $t\bar{t}Z' \rightarrow t\bar{t}t\bar{t}$ . . . . . | 17  |
| 79  | 2.2.1 Top-philic vector resonance . . . . .  | 17  |
| 80  | 2.2.2 Production channels . . . . .  | 19  |
| 81  | 2.2.3 Decay modes . . . . .  | 20  |
| 82  | <b>Chapter 3. LHC &amp; ATLAS Experiment . . . . .</b>                             | 22  |
| 83  | 3.1 The Large Hadron Collider . . . . .  | 22  |
| 84  | 3.1.1 Overview . . . . .   | 22  |
| 85  | 3.1.2 LHC operations . . . . .   | 24  |
| 86  | 3.1.3 Physics at the LHC . . . . .   | 25  |
| 87  | 3.2 The ATLAS detector . . . . .   | 25  |
| 88  | 3.2.1 Inner detector . . . . .   | 28  |
| 89  | 3.2.2 Calorimeter systems . . . . .  | 29  |
| 90  | 3.2.3 Muon spectrometer . . . . .  | 31  |
| 91  | 3.2.4 Trigger & data acquisition . . . . .   | 33  |
| 92  | <b>Chapter 4. Particle Reconstruction &amp; Identification . . . . .</b>           | 34  |
| 93  | 4.1 Primary reconstruction . . . . .   | 34  |
| 94  | 4.1.1 Tracks . . . . .   | 34  |
| 95  | 4.1.2 Vertices . . . . .   | 35  |
| 96  | 4.1.3 Topological clusters . . . . .   | 36  |
| 97  | 4.2 Jets . . . . .   | 37  |
| 98  | 4.2.1 Jet reconstruction . . . . .   | 38  |
| 99  | 4.2.2 Flavor tagging . . . . .   | 39  |
| 100 | 4.3 Leptons . . . . .  | 43  |
| 101 | 4.3.1 Electrons . . . . .  | 43  |
| 102 | 4.3.2 Muons . . . . .  | 46  |

|     |  |   |           |
|-----|--|---|-----------|
| 103 | 4.4  | Missing transverse momentum . . . . .                     | 48        |
| 104 | 4.5  | Overlap removal . . . . .                                 | 49        |
| 105 | 4.6  | Object definition . . . . .                               | 50        |
| 106 | <b>Chapter 5. Data &amp; Simulated Samples</b> | . . . . .   | <b>51</b> |
| 107 | 5.1  | Data samples . . . . .                                    | 51        |
| 108 | 5.2  | Monte Carlo samples . . . . .                             | 51        |
| 109 | 5.2.1  | $t\bar{t}Z'$ signal samples . . . . .                     | 52        |
| 110 | 5.2.2  | Background samples . . . . .                              | 54        |
| 111 | <b>Chapter 6. Analysis Strategy</b>            | . . . . .   | <b>59</b> |
| 112 | 6.1  | Event selection . . . . .                                 | 59        |
| 113 | 6.1.1  | Event categorization . . . . .                            | 60        |
| 114 | 6.2  | Analysis regions . . . . .                                | 61        |
| 115 | 6.2.1  | Signal regions . . . . .                                  | 63        |
| 116 | 6.2.2  | Control regions . . . . .                                 | 64        |
| 117 | 6.3  | Background estimation . . . . .                           | 67        |
| 118 | 6.3.1  | Template fitting for fake/non-prompt estimation . . . . . | 69        |
| 119 | 6.3.2  | Charge misidentification data-driven estimation . . . . . | 69        |
| 120 | 6.3.3  | $t\bar{t}W$ background data-driven estimation . . . . .   | 71        |
| 121 | <b>Chapter 7. Systematic Uncertainties</b>     | . . . . .   | <b>74</b> |
| 122 | 7.1  | Experimental uncertainties . . . . .                      | 74        |
| 123 | 7.1.1  | Luminosity & pile-up reweighting . . . . .                | 74        |
| 124 | 7.1.2  | Leptons . . . . .   | 74        |
| 125 | 7.1.3  | Jets . . . . .  | 75        |
| 126 | 7.1.4  | Missing transverse energy . . . . .                       | 77        |
| 127 | 7.2  | Modeling uncertainties . . . . .                          | 78        |
| 128 | 7.2.1  | Signal and irreducible background uncertainties . . . . . | 78        |
| 129 | 7.2.2  | Reducible background uncertainties . . . . .              | 80        |
| 130 | <b>Chapter 8. Results</b>                      | . . . . .   | <b>82</b> |
| 131 | 8.1  | Statistical interpretation . . . . .                      | 82        |
| 132 | 8.1.1  | Profile likelihood fit . . . . .                          | 82        |
| 133 | 8.1.2  | Exclusion limit . . . . .                                 | 85        |
| 134 | 8.2  | Fit results . . . . .                                     | 87        |
| 135 | <b>Chapter 9. Summary</b>                      | . . . . .   | <b>97</b> |
| 136 | <b>References</b>                              | . . . . .   | <b>99</b> |

# <sup>137</sup> List of Tables

|  |   |    |
|--|---|----|
| <sup>138</sup> 137   | Table 4.1: Overlap removal process for this analysis, applied sequentially from top to bottom. . . . .  | 49 |
| <sup>140</sup> 141   | Table 4.2: Summary of object selection criteria used in this analysis. $\ell_0$ refers to the leading lepton in the event. . . . .  | 50 |
| <sup>142</sup> 143   | Table 5.1: Summary of all HLT triggers used in this analysis. Events are required to pass at least one trigger. . . . .   | 52 |
| <sup>144</sup> 145<br><sup>146</sup><br><sup>147</sup>                                     | Table 5.2: Summary of all Monte-Carlo samples used in this analysis. $V$ refers to an EW ( $W^\pm/Z/\gamma^*$ ) or Higgs boson. Matrix element (ME) order refers to the order in QCD of the perturbative calculation. Tune refers to the underlying-event tune of the parton shower (PS) generator. . . . .   | 53 |
| <sup>148</sup> 149<br><sup>150</sup><br><sup>151</sup><br><sup>152</sup><br><sup>153</sup> | Table 6.1: Definitions of signal, control and validation regions (VR) used in this analysis. $N_{\text{jets}}$ and $N_b$ refers to the number of jets and number of $b$ -tagged jets respectively. $\ell_1$ refers to the leading lepton, $\ell_2$ refers to the subleading lepton and so on. $H_T$ refers to the $p_T$ scalar sum of all leptons and jets in the event. $m_{\ell\ell}$ refers to the dilepton invariant mass, which must not coincide with the $Z$ -boson mass range of 81-101 GeV for SS2L+3L events. . . . . | 62 |
| <sup>154</sup> 155   | Table 6.2: Definitions of SR sub-regions. Events are sorted into different sub-regions based on the number of $b$ -tagged jets and leptons present. . . . .   | 63 |
| <sup>156</sup>   | Table 6.3: List of possible assigned values for DFCAA. . . . .  | 66 |
| <sup>157</sup> 158<br><sup>159</sup><br><sup>160</sup>                                     | Table 8.1: Normalization factors for backgrounds with dedicated CRs, obtained from a simultaneous fit in all CRs and SR under the background-only hypothesis. The nominal pre-fit value is 1 for all NFs and 0 for the scaling factors $a_0$ and $a_1$ . Uncertainties shown include both statistical and systematic uncertainties.   | 89 |



# List of Figures

|     |   |    |
|-----|---|----|
| 174 | Figure 2.1: Particles within the SM and their properties. . . . .   | 6  |
| 176 | Figure 2.2: Feynman diagram for $t\bar{t}$ production and subsequent decay processes. Top quark decays into a $W$ -boson and $b$ -quarks, and $W$ -boson can decay to a $q\bar{q}$ or a $\ell\nu_\ell$ pair. . . . .  | 8  |
| 179 | Figure 2.3: Illustration of a common representation of the Higgs potential. Before SSB, the ground state $\phi(0)$ is located at A which is symmetric with respect to the potential. A perturbation to this state fixes the ground state energy $ \phi(0) ^2$ to a particular value at B, "spontaneously" breaking the symmetry and degeneracy in $ \phi(0) ^2$ . . . . . | 15 |
| 184 | Figure 2.4: Feynman diagrams for tree level $Z'$ production in association with (a) $t\bar{t}$ , (b) $tj$ (light quark) and (c) $tW$ , decaying to final states containing (a) $t\bar{t}t\bar{t}$ or (b)(c) $t\bar{t}t$ . . . . .   | 19 |
| 187 | Figure 2.5: Theoretical $t\bar{t}Z'$ production cross-section times $Z' \rightarrow t\bar{t}$ branching ratio as a function of the $Z'$ mass at LO in QCD coupling to top with $c_t = 1$ under a simplified top-philic model. . . . .   | 20 |
| 190 | Figure 2.6: Branching ratios for $t\bar{t}t\bar{t}$ decay. The same-sign dilepton and multilepton channels together forms the SSML channel. . . . .   | 21 |
| 192 | Figure 3.1: The full CERN accelerator complex as of 2022. . . . .   | 23 |
| 193 | Figure 3.2: Current and future timeline of LHC operations as of 2025 with corresponding center-of-mass energies and projected integrated luminosities. . .  | 24 |
| 195 | Figure 3.3: Summary of predicted and measured cross-section for SM processes at the LHC at different center-of-mass energies . . . . .  | 26 |
| 197 | Figure 3.4: A cross section slice of the ATLAS detector showing different subsystems along with visualization of different types of particles traveling through the detector . . . . .  | 27 |

|     |  |    |
|-----|--|----|
| 200 | Figure 3.5: Cutaway illustration of the inner detector along with its subsystems. . . . .  | 28 |
| 201 | Figure 3.6: Cutaway illustration of the calorimeter system including the EM, hadronic<br>202 and LAr forward calorimeters . . . . .  | 30 |
| 203 | Figure 4.1: Stages of topo-cluster formation corresponding to each threshold. In (a),<br>204 proto-clusters are seeded from cells with adequate signal significance $\zeta_{\text{cell}}^{\text{EM}}$ .<br>205 The clusters are further merged and split in (b) according to a predefined<br>206 cluster growth threshold. The process stops in (c) when all sufficiently<br>207 significant signal hits have been matched to a cluster. . . . .   | 37 |
| 208 | Figure 4.2: Jet energy scale calibration sequence for EM-scale jets. . . . .   | 39 |
| 209 | Figure 4.3: Overview of the GN2 architecture. The number of jet and track features<br>210 are represented by $n_{\text{jf}}$ and $n_{\text{tf}}$ respectively. The global jet representation<br>211 and track embeddings output by the Transformer encoder are used as<br>212 inputs for three task-specific networks. . . . .   | 41 |
| 213 | Figure 4.4: The $c$ -, light- and $\tau$ -jet rejection rate as a function of $b$ -tagging efficiency<br>214 for GN2 and DL1d using (a) jets in the $t\bar{t}$ sample, and (b) jets in the $Z'$<br>215 sample. The performance ratios of GN2 to DL1d are shown in the bottom<br>216 panels. . . . .  | 42 |
| 217 | Figure 6.1: Post-fit background composition in each analysis region and sub-region.<br>218 The fit was performed using ideal pseudo-datasets (Asimov data) in the SR. 61   |    |
| 219 | Figure 6.2: Pre-fit kinematic distributions and event compositions in the inclusive<br>220 SR for (a) $H_T$ i.e. scalar sum of $p_T$ of all objects in the event, (b) jet<br>221 multiplicity, (c) $b$ -jet multiplicity, (d) leading lepton $p_T$ . The shaded band<br>222 represents the uncertainty in the total distribution. The first and last bins<br>223 of each distribution contains underflow and overflow events respectively. . . . . | 65 |
| 224 | Figure 6.3: Feynman diagram for one possible $t\bar{t}W$ decay process with similar SS2L<br>225 lepton signature to the $t\bar{t}Z'$ signal. Usually only two $b$ -jets are present due<br>226 to CKM suppression of $b$ -quark production from $W$ -boson decays; this is<br>227 enough to allow $t\bar{t}W$ decays to enter and contaminate the SR. . . . .  | 68 |
| 228 | Figure 6.4: Charge flip rate calculated for SR and CR $t\bar{t}W$ in bins of $ \eta $ and $p_T$ . . . . .  | 71 |
| 229 | Figure 7.1: Combined QmisID uncertainty rate for SR in bins of $ \eta $ and $p_T$ . . . . .  | 81 |

|     |  |    |
|-----|--|----|
| 230 | Figure 8.1: Example of an exclusion limit graph. The solid (dotted) line represents<br>231 the observed (expected) upper limits as a function of the $Z'$ mass at<br>232 95% CL on the cross-section of $pp \rightarrow t\bar{t}Z'$ production times the $Z' \rightarrow$<br>233 $t\bar{t}$ branching ratio. The solid blue line represents the theoretical signal<br>234 cross-section with $c_t = 1$ at LO in QCD [74]. The green and yellow<br>235 bands represent the 68% ( $\pm 1\sigma$ ) and 95% ( $\pm 2\sigma$ ) confidence intervals for the<br>236 expected upper limits. Values of $\mu$ within the region above the observed<br>237 limit is excluded under the current model. Masses below the $m_{Z'}$ value at<br>238 which the observed limit intersect the theoretical cross section are excluded. | 86 |
| 239 | Figure 8.2: Comparison between data and post-fit prediction for the discriminant ob-<br>240 servable in each CR. Distributions shown are obtained from the fit using<br>241 the $t\bar{t}Z'$ signal sample with $m_{Z'} = 2$ TeV. The lower panel shows the<br>242 ratio between data and post-fit predictions. The shaded band represents<br>243 the total uncertainty on the fit. The dashed line represents the pre-fit<br>244 distribution. . . . .  | 90 |
| 245 | Figure 8.4: Post-fit pull from nominal values for nuisance parameters representing<br>246 systematic uncertainties. Systematics pruned during the fit are not shown.<br>247 The dashed line represents the nominal pre-fit values. The green and<br>248 yellow bands represent the 68% ( $\pm 1\sigma$ ) and 95% ( $\pm 2\sigma$ ) confidence intervals<br>249 for the nominal fit value. . . . .  | 93 |
| 250 | Figure 8.5: Observed (solid line) and expected (dotted line) upper limits as a function<br>251 of the $Z'$ mass at 95% CL on the cross-section of $pp \rightarrow t\bar{t}Z'$ production<br>252 times the $Z' \rightarrow t\bar{t}$ branching ratio. The region above the observed limit is<br>253 excluded. The solid blue line represents the theoretical signal cross-section<br>254 with $c_t = 1$ at LO in QCD. The green and yellow bands represent the<br>255 68% ( $\pm \sigma$ ) and 95% ( $\pm 2\sigma$ ) confidence intervals respectively. . . . .   | 94 |

## KEY TO ABBREVIATIONS

257

### Physical & Mathematical Quantities

258  $\chi^2$  chi-squared259  $d_0$  transverse impact parameter260  $\Delta R$  angular distance261  $\sqrt{s}$  center-of-mass energy262  $\eta$  pseudorapidity263  $E_T$  transverse energy264  $E_T^{\text{miss}}$  missing transverse energy265  $\Gamma$  decay width266  $\gamma_5$  chirality projection operator267  $\gamma_\mu$  Dirac matrices268  $H_0$  null hypothesis269  $H_T$  scalar sum of transverse momenta  $p_T$  of all objects in an event270  $\mathcal{L}$  Lagrangian271  $\mathcal{L}(\theta)$  likelihood function272  $L$  instantaneous luminosity273  $m_{\ell\ell}$  dilepton invariant mass274  $\mu$  signal strength275  $\mu_F$  factorization scale276  $\mu_R$  renormalization scale277  $N_{\text{jets}}$  number of jets/jet multiplicity278  $\mathcal{O}(n)$  on the order of  $n$ 279  $\mathcal{P}$  Poisson probability280  $p_T$  transverse momentum

- <sup>281</sup>  $Q$  electric charge  
<sup>282</sup>  $q_\mu$  profile likelihood ratio  
<sup>283</sup>  $\sigma$  standard deviation  
<sup>284</sup>  $\sigma[b]$  cross-section  
<sup>285</sup>  $z_0$  longitudinal impact parameter

## 286 Particles & Processes

- <sup>287</sup>  $\gamma^*$  virtual photon  
<sup>288</sup>  $gg$  gluon-gluon fusion  
<sup>289</sup>  $pp$  proton-proton  
<sup>290</sup> PbPb lead-lead  
<sup>291</sup>  $q$  quark  
<sup>292</sup>  $q\bar{q}$  quark-antiquark pair  
<sup>293</sup>  $t\bar{t}$  top/anti-top quark pair  
<sup>294</sup>  $t\bar{t}X$  top pair in association with another particle  
<sup>295</sup>  $t\bar{t}t\bar{t}$  four-top-quark  
<sup>296</sup>  $V$  massive vector bosons ( $W^\pm, Z$ )  
<sup>297</sup>  $H$  Higgs in association with a vector boson

## 298 Acronyms

- <sup>299</sup> **1LOS** one lepton, or two leptons of opposite charges  
<sup>300</sup> **2HDM** two-Higgs doublet model  
<sup>301</sup> **AF3** AtlFast3 fast simulation  
<sup>302</sup> **ALICE** A Large Ion Collider Experiment  
<sup>303</sup> **ATLAS** A Toroidal LHC ApparatuS  
<sup>304</sup> **AWAKE** Advanced WAKEfield Experiment  
<sup>305</sup> **BDT** boosted decision tree  
<sup>306</sup> **BR** branching ratio

- <sup>307</sup> **BSM** Beyond the Standard Model
- <sup>308</sup> **CB** combined muon
- <sup>309</sup> **CERN** European Organization for Nuclear Research
- <sup>310</sup> **CKM** Cabibbo-Kobayashi-Maskawa matrix
- <sup>311</sup> **CL** confidence level
- <sup>312</sup> **CMS** Compact Muon Solenoid
- <sup>313</sup> **CP** charge-parity symmetry
- <sup>314</sup> **CR** control region
- <sup>315</sup> **CSC** Cathode Strip Chambers
- <sup>316</sup> **CTP** Central Trigger Processor
- <sup>317</sup> **ECIDS** Electron Charge ID Selector
- <sup>318</sup> **EFT** effective field theory
- <sup>319</sup> **EM** electromagnetic
- <sup>320</sup> **EW** electroweak
- <sup>321</sup> **FASER** ForwArd Search ExpeRiment
- <sup>322</sup> **FCal** forward calorimeter
- <sup>323</sup> **FS** full detector simulation
- <sup>324</sup> **GNN** graph neural network
- <sup>325</sup> **GRL** Good Run List
- <sup>326</sup> **GSC** Global Sequential Calibration
- <sup>327</sup> **GSF** Gaussian-sum filter
- <sup>328</sup> **GUT** Grand Unified Theory
- <sup>329</sup> **HEC** hadronic endcap calorimeter
- <sup>330</sup> **HF** heavy-flavor
- <sup>331</sup> **HL-LHC** High-Luminosity Large Hadron Collider
- <sup>332</sup> **HLT** High-Level Trigger
- <sup>333</sup> **ID** Inner Detector

- <sup>334</sup> **IP** interaction point
- <sup>335</sup> **JER** jet energy resolution
- <sup>336</sup> **JES** jet energy scale
- <sup>337</sup> **JVT** Jet Vertex Tagger
- <sup>338</sup> **KATRIN** Karlsruhe Tritium Neutrino Experiment
- <sup>339</sup> **L1** Level 1
- <sup>340</sup> **LAr** liquid argon
- <sup>341</sup> **LF** light-flavor
- <sup>342</sup> **LH** likelihood
- <sup>343</sup> **LHC** Large Hadron Collider
- <sup>344</sup> **LHCb** Large Hadron Collider beauty
- <sup>345</sup> **LINAC** linear accelerator
- <sup>346</sup> **LLH** log-likelihood
- <sup>347</sup> **LO** leading order
- <sup>348</sup> **MC** Monte Carlo simulation
- <sup>349</sup> **ME** matrix element
- <sup>350</sup> **ML** multilepton
- <sup>351</sup> **MS** Muon Spectrometer
- <sup>352</sup> **MDT** Monitored Drift Tubes
- <sup>353</sup> **MET** missing transverse energy
- <sup>354</sup> **NF** normalization factor
- <sup>355</sup> **NNJvt** Neural Network-based Jet Vertex Tagger
- <sup>356</sup> **NLO** next-to-leading order
- <sup>357</sup> **NNLO** next-to-next-to-leading order
- <sup>358</sup> **NP** nuisance parameter
- <sup>359</sup> **OP** operating point (also working point)
- <sup>360</sup> **OS** opposite-sign

- <sup>361</sup> **PCBT** pseudo-continuous  $b$ -tagging
- <sup>362</sup> **PDF** parton distribution function
- <sup>363</sup> **POI** parameter of interest
- <sup>364</sup> **PS** parton shower
- <sup>365</sup> **PV** primary vertex
- <sup>366</sup> **QCD** quantum chromodynamics
- <sup>367</sup> **QED** quantum electrodynamics
- <sup>368</sup> **QFT** quantum field theory
- <sup>369</sup> **QmisID** charge mis-identification
- <sup>370</sup> **RPC** Resistive Plate Chamber
- <sup>371</sup> **SCT** Semiconductor Tracker
- <sup>372</sup> **SF** scale factor
- <sup>373</sup> **SM** Standard Model
- <sup>374</sup> **SR** signal region
- <sup>375</sup> **SS** same-sign
- <sup>376</sup> **SSB** spontaneous symmetry breaking
- <sup>377</sup> **SS2L** same-sign dilepton
- <sup>378</sup> **SSML** same-sign dilepton, or more than two leptons of any charges
- <sup>379</sup> **TDAQ** Trigger and Data Acquisition
- <sup>380</sup> **TGC** Thin-Gap Chamber
- <sup>381</sup> **TRT** Transition Radiation Tracker
- <sup>382</sup> **VEV** vacuum expectation value
- <sup>383</sup> **VR** validation region
- <sup>384</sup> **UE** underlying-event

# <sup>385</sup> Chapter 1. Introduction

<sup>386</sup> The 20<sup>th</sup> century ushered in a revolutionary period for mankind's understanding of the  
<sup>387</sup> fundamental nature of matter and the forces that govern our universe with the development  
<sup>388</sup> of special relativity and quantum mechanics, which redefined our understanding of space,  
<sup>389</sup> time, energy and matter at the furthest extremes of scale from the vast reaches of the cosmos  
<sup>390</sup> to the tiniest constituents of matter. Building on these principles, Quantum Electrodynamics  
<sup>391</sup> (QED) [1–3] was developed as the first successful quantum field theory (QFT) describing  
<sup>392</sup> electromagnetism. The discovery of beta decay [4] and its paradoxical behaviors within the  
<sup>393</sup> framework of QED prompted the prediction of neutrinos and development of the theory of  
<sup>394</sup> weak interaction.

<sup>395</sup> At around the same time, a spectrum of strongly interacting particles was discovered  
<sup>396</sup> [5] as particle accelerators probed deeper into atomic nuclei, leading to the formation of  
<sup>397</sup> the quark model in the 1960s and with it a hypothesized new binding force, the strong  
<sup>398</sup> force. However, the QFT framework remained incapable of describing the weak and strong  
<sup>399</sup> interactions until advancements in gauge theory and the quantization of non-Abelian gauge  
<sup>400</sup> via QFT resulted in the formation of Yang-Mills theory [6, 7]. This sparked a renaissance  
<sup>401</sup> in modern physics with the unification of electromagnetism and weak force in 1967 under  
<sup>402</sup> the framework of electroweak (EW) [8] theory, as well as the development of Quantum  
<sup>403</sup> Chromodynamics (QCD) [9, 10] to describe the strong force binding quarks.

<sup>404</sup> At this point, the prediction of massless bosons within EW formalism remained a contra-  
<sup>405</sup> diction to the predicted massive  $W^\pm$  and  $Z$  bosons that mediate the weak force. This was  
<sup>406</sup> resolved by the introduction of EW spontaneous symmetry breaking and the Higgs mech-  
<sup>407</sup> anism in 1964 [11–13], which explained the generation of masses for both the EW bosons

408 and fermions. Together, these developments culminated in the Standard Model of parti-  
409 cle physics SM [14], a comprehensive theory that described the electromagnetic, weak, and  
410 strong interactions, classified all known fundamental particles and predicted mathematically  
411 consistent but not yet observed particles. Following its inception, particles predicted by the  
412 Standard Model were gradually observed experimentally, starting with the gluon in 1979  
413 [15], then the  $W^\pm$  and  $Z$  bosons [16, 17], and finally the top quark in 1995 [18, 19]. The  
414 final missing piece was confirmed as the Higgs boson was observed in 2012 independently  
415 by the ATLAS [20] and CMS [21] detectors at the Large Hadron Collider, completing the  
416 Standard Model after a 40-year search and cementing it as the most successful framework  
417 so far describing fundamental constituents of matter and their governing forces.

418 Despite its successes, the Standard Model remains incomplete. Key unanswered questions  
419 include the nature of dark matter [22], which makes up about 27% of the universes energy  
420 content but has no explanation within the Standard Model; the origin of neutrino masses and  
421 their oscillations [23]; the observed matter-antimatter asymmetry in the universe; possible  
422 unification of the EW and strong interaction into a Grand Unified Theory (GUT); and the  
423 hierarchy problem describing the large discrepancy in scales between forces and the apparent  
424 lightness of the Higgs boson compared to values predicted from quantum corrections.

425 After the discovery of the Higgs boson, efforts have been underway to construct new  
426 hypotheses and models in search of beyond the Standard Model (BSM) physics via different  
427 avenues, one of which being direct searches at colliders for new resonances or particles not  
428 predicted by the SM. In particular, the top quark possesses large mass and strong coupling to  
429 the Higgs boson [24] which gives it a special role in many proposed BSM models as a possible  
430 connection with strong coupling to new particles and heavy resonances. In addition, the  
431 top quark has a clean decay signature with well-understood final states and is produced in

abundance at the LHC from  $pp$  collisions in the form of top pairs  $t\bar{t}$  [25, 26]. This dissertation presents a search for the production of a heavy resonance that couples preferentially to top quark (topophilic) in association with a top pair ( $t\bar{t}$ ) in the final state with either two leptons of the same electric charge or at least three leptons (SSML). The search is performed in proton-proton collisions at  $\sqrt{s} = 13$  TeV with the ATLAS detector [27] via the four-top ( $t\bar{t}t\bar{t}$ ) production channel.

A similar search for topophilic heavy resonances was performed using  $t\bar{t}t\bar{t}$  final state containing either one lepton or two opposite-sign leptons (1LOS) [28] with a much larger branching ratio of 56% and larger irreducible background of SM processes. Despite the small cross-section within the SM, the  $t\bar{t}t\bar{t}$  SSML final state provides heightened sensitivity to BSM physics and higher signal-to-background ratio than inclusive resonance searches (e.g. in dijet or dilepton final states) due to the distinctive signal signature and suppression of large SM background processes present in  $t\bar{t}$ -associated production i.e. diboson ( $VV$ ),  $t\bar{t}$  production with an additional boson ( $t\bar{t}V/ttH+jets$ ) or with additional light leptons from heavy-flavor decays ( $t\bar{t} + HF$ ). The cross-section for  $t\bar{t}t\bar{t}$  production can be enhanced by many proposed BSM models including supersymmetric gluino pair-production [29, 30], scalar gluon pair-production [31, 32], top-quark-compositeness models [33, 34], effective field theory (EFT) operators [26, 35–38] and two-Higgs-doublet models (2HDM) [39–43]. Searching within this channel is particularly motivated by the recent observed excess in the measurement of four-top production in the SSML final state at the LHC by the ATLAS detector [44] with a measured cross-section of  $24^{+7}_{-6}$  fb, almost double the SM prediction of  $13.4^{+1.0}_{-1.8}$  fb.

A simplified color-singlet vector boson model [45] is employed for the search to minimize parameter dependency on model choice. Data-driven background estimation methods are implemented for  $t\bar{t}W$ - one of the dominant irreducible backgrounds in the analysis - and

456 the charge misidentification background to rectify mismodeling related to jet multiplicity  
457 in simulated background that were not covered in the previous 1LOS  $t\bar{t}Z'$  search [28] and  
458 SSML  $t\bar{t}H/A \rightarrow t\bar{t}t\bar{t}$  search [46]. These methods are employed similarly to that in previous  
459 SM  $t\bar{t}t\bar{t}$  analyses [44, 47].

460 This dissertation is organized as follows. Chapter 2 presents the formalism of the SM and  
461 relevant BSM concepts. Chapter 3 provides an introduction to the LHC and ATLAS detector.  
462 Chapter 4 describes the reconstruction and identification of physics object from detector  
463 signals. Chapter 5 defines the data and simulated samples used in the analysis. Chapter 6  
464 describes the analysis strategy, including object definition, analysis region description and  
465 background estimation methods. Chapter 7 summarizes the uncertainties involved in the  
466 analysis. Chapter 8 presents the statistical interpretation and analysis results. Finally,  
467 Chapter 9 discusses a summary of the analysis and future outlook.

# 468 Chapter 2. Theoretical Overview

## 469 2.1 The Standard Model

470 The Standard Model of Physics (SM) [48] is currently the most successful formalism to  
471 describe the physical world at a microscopic scale by providing descriptions for all currently  
472 known elementary particles, along with three out of four fundamental forces (electromag-  
473 netism, weak force, strong force) with the exception of gravity. The SM is however not  
474 perfect, and there remain unanswered questions that require development and discovery of  
475 new physics beyond the Standard Model (BSM). This chapter describes an overview of  
476 important components within the SM and relevant BSM aspects for this analysis.

### 477 2.1.1 Elementary particles

478 Elementary particles in the SM can be classified into two groups: bosons consisting  
479 of particles following Bose-Einstein statistics with integer spin, and fermions consisting of  
480 particles following Fermi-Dirac statistics with half-integer spin. Fermions are the building  
481 blocks of composite particles and consequently all known matter, and can be further classified  
482 into quarks & leptons. Bosons act as force mediators for all fundamental forces described by  
483 the SM, and can either be a scalar boson with spin 0 or vector gauge bosons with spin 1. For  
484 each elementary particle, there also exists a corresponding antiparticle with identical mass  
485 and opposite charge (electric or color). Figure 2.1 shows all known elementary particles in  
486 the SM.

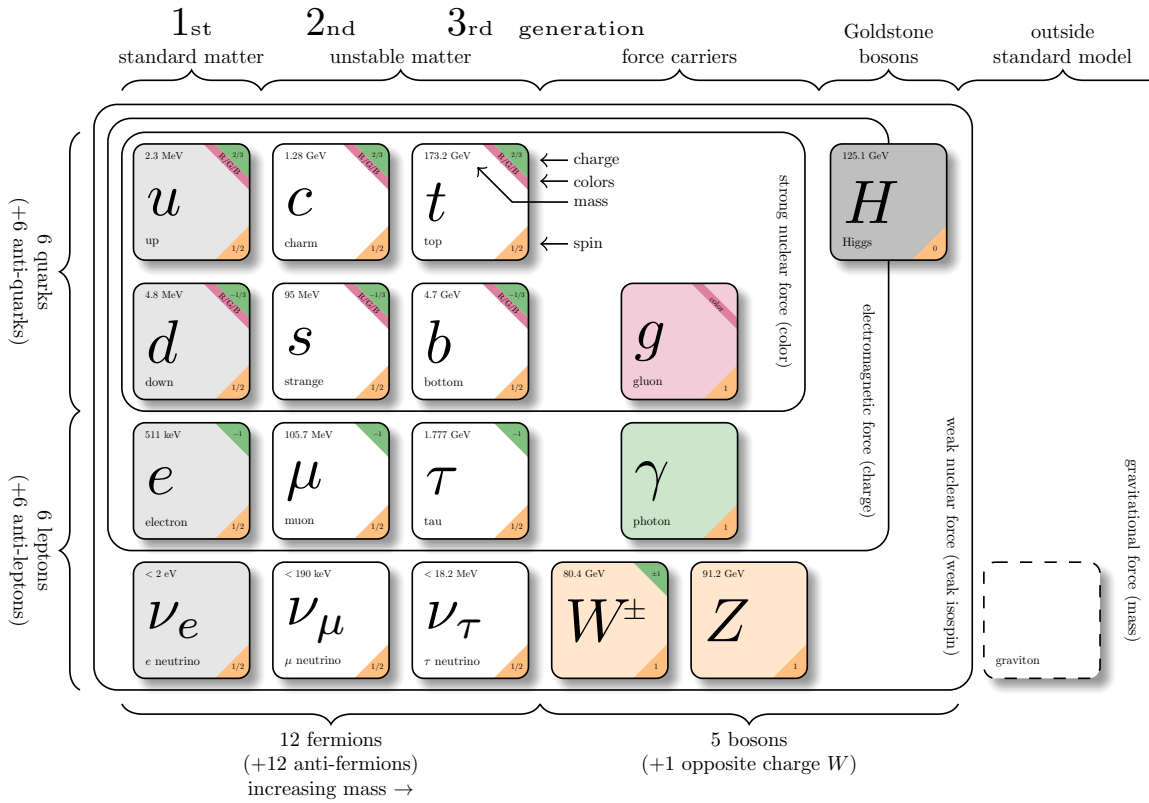


Figure 2.1: Particles within the SM and their properties [49].

## 487 Fermions

488 Fermions consist of quarks and leptons with six flavors each, grouped into three genera-  
 489 tions of doublets. The six quark flavors are up ( $u$ ), down ( $d$ ), charm ( $c$ ), strange ( $s$ ), bottom  
 490 ( $b$ ) and top ( $t$ ), arranged in increasing order of mass. The quark flavors form three doublets  
 491 ( $u, d$ ), ( $c, s$ ) and ( $t, b$ ), with each doublet containing one quark with electric charge of  $+2/3$   
 492 ( $u, s, t$ ), and the other with charge of  $-1/3$  ( $d, c, b$ ). Each quark also possesses a property  
 493 known as color charge, with possible values of red ( $R$ ), green ( $G$ ), blue ( $B$ ) or their corre-  
 494 sponding anticolor ( $\bar{R}, \bar{G}, \bar{B}$ ). Color charge follows color confinement rules, which allows  
 495 only configurations of quarks with total neutral color charge to exist in isolation. Neutral

496 charge configurations can be formed from either a set of three colors ( $R, G, B$ ), a set of a  
497 color and its anticolor, or any combination of the two. Consequently, quarks can only exist  
498 in bound states called hadrons and no isolated quark can be found in a vacuum. Quarks are  
499 the only elementary particles in the SM that can interact with all four fundamental forces.

500 The three leptons doublets consist of three charged leptons: electron ( $e$ ), muon ( $\mu$ ), tau  
501 ( $\tau$ ), and their respective neutrino flavors: electron neutrino ( $\nu_e$ ), muon neutrino ( $\nu_\mu$ ), tau  
502 neutrino ( $\nu_\tau$ ). Charged leptons carry an electric charge of  $-1$ , while their antiparticles carry  
503 the opposite charge ( $+1$ ) and their corresponding neutrino flavors carry no charge. Charged  
504 leptons interact with all fundamental forces except the strong force, while neutrinos only  
505 interact with the weak force and gravity.

506 **Bosons**

507 The SM classifies bosons into two types: one scalar boson with spin 0 known as the  
508 Higgs ( $H$ ) boson, and vector gauge bosons with spin 1 known as gluons ( $g$ ), photon ( $\gamma$ ),  $W^\pm$   
509 and  $Z$  bosons [22]. Gluons and photon are massless, while the  $W^\pm$ ,  $Z$  and  $H$  bosons are  
510 massive. Each vector gauge boson serves as the mediator for a fundamental force described  
511 by the SM. Gluons are massless particles mediating the strong interaction by carrying color  
512 charges between quarks following quantum chromodynamics (QCD). Each gluon carries a  
513 non-neutral color charge out of eight linearly independent color states in the gluon color octet  
514 [50]. The photon is the massless and charge-neutral mediator particle for the electromagnetic  
515 interaction following quantum electrodynamics (QED). The  $W^\pm$  and  $Z$  bosons are massive  
516 mediator particles for the weak interaction, with the  $W^\pm$  boson carrying an electric charge  
517 of  $\pm 1$  while the  $Z$  boson is charge neutral.

518 Other than the vector gauge boson, the only scalar boson in the SM is the massive and

519 charge neutral Higgs boson [22]. The Higgs boson does not mediate any fundamental force  
 520 like vector bosons, but serve to provide the rest mass for all massive elementary particles in  
 521 the SM through the Higgs mechanism described in section 2.1.2.3.

522 **Top quark**

523 As of now, the top quark ( $t$ ) is the heaviest particle in the SM with mass of about 173 GeV  
 524 [51], approaching the EW symmetry breaking scale. Its high mass gives the top quark the  
 525 strongest Yukawa coupling to the Higgs boson ( $y_t \approx 1$ ) [24] and exotic resonances in many  
 526 proposed BSM models [52–55], making the top quark and its processes attractive vehicles  
 527 with which to probe new physics.

528 Due to its mass, the top quark has a  
 529 very short lifetime of  $10^{-24}$  s [22] and de-  
 530 cays before it can hadronize following color  
 531 confinement. The top quark decays to a  $W$   
 532 boson and a  $b$ -quark with a branching ratio  
 533 of almost 100%. The  $W$  boson can subse-  
 534 quently decay to a quark-antiquark pair or  
 535 to a lepton-neutrino pair (Figure 2.2), with  
 536 branching ratios of approximately 68% and  
 537 32% respectively. All lepton flavors have  
 538 similar branching ratios during a leptonic  $W$   
 539 decay.

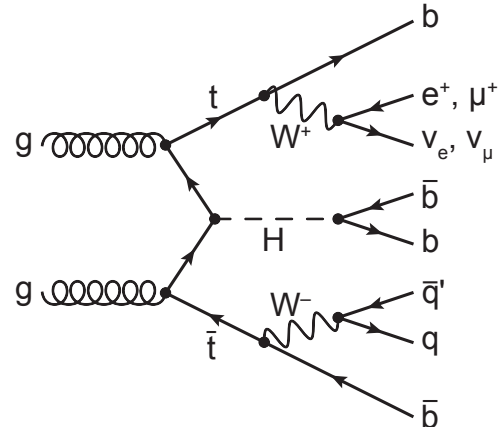


Figure 2.2: Feynman diagram for  $t\bar{t}$  production and subsequent decay processes [56]. Top quark decays into a  $W$ -boson and  $b$ -quarks, and  $W$ -boson can decay to a  $q\bar{q}$  or a  $\ell\nu_\ell$  pair.

## 540 2.1.2 Mathematical formalism

541 The SM can be described within the formalism of quantum field theory (QFT) with the  
542 Lagrangian [57]

$$\mathcal{L}_{\text{SM}} = \mathcal{L}_{\text{QCD}} + \underbrace{(\mathcal{L}_{\text{gauge}} + \mathcal{L}_{\text{fermion}} + \mathcal{L}_{\text{Higgs}} + \mathcal{L}_{\text{Yukawa}})}_{\mathcal{L}_{\text{EW}}} \quad (2.1)$$

543 where  $\mathcal{L}_{\text{QCD}}$  is the QCD term and  $\mathcal{L}_{\text{EW}}$  is the electroweak (EW) term of the Lagrangian.  
544 Formalism of QFT within the SM treats particles as excitations [58] of their corresponding  
545 quantum fields i.e. fermion field  $\psi$ , electroweak boson fields  $W_{1,2,3}$  &  $B$ , gluon fields  $G_\alpha$  and  
546 Higgs field  $\phi$ .

547 The foundation of modern QFT involves gauge theory. A quantum field has gauge sym-  
548 metry if there exists a continuous gauge transformation that when applied to every point in  
549 a field (local gauge transformation) leaves the field Lagrangian unchanged. The set of gauge  
550 transformations of a gauge symmetry is the symmetry group of the field which comes with  
551 a set of generators, each with a corresponding gauge field. Under QFT, the quanta of these  
552 gauge fields are called gauge bosons.

553 The SM Lagrangian is gauge invariant under global Poincaré symmetry and local  $SU(3)_C \times$   
554  $SU(2)_L \times U(1)_Y$  gauge symmetry, with the  $SU(3)_C$  symmetry group corresponding to the  
555 strong interaction and  $SU(2)_L \times U(1)_Y$  to the EW interaction. Global Poincaré symmetry  
556 ensures that  $\mathcal{L}_{\text{SM}}$  satisfies translational symmetry, rotational symmetry and Lorentz boost  
557 frame invariance [59]. These symmetries give rise to corresponding conservation laws, which  
558 lead to conservation of momentum, angular momentum and energy in the SM as a result of  
559 Noether's theorem [60].

560    2.1.2.1    Quantum chromodynamics

561        Quantum chromodynamics is a non-Abelian gauge theory i.e. Yang-Mills theory [6, 7]  
 562        describing the strong interaction between quarks in the SM with the gauge group  $SU(3)_C$ ,  
 563        where  $C$  represents conservation of color charge under  $SU(3)_C$  symmetry. According to  
 564        QFT, quarks can be treated as excitations of the corresponding quark fields  $\psi$ . The free Dirac  
 565        Lagrangian for the quark fields  $\mathcal{L}_0 = \bar{\psi}(i\gamma^\mu\partial_\mu - m)\psi$  is invariant under global  $SU(3)$  sym-  
 566        metry, but not under local  $SU(3)_C$  symmetry. To establish invariance under local  $SU(3)_C$   
 567        symmetry, the gauge covariant derivative  $D_\mu$  is defined so that

$$D_\mu\psi = (\partial_\mu - ig_s G_\mu^a T_a)\psi, \quad (2.2)$$

568        where  $g_s = \sqrt{4\pi\alpha_s}$  is the QCD coupling constant,  $G_\mu^a(x)$  are the eight gluon fields, and  
 569         $T_a$  are generators of  $SU(3)_C$ , represented as  $T_a = \lambda_a/2$  with  $\lambda_a$  being the eight Gell-Mann  
 570        matrices [50]. Let the gluon field strength tensors  $G_{\mu\nu}^a$  be

$$G_{\mu\nu}^a \equiv \partial_\mu G_\nu^a - \partial_\nu G_\mu^a - g_s f^{abc} G_\mu^b G_\nu^c, \quad (2.3)$$

571        where  $f^{abc}$  are the structure constants of  $SU(3)_C$ . The gauge invariant QCD Lagrangian  
 572        can then be written as

$$\begin{aligned} \mathcal{L}_{\text{QCD}} &= \bar{\psi}(i\gamma^\mu D_\mu - m)\psi - \frac{1}{4}G_{\mu\nu}^a G_a^{\mu\nu} \\ &= \underbrace{-\frac{1}{4}G_{\mu\nu}^a G_a^{\mu\nu}}_{\text{gluon kinematics}} + \underbrace{\bar{\psi}(i\gamma^\mu\partial_\mu - m)\psi}_{\text{quark kinematics}} + \underbrace{\bar{\psi}^i(g_s\gamma^\mu(T_a)_{ij}G_\mu^a)\bar{\psi}^j}_{\text{quark-gluon interaction}}, \end{aligned} \quad (2.4)$$

<sup>573</sup> where  $i, j$  are color indices with integer values from 1 to 3. Gluons are forced to be massless  
<sup>574</sup> from the lack of a gluon mass term to maintain gauge invariance for the Lagrangian.

<sup>575</sup> **2.1.2.2 Electroweak theory**

<sup>576</sup> The electroweak interaction is the unified description of the weak interaction and electro-  
<sup>577</sup> magnetism under the  $SU(2)_L \times U(1)_Y$  symmetry group, where  $L$  represents the left-handed  
<sup>578</sup> chirality of the weak interaction and  $Y$  represents the weak hypercharge quantum number.  
<sup>579</sup> Fermions can have either left-handed or right-handed chirality with the exception of neutr-  
<sup>580</sup>inos which can only have left-handed chirality within the SM framework. Fermions in the  
<sup>581</sup> SM can be divided into left-handed doublets and right-handed singlets

$$\psi_L = \begin{pmatrix} \nu_e \\ e_L \end{pmatrix}, \begin{pmatrix} \nu_\mu \\ \mu_L \end{pmatrix}, \begin{pmatrix} \nu_\tau \\ \tau_L \end{pmatrix}, \begin{pmatrix} u_L \\ d_L \end{pmatrix}, \begin{pmatrix} c_L \\ s_L \end{pmatrix}, \begin{pmatrix} t_L \\ b_L \end{pmatrix} \quad (2.5)$$

$$\psi_R = e_R, \mu_R, \tau_R, u_R, d_R, c_R, s_R, t_R, b_R.$$

<sup>582</sup> where  $g'$  is the  $B_\mu$  coupling constant and  $B_\mu(x)$  is a vector gauge field that transforms under  
<sup>583</sup>  $U(1)_Y$  as

$$B_\mu \rightarrow B_\mu + \frac{1}{g'} \partial_\mu \theta(x). \quad (2.6)$$

<sup>584</sup> Right-handed fermion singlets are not affected by  $SU(2)_L$  transformation, so the fermion  
<sup>585</sup> fields  $\psi$  transform under  $SU(2)_L$  as

$$\psi_L \rightarrow e^{iI_3\vec{\theta}(x)\cdot\vec{\sigma}/2}\psi_L \quad (2.7)$$

$$\psi_R \rightarrow \psi_R.$$

<sup>586</sup> where  $\vec{\sigma}/2$  are generators of  $SU(2)_L$  with  $\vec{\sigma}$  being the Pauli matrices. In order to preserve  
<sup>587</sup> local symmetry, the gauge covariant derivative for  $SU(2)_L$  and  $U(1)_Y$  can be defined [61] so

588 that the gauge covariant derivative for  $SU(2)_L \times U(1)_Y$  can be written as

$$\begin{aligned} D_\mu \psi_L &= \left( \partial_\mu - ig' \frac{Y_L}{2} B_\mu - ig \frac{\sigma_i}{2} W_\mu^i \right) \psi_L \\ D_\mu \psi_R &= \left( \partial_\mu - ig' \frac{Y_R}{2} B_\mu \right) \psi_R. \end{aligned} \quad (2.8)$$

589 where  $B_\mu(x)$  is a vector gauge field associated with  $U(1)_Y$  and  $W_\mu^i(x)$  ( $i = 1, 2, 3$ ) are three  
590 vector gauge fields associated with  $SU(2)_L$ . The  $B_\mu$  and  $W_\mu^i$  gauge fields transform under  
591 their corresponding symmetry groups  $U(1)_Y$  and  $SU(2)_L$  as

$$\begin{aligned} B_\mu &\rightarrow B_\mu + \frac{1}{g'} \partial_\mu \theta(x) \\ W_\mu^i &\rightarrow W_\mu^i + \frac{2}{g} \partial_\mu \theta_a(x) + \epsilon^{ijk} \theta_j(x) W_\mu^k, \end{aligned} \quad (2.9)$$

592 where  $g'$  is the  $B_\mu$  gauge coupling constant,  $g$  is the  $W_\mu^i$  gauge coupling constants and  $\epsilon^{ijk}$   
593 is the  $SU(2)_L$  structure constant. Similar to section 2.1.2.1, the kinetic term is added by  
594 defining field strengths for the four gauge fields

$$\begin{aligned} B_{\mu\nu} &\equiv \partial_\mu B_\nu - \partial_\nu B_\mu \\ W_{\mu\nu}^i &\equiv \partial_\mu W_\nu^i - \partial_\nu W_\mu^i - g e^{ijk} W_\mu^j W_\nu^k. \end{aligned} \quad (2.10)$$

595 The local  $SU(2)_L \times U(1)_Y$  invariant EW Lagrangian [61] is then

$$\begin{aligned} \mathcal{L}_{\text{EW}} &= i \bar{\psi} (\gamma^\mu D_\mu) \psi - \frac{1}{4} W_{\mu\nu}^i W_i^{\mu\nu} - \frac{1}{4} B_{\mu\nu} B^{\mu\nu} \\ &= \underbrace{i \bar{\psi} (\gamma^\mu \partial_\mu) \psi}_{\text{fermion kinematics}} - \underbrace{\bar{\psi} \left( \gamma^\mu g' \frac{Y}{2} B_\mu \right) \psi}_{\text{fermion-gauge boson interaction}} - \underbrace{\bar{\psi}_L \left( \gamma^\mu g \frac{\sigma_i}{2} W_\mu^i \right) \psi_L}_{\text{boson kinematics \& self-interaction}} - \frac{1}{4} W_{\mu\nu}^i W_i^{\mu\nu} - \frac{1}{4} B_{\mu\nu} B^{\mu\nu}. \end{aligned} \quad (2.11)$$

596 Under  $\approx 159.5$  GeV, the EW symmetry  $SU(2)_L \times U(1)_Y$  undergoes spontaneous symmetry  
 597 breaking [62] into  $U(1)_{\text{QED}}$  symmetry, which corresponds to a separation of the weak and  
 598 electrodynamic forces. Electroweak spontaneous symmetry breaking replaces the four mass-  
 599 less and similarly-behaved EW gauge bosons  $B_\mu$  and  $W_\mu^i$  with the EM boson  $\gamma$  and the weak  
 600 bosons  $Z/W^\pm$ , as well as giving the  $Z$  and  $W^\pm$  bosons masses via the Higgs mechanism.  
 601 This is due to a specific choice of gauge for the Higgs field leading to the reparameterization  
 602 of the EW bosons  $B_\mu$  and  $W_\mu^i$  to  $W^\pm/Z/\gamma$  using the relations

$$\begin{aligned}
 W_\mu^\pm &\equiv \frac{1}{\sqrt{2}} (W_\mu^1 \mp iW_\mu^2) \\
 \begin{pmatrix} A_\mu \\ Z_\mu \end{pmatrix} &\equiv \begin{pmatrix} \cos \theta_W & \sin \theta_W \\ -\sin \theta_W & \cos \theta_W \end{pmatrix} \begin{pmatrix} B_\mu \\ W_\mu^3 \end{pmatrix}
 \end{aligned} \tag{2.12}$$

603 where  $\theta_W \equiv \cos^{-1} (g/\sqrt{g^2 + g'^2})$  is the weak mixing angle. The boson kinetic term can also  
 604 be refactorized to extract cubic (three vertices) and quartic (four vertices) self-interactions  
 605 among the gauge bosons [61]. The Lagrangian can then be rewritten as

$$\begin{aligned}
 \mathcal{L} = & \underbrace{eA_\mu \bar{\psi} (\gamma^\mu Q) \psi}_{\text{electromagnetism}} + \underbrace{\frac{e}{2\sin \theta_W \cos \theta_W} \bar{\psi} \gamma^\mu (v_f - a_f \gamma_5) \psi Z_\mu}_{\text{neutral current interaction}} \\
 & + \underbrace{\frac{g}{2\sqrt{2}} \sum_{\psi_L} [\bar{f}_2 \gamma^\mu (1 - \gamma_5) f_1 W_\mu^+ + \bar{f}_1 \gamma^\mu (1 - \gamma_5) f_2 W_\mu^-]}_{\text{charged current interaction}} \\
 & + \underbrace{\mathcal{L}_{\text{kinetic}} + \mathcal{L}_{\text{cubic}} + \mathcal{L}_{\text{quartic}}}_{\text{boson self-interaction}}
 \end{aligned} \tag{2.13}$$

606 where  $\gamma_5 = i\gamma^0\gamma^1\gamma^2\gamma^3$  is the chirality projection operator,  $a_f = I_3$ ,  $v_f = I_3(1 - 4|Q| \sin^2 \theta_W)$   
 607 and  $f_1, f_2$  are up and down type fermions of a left-handed doublet.

608    **2.1.2.3 Higgs mechanism**

609    So far, the EW bosons are massless since the mass terms  $-m\bar{\psi}\psi$  for fermions and  
 610    $-mA^\mu A_\mu$  for bosons are not invariant under the EW Lagrangian symmetries. The parti-  
 611   cles must then acquire mass under another mechanism. The Brout-Engler-Higgs mechanism  
 612   [11–13] was introduced in 1964 to rectify this issue and verified in 2012 with the discovery  
 613   of the Higgs boson [20, 21].

614    The Higgs potential is expressed as

$$V(\phi^\dagger \phi) = \mu^2 \phi^\dagger \phi + \lambda (\phi^\dagger \phi)^2 \quad (2.14)$$

615    where  $\mu^2$  and  $\lambda > 0$  are arbitrary parameters, and the  $SU(2)_L$  doublet  $\phi = \begin{pmatrix} \phi^+ \\ \phi^0 \end{pmatrix}$  is the Higgs  
 616   field with complex scalar fields  $\phi^+$  and  $\phi^0$  carrying +1 and 0 electric charge respectively.  
 617   The Lagrangian for the scalar Higgs field is

$$\mathcal{L}_H = (\partial_\mu \phi)^\dagger (\partial^\mu \phi) - V(\phi^\dagger \phi). \quad (2.15)$$

618    Since the potential  $V(\phi^\dagger \phi)$  is constrained by  $\lambda > 0$ , the ground state is solely controlled by  
 619    $\mu$ . If  $\mu^2 > 0$ , the ground state energy is  $\phi = 0$ , and the EW bosons would remain massless.  
 620   If  $\mu^2 < 0$ , the ground state is

$$|\phi|^2 = -\frac{\mu^2}{2\lambda} \equiv \frac{v^2}{\sqrt{2}}, \quad (2.16)$$

621    where  $v$  is defined as the vacuum expectation value (VEV). The standard ground state for  
 622   the Higgs potential without loss of generality can be chosen as  $\phi(0) = 1/\sqrt{2}(0)_v$ .

623    Having  $U(1)$  symmetry allows any  $-e^{i\theta} \sqrt{\mu^2/\lambda}$  to be a ground state energy for the Higgs

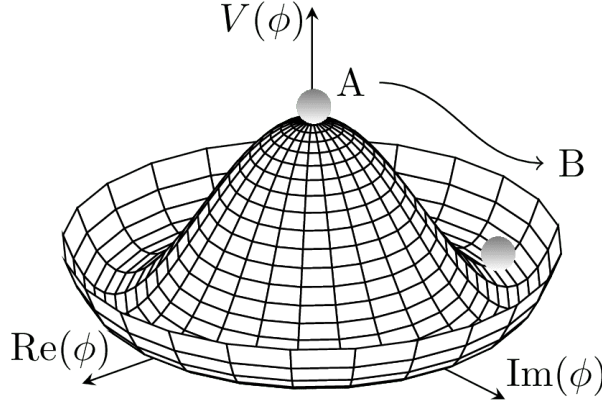


Figure 2.3: Illustration of a common representation of the Higgs potential [63]. Before SSB, the ground state  $\phi(0)$  is located at A which is symmetric with respect to the potential. A perturbation to this state fixes the ground state energy  $|\phi(0)|^2$  to a particular value at B, "spontaneously" breaking the symmetry and degeneracy in  $|\phi(0)|^2$ .

624 Lagrangian. This degeneracy results in spontaneous symmetry breaking of the  $SU(2)_L \times$   
 625  $U(1)_Y$  symmetry into  $U(1)_{\text{EM}}$  symmetry when the Higgs field settles on a specific vacuum  
 626 state as a result of a perturbation or excitation (Figure 2.3). The spontaneous symmetry  
 627 breaking introduces three massless (Nambu-Goldstone [64]) vector gauge boson  $\xi$  and a  
 628 massive scalar boson  $\eta$ , each corresponds to a generator of the gauge group. The vector field  
 629 for  $\xi$  and  $\eta$  are real fields parameterized as  $\xi \equiv \phi^+ \sqrt{2}$  and  $\eta \equiv \phi^0 \sqrt{2} - v$  [65]. The Higgs  
 630 field now becomes

$$\phi = \frac{v + \eta + i\xi}{\sqrt{2}} = \frac{1}{\sqrt{2}} e^{i\xi} \begin{pmatrix} 0 \\ v + \eta \end{pmatrix}. \quad (2.17)$$

631 Due to  $U(1)_{\text{EM}}$  invariance, a unitary gauge with the transformation  $\phi \rightarrow \exp(-i\xi \cdot) \frac{\sigma}{2v}$  can  
 632 be chosen for the Higgs field to eliminate the massless bosons and incorporate them into the  
 633 EM/weak bosons via Equation 2.12. This leaves the massive  $\eta$  which can now be observed as  
 634 an excitation of the Higgs field from the standard ground state and must be the Higgs boson  
 635  $h$ . Using the EW covariant derivative from Equation 2.8, the Higgs Lagrangian around the

636 vacuum state becomes

$$\begin{aligned}\mathcal{L}_H &= (D_\mu \phi)^\dagger (D^\mu \phi) - \mu^2 \left( \frac{v+h}{\sqrt{2}} \right)^2 - \lambda \left( \frac{v+h}{\sqrt{2}} \right)^4 \\ &= (D_\mu \phi)^\dagger (D^\mu \phi) - \frac{1}{2} \mu^2 h^2 - \lambda v h^3 - \frac{\lambda}{4} h^4 - \dots\end{aligned}\tag{2.18}$$

637 The Higgs mass can be extracted from the quadratic term as  $m_H = \sqrt{-2\mu^2}$ . The kinetic

638 term in the Lagrangian can be written as

$$\begin{aligned}(D_\mu \phi)^\dagger (D^\mu \phi) &= \frac{1}{2} (\partial_\mu h)^2 + \frac{g^2}{8} (v+h)^2 \left| W_\mu^1 - i W_\mu^2 \right|^2 + \frac{1}{8} (v+h)^2 (g' W_\mu - g B_\mu) \\ &= \frac{1}{2} (\partial_\mu h)^2 + (v+h)^2 \left( \frac{g^2}{4} W_\mu^+ W^{-\mu} + \frac{1}{8} (g^2 + g'^2) Z_\mu^0 Z^{0\mu} \right).\end{aligned}\tag{2.19}$$

639 Masses for the EW bosons can be extracted from the quadratic terms

$$m_{W^\pm} = \frac{v}{2} g, \quad m_Z = \frac{v}{2} \sqrt{g^2 + g'^2}, \quad m_\gamma = 0.\tag{2.20}$$

640 However, the fermion mass term  $-m\bar{\psi}\psi$  still breaks EW invariance after spontaneous sym-

641 metry breaking. Instead, fermions acquire mass by replacing the mass term with a gauge

642 invariant Yukawa term in the EW Lagrangian representing fermions' interactions with the

643 Higgs field [65]

$$\begin{aligned}\mathcal{L}_{\text{Yukawa}} &= -c_f \frac{v+h}{\sqrt{2}} (\bar{\psi}_R \psi_L + \bar{\psi}_L \psi_R) \\ &= -\underbrace{\frac{c_f}{\sqrt{2}} v (\bar{\psi} \psi)}_{\text{fermion mass}} - \underbrace{\frac{c_f}{\sqrt{2}} (h \bar{\psi} \psi)}_{\text{fermion-Higgs interaction}},\end{aligned}\tag{2.21}$$

644 where  $c_f$  is the fermion-Higgs Yukawa coupling. The fermion mass is then  $m_f = c_f v / \sqrt{2}$ .

## 645 2.2 Beyond the Standard Model: $t\bar{t}Z' \rightarrow t\bar{t}t\bar{t}$

646 This analysis uses the  $t\bar{t}t\bar{t}$  final state signal signature to search for the existence of a  
647 heavy neutral BSM resonance that couples strongly to the top quark, nominally named  
648  $Z'$ . The cross-section for  $t\bar{t}t\bar{t}$  production at the LHC can be enhanced by many possible  
649 BSM models, in particular production of heavy scalars and pseudoscalar bosons predicted in  
650 Type-II two-Higgs-doublet models (2HDM) [39–43] or possible production of a heavy neutral  
651 resonance boson  $Z'(\rightarrow t\bar{t})$  in association with a  $t\bar{t}$  pair [66, 67]. The  $t\bar{t}Z'$  production mode  
652 and consequently  $t\bar{t}t\bar{t}$  signal signature can provide a more sensitive channel for searches by  
653 avoiding contamination from the large SM  $gg \rightarrow t\bar{t}$  background in an inclusive  $Z' \rightarrow t\bar{t}$   
654 search.

### 655 2.2.1 Top-philic vector resonance

656 Many BSM models extend the SM by adding to the SM gauge group additional  $U(1)'$   
657 gauge symmetries [68, 69], each with an associated vector gauge boson ( $Z'$ ). In the case of  
658 a BSM global symmetry group with rank larger than the SM gauge group, the symmetry  
659 group can spontaneously break into  $G_{\text{SM}} \times U(1)'^n$ , where  $G_{\text{SM}}$  is the SM gauge group  
660  $SU(3)_C \times SU(2)_L \times U(1)_Y$  and  $U(1)'^n$  is any  $n \geq 1$  number of  $U(1)'$  symmetries. The  
661 existence of additional vector boson(s)  $Z'$  would open up many avenues of new physics e.g.  
662 extended Higgs sectors from  $U(1)'$  symmetry breaking [70, 71] and possible new particles as  
663 heavy  $Z'$  decay products [73].

664 Due to the top quark having the largest mass out of all known elementary particles in the  
665 SM, many BSM models [38–43, 74, 75] predict ‘top-philic’ vector resonances that have much  
666 stronger coupling to the top quark compared to other quarks. Previous BSM  $t\bar{t}t\bar{t}$  search at

667 the LHC for top-philic resonances [28] with a similar model in the single-lepton final state  
 668 and similar mass ranges set upper limits on observed (expected)  $Z'$  production cross section  
 669 between 21 (14) fb to 119 (86) fb depending on parameter choice. This analysis is also moti-  
 670 vated by the recent observation of SM  $t\bar{t}t\bar{t}$  production in the same-sign multilepton (SSML)  
 671 channel by ATLAS [44] and CMS [76] at  $6.1\sigma$  and  $5.6\sigma$  discovery significance respectively.

672 A simplified top-philic color-singlet vector particle model [45, 74] is employed in the  
 673 search. The interaction Lagrangian assumes the  $Z'$  couples dominantly the top quark and  
 674 has the form

$$\begin{aligned}
 \mathcal{L}_{Z'} &= \bar{t}\gamma_\mu (c_L P_L + c_R P_R) t Z'^\mu \\
 &= c_t \bar{t}\gamma_\mu (\cos\theta P_L + \sin\theta P_R) t Z'^\mu,
 \end{aligned} \tag{2.22}$$

675 where  $c_t = \sqrt{c_L^2 + c_R^2}$  is the  $Z'$ -top coupling strength,  $P_{L/R} = (1 \mp \gamma_5)/2$  are the chirality  
 676 projection operators, and  $\theta = \tan^{-1}(c_R/c_L)$  is the chirality mixing angle. Expanding the  
 677 Lagrangian results in

$$\mathcal{L}_{Z'} = \frac{1}{\sqrt{2}} \bar{t}\gamma_\mu \left[ \sin\left(\theta + \frac{\pi}{4}\right) - \left( \sqrt{2} \cos\left(\theta + \frac{\pi}{4}\right) \right) \gamma_5 \right] t Z'^\mu, \tag{2.23}$$

678 which bears striking resemblance to the EW Lagrangian neutral current interaction term in  
 679 Equation 2.13, showing the similarity between the  $Z'$  and the  $Z$  boson that acquires mass  
 680 from  $SU(2)_L \times U(1)_Y$  spontaneous symmetry breaking. Assuming the  $Z'$  mass  $m_{Z'}$  is much  
 681 larger than the top mass ( $m_t^2/m_{Z'}^2 \approx 0$ ), the  $Z'$  decay width at leading-order (LO) can be  
 682 approximated as

$$\Gamma(Z' \rightarrow t\bar{t}) \approx \frac{c_t^2 m_{Z'}}{8\pi}. \tag{2.24}$$

683 It can be observed that  $\Gamma/m_{Z'} \approx c_t^2/8\pi \ll 1$  for  $c_t \approx 1$ , which suggests a very narrow and

684 well-defined resonance peak, validating the narrow-width approximation for the choice of

685  $c_t = 1$ .

## 686 2.2.2 Production channels

687 The main production channels at the LHC proton-proton collider for the aforementioned  
688 heavy topophilic color singlet  $Z'$  are at tree level and loop level, with the one-loop level being  
689 the dominant processes [45]. Loop level processes are dependent on the chirality angle  $\theta$ ,  
690 where  $\theta = \pi/4$  suppresses all but gluon-initiated box sub-processes. To minimize model  
691 dependence, only the tree level production was considered for this analysis by choosing  
692  $\theta = \pi/4$ . Figure 2.4 illustrates several tree level  $Z'$  production processes.

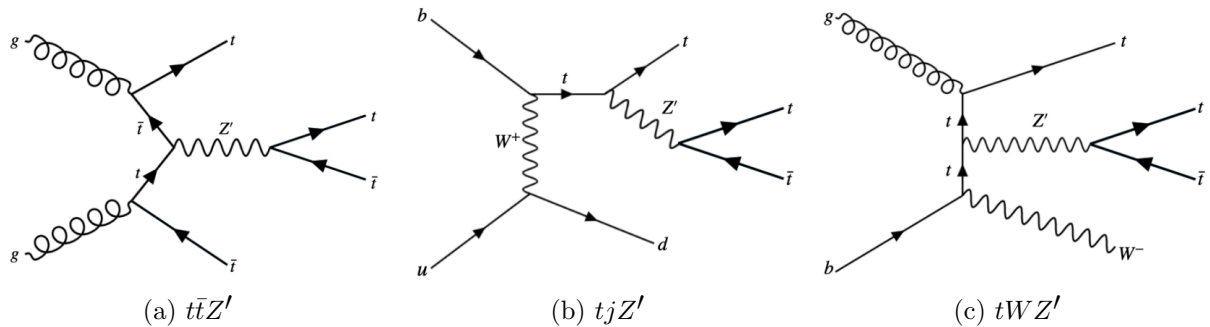


Figure 2.4: Feynman diagrams for tree level  $Z'$  production in association with (a)  $t\bar{t}$ , (b)  $tj$  (light quark) and (c)  $tW$ , decaying to final states containing (a)  $t\bar{t}t\bar{t}$  or (b)(c)  $t\bar{t}t$  [45].

693 The tree level  $t\bar{t}$ -associated process  $t\bar{t}Z'$  is the targeted production channel for the search  
694 in this dissertation. The  $t\bar{t}Z'$  cross-section at LO in QCD is shown in Figure 2.5. Con-  
695 tributions from the single-top-associated channels  $tjZ'$  and  $tWZ'$  are not considered due  
696 to a smaller cross-section by a factor of two compared to  $t\bar{t}Z'$  due to suppression in the  
697 three-body phase space [45]. Additionally,  $t\bar{t}Z' \rightarrow t\bar{t}t\bar{t}$  production is independent of  $\theta$  while  
698  $tjZ'$  and  $tWZ'$  are minimally suppressed under pure left-handed interactions ( $\theta = 0$ ) and  
699 maximally suppressed under pure right-handed interactions ( $\theta = \pi/2$ ); both channels are

700 affected by the choice of  $\theta = \pi/4$  to suppress loop level production.

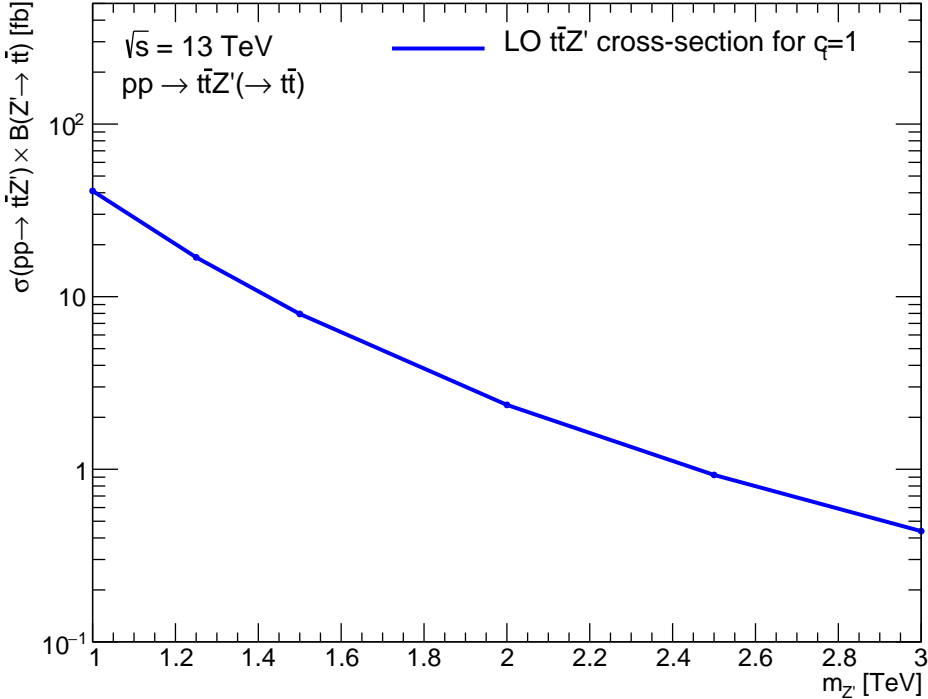


Figure 2.5: Theoretical  $t\bar{t}Z'$  production cross-section times  $Z' \rightarrow t\bar{t}$  branching ratio as a function of the  $Z'$  mass at LO in QCD coupling to top with  $c_t = 1$  under a simplified topophilic model [45, 74, 77].

### 701 2.2.3 Decay modes

702 The different  $W$  boson decay modes shown in Figure 2.2 result in many different final  
 703 states for  $t\bar{t}Z'/t\bar{t}t\bar{t}$  decay, which can each be classified into one of three channels shown in  
 704 Figure 2.6: all hadronic decays; exactly one lepton or two opposite-sign leptons (1LOS);  
 705 exactly two same-sign leptons or three or more leptons (SSML). The branching ratio for  
 706 each channel is shown in Figure 2.6. The all hadronic and 1LOS channels have much larger  
 707 branching ratios compared to SSML channel but suffer heavily from  $gg \rightarrow t\bar{t}$  background  
 708 contamination, giving the SSML channel better sensitivity at the cost of lower statistics.

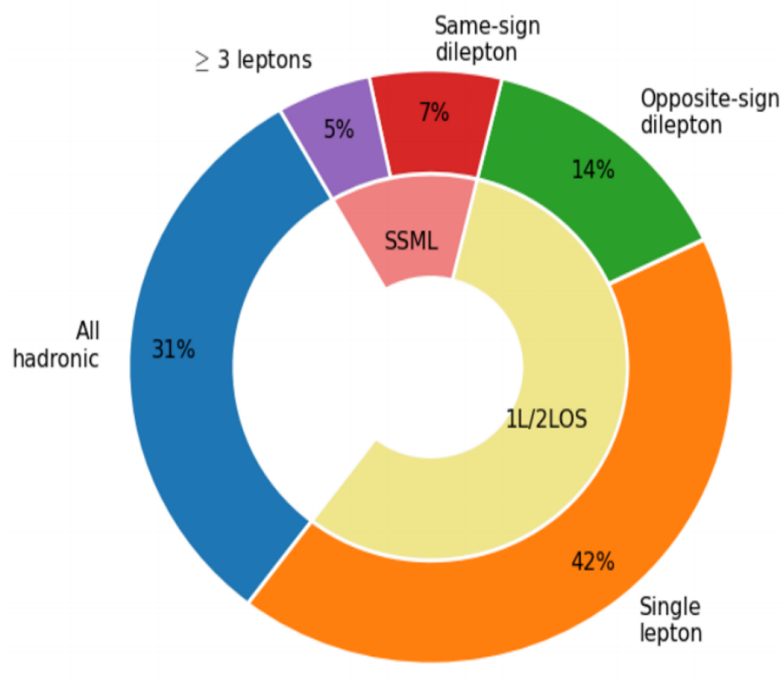


Figure 2.6: Branching ratios for  $t\bar{t}t\bar{t}$  decay [78]. The same-sign dilepton and multilepton channels together forms the SSML channel.

<sup>709</sup> This is also the targeted channel for this analysis.

# 710 Chapter 3. LHC & ATLAS Experiment

## 711 3.1 The Large Hadron Collider

712 Predictions from theoretical models are evaluated against experimental data collected  
713 from particle detectors. This chapter provides a detailed overview of the Large Hadron  
714 Collider (LHC) and the ATLAS detector, one of the key experiments designed to study  
715 high-energy collisions at the LHC.

### 716 3.1.1 Overview

717 The Large Hadron Collider [79] (LHC) is currently the world's largest particle collider  
718 with a circumference of almost 27 km. Built by CERN on the border of Switzerland and  
719 France, the LHC is designed as a particle collider for proton-proton ( $pp$ ), sometimes heavy  
720 ions i.e. lead-lead (PbPb) and proton-lead ( $pPb$ ) beams at TeV-scale energies. Two beams  
721 of particles are injected into the LHC in opposite directions and allowed to collide at the  
722 center of four major experiments:

- 723 • **A Toroidal LHC ApparatuS** (ATLAS) [27] and **Compact Muon Solenoid** (CMS)  
724 [80]: multi-purpose detectors, designed to target a variety of phenomena including SM,  
725 BSM and heavy-ion physics.
- 726 • **Large Ion Collider Experiment** (ALICE) [81]: specialized detector to record ion  
727 collisions and study heavy-ion physics.
- 728 • **Large Hadron Collider beauty** (LHCb) [82]: detector dedicated to study properties  
729 of  $b$ -quarks and  $b$ -hadrons.

730      Aside from the four major experiments, the LHC also houses smaller experiments e.g.  
 731     AWAKE [83], FASER [84], KATRIN [85], that either share an interaction point with one of  
 732     the above experiments or make use of particle beams pre-LHC injection.

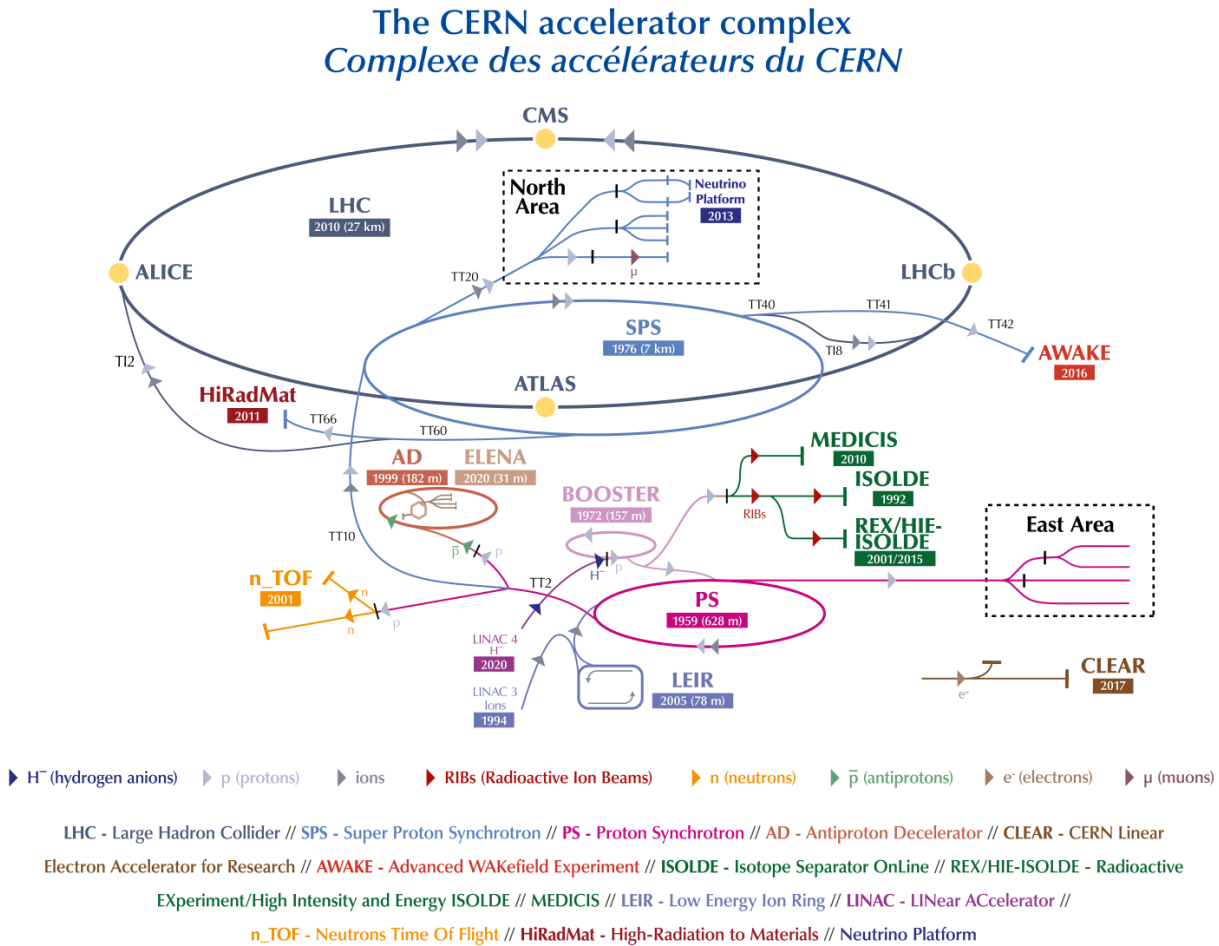


Figure 3.1: The full CERN accelerator complex as of 2022 [86].

733      The majority of the LHC operational time is dedicated to studying  $pp$  collisions of up to  
 734      $\sim 13$  TeV center-of-mass energy, denoted as  $\sqrt{s}$ . Reaching collision energy requires a sequence  
 735     of accelerators within the CERN accelerator complex, shown in Figure 3.1. Proton produc-  
 736     tion starts at LINAC 4, where hydrogen atoms are accelerated to 160 MeV then stripped  
 737     of electrons. The leftover proton beams are injected into the Proton Synchrotron Booster

738 (PSB) and accelerated to 2 GeV before being transferred into the Proton Synchrotron (PS).  
 739 Here, the beams are ramped up to 26 GeV then injected into the Super Proton Synchrotron  
 740 (SPS) to further raise the energy threshold to 450 GeV. The beams are finally injected into  
 741 the LHC in opposite directions, continuously increasing in energy up to 6.5 TeV per beam,  
 742 reaching the 13 TeV center-of-mass energy threshold necessary for collision during Run 2.  
 743 As of the start of Run 3 in 2022, proton beams can now be ramped up to 6.8 TeV per beam  
 744 for a total of  $\sqrt{s} = 13.6$  TeV.

### 745 3.1.2 LHC operations

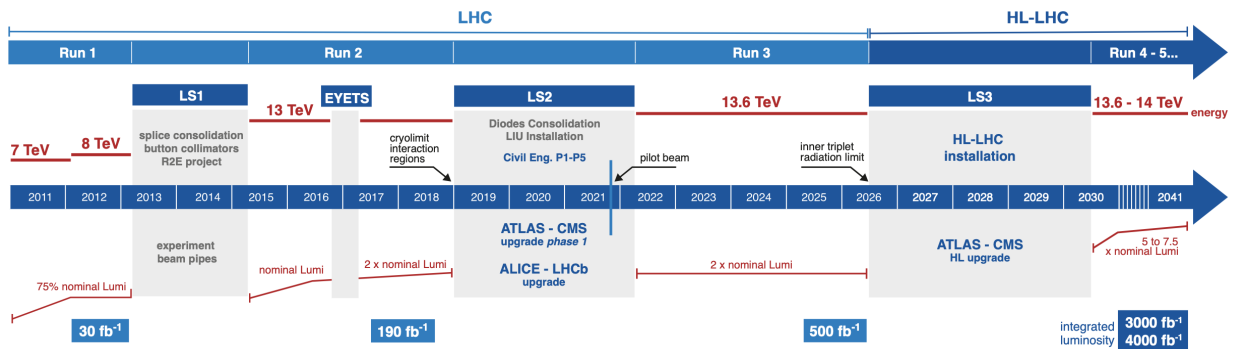


Figure 3.2: Current and future timeline of LHC operations with corresponding center-of-mass energies and projected integrated luminosities. [87].

746 Operations at the LHC are defined in periods of data-taking and shut-down known as  
 747 runs and long shutdowns respectively; the first period (Run 1) started with first collisions  
 748 at the LHC in 2010 at  $\sqrt{s} = 7$  TeV [88]. Upgrades are usually carried out for detectors and  
 749 accelerators during long shutdowns, raising the maximum energy threshold in preparation  
 750 for the next run. An overview of the LHC runtime and corresponding center-of-mass energies  
 751 are summarized in Figure 3.2. During Run 2 from 2015-2018, the ATLAS detector recorded  
 752 a total of  $1.1 \times 10^{16}$   $pp$  collisions at  $\sqrt{s} = 13$  TeV, which corresponds to an integrated

753 luminosity of  $140 \pm 0.83\% \text{ fb}^{-1}$  that passed data quality control and are usable for analyses  
754 [89]. This is also the data set used for the analysis in this dissertation.

### 755 3.1.3 Physics at the LHC

756 The majority of physics studied at the LHC focus primarily on QCD proton-proton hard  
757 scattering processes and the resulting products. Hard scattering processes involve large  
758 momentum transfer compared to the proton mass e.g. top pair production ( $gg \rightarrow t\bar{t}$ ) and  
759 Higgs production ( $gg \rightarrow H$ ), and can be predicted using perturbative QCD [90]. Hard  
760 processes probe distance scales much lower than the proton radius and can be considered  
761 collisions between the constituent quarks and gluons i.e. partons. Soft processes involve  
762 lower momentum transfer between partons and are dominated by less well-understood non-  
763 perturbative QCD effects. The hard interaction between two partons are represented by a  
764 parton distribution function (PDF)  $f_i(x, Q^2)$ , which describes the probability of interacting  
765 with a constituent parton  $i$  that carries a fraction  $x$  of the external hadron's momentum  
766 when probed at a momentum scale of  $Q^2$  [91]. Other partons within the hadron that did  
767 not participate in the collision can still interact via lower momentum underlying-events  
768 (UE). The probability of a particular interaction occurring is defined as its cross-section  
769  $\sigma[b]$ . Figure 3.3 gives an overview of SM processes produced within the LHC and their  
770 cross-sections.

## 771 3.2 The ATLAS detector

772 One of the four main experiments at the LHC is ATLAS [27], designed as a multi-purpose  
773 detector for the role of studying high-energy physics in  $pp$  and heavy-ion collisions. ATLAS

## Standard Model Production Cross Section Measurements

Status: October 2023

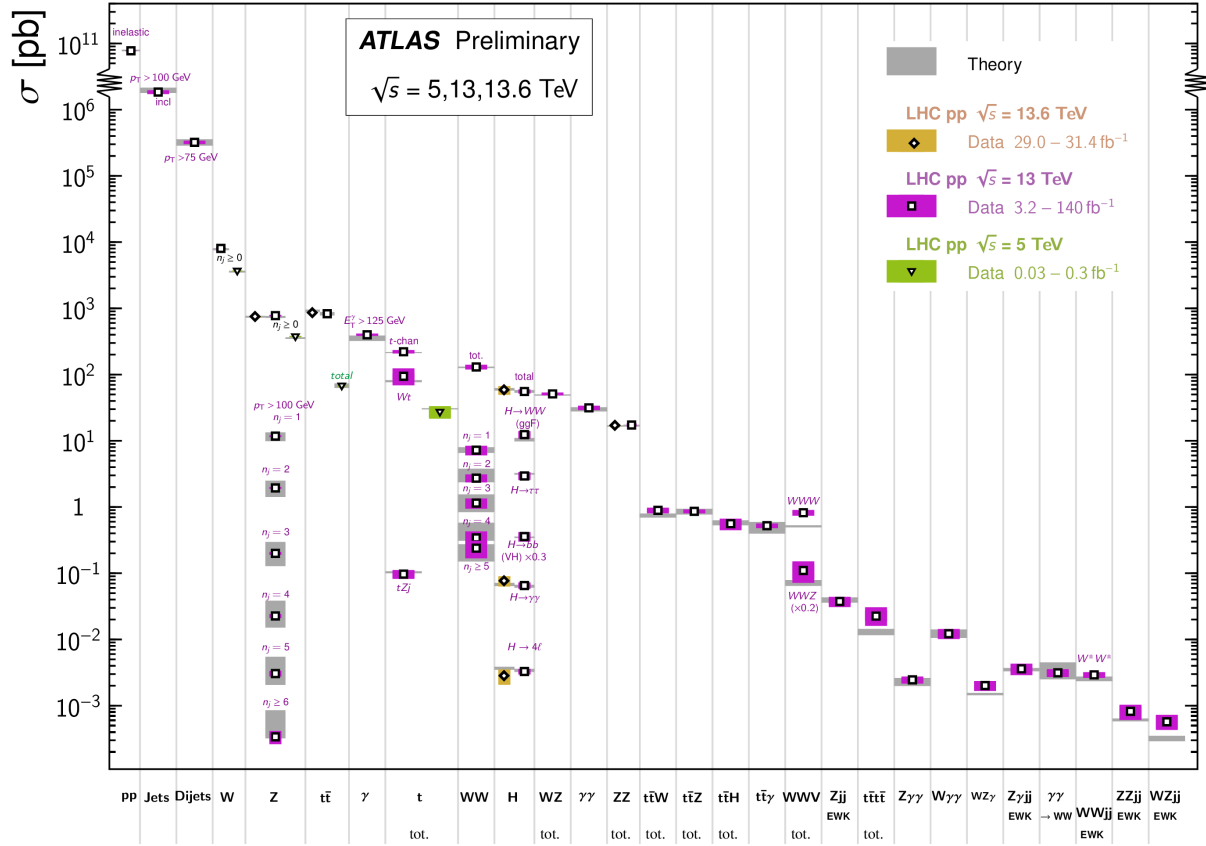


Figure 3.3: Summary of predicted and measured cross-section for SM processes at the LHC at different center-of-mass energies [92].

774 is a detector with symmetric cylindrical geometry with dimensions of 44 m in length and 25  
 775 m in diameter, covering a solid angle of almost  $4\pi$  around the collision point. The detector is  
 776 built concentrically around the beamline with the collision point at the center to maximally  
 777 capture signals produced by interactions. Figure 3.4 shows a slice of the ATLAS detector.  
 778 From the inside out, the main ATLAS subdetector system consists of the inner detector  
 779 (ID), calorimeter systems (electromagnetic and hadronic) and the muon spectrometer (MS).  
 780 The ATLAS detector uses a right-handed coordinate system [27] designed to align with  
 781 the geometry of a collision interaction, with the origin set at the interaction point, the  $z$ -axis

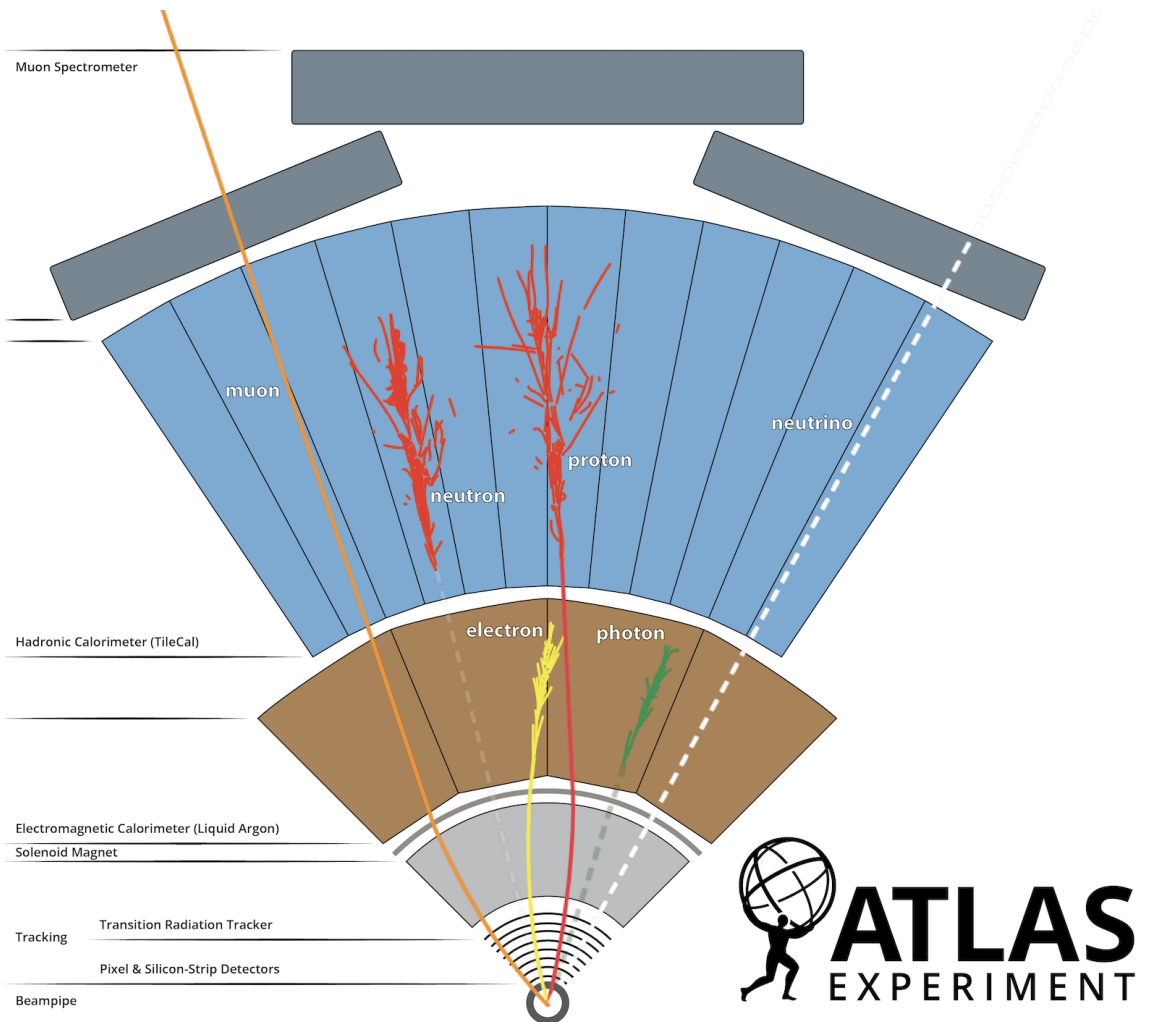


Figure 3.4: A cross section slice of the ATLAS detector showing different subsystems along with visualization of different types of particles traveling through the detector [93].

following (either of) the beamline and the  $x$ -axis pointing towards the center of the LHC ring. In cylindrical coordinates, the polar angle  $\theta$  is measured from the beam axis, and the azimuthal angle  $\phi$  is measured along the transverse plane ( $xy$ -plane) starting at the  $x$ -axis. Additional observables are defined for physics purposes: the pseudorapidity defined as  $\eta = -\ln \tan(\theta/2)$ ; angular distance within the detector defined as  $\Delta R = \sqrt{\Delta\eta^2 + \Delta\phi^2}$ ; and transverse momentum  $p_T$  (transverse energy  $E_T$ ) defined as the component of the particle's momentum (energy) projected onto the transverse plane.

### 789 3.2.1 Inner detector

790 The innermost part of ATLAS is the inner detector (ID) [27], constructed primarily for  
791 the purpose of measuring and reconstructing charged tracks within the  $|\eta| < 2.5$  region with  
792 high momentum resolution ( $\sigma_{p_T}/p_T = 0.05\% \pm 1\%$ ). Figure 3.5 shows the composition of  
793 the ID with three subsystems, the innermost being the pixel detector, then Semiconductor  
794 Tracker (SCT), and the Transition Radiation Tracker (TRT) on the outermost layer; all of  
795 which are surrounded by a solenoid magnet providing a magnetic field of 2 T.

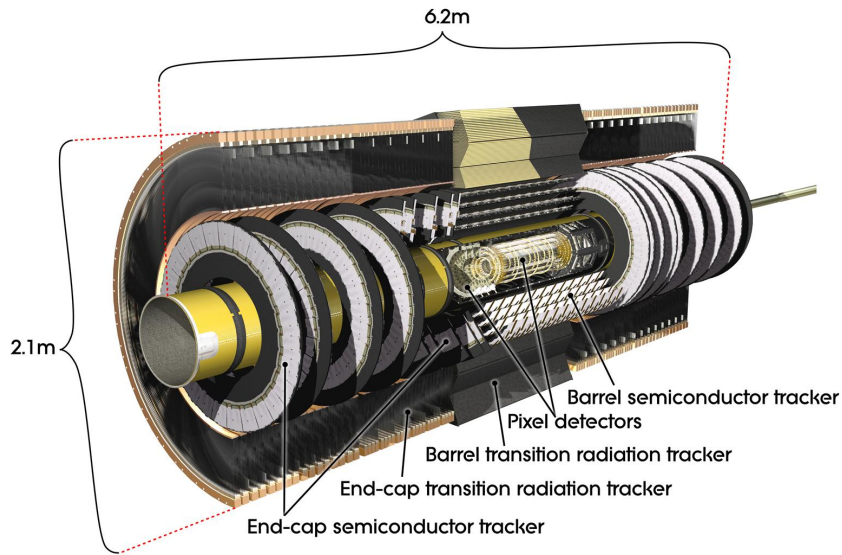


Figure 3.5: Cutaway illustration of the inner detector along with its subsystems [94].

### 796 Pixel detector

797 The pixel detector subsystem [27] consists of 250  $\mu\text{m}$  silicon semiconductor pixel layers  
798 with about 80.4 million readout channels, reaching a spatial resolution of 10  $\mu\text{m}$  in the  
799  $R - \phi$  (transverse) plane and 115  $\mu\text{m}$  in the  $z$ -direction for charged tracks. Charged particles  
800 passing through the pixel detector ionize the silicon layers and produce electron-hole pairs;

801 the electrons drift towards the detector's electrode under an applied electric field and the  
802 resulting electric signals are collected in read-out regions. The pixel detector is used primarily  
803 for impact parameter measurement, pile-up suppression, vertex finding and seeding for track  
804 reconstruction.

## 805 Semiconductor Tracker

806 The Semiconductor Tracker (SCT) [27] functions similarly to the pixel detector, using  
807 silicon semiconductor microstrips totaling about 6.3 million read-out channels, reaching a  
808 per layer resolution of 17  $\mu\text{m}$  in the  $R\text{-}\phi$  plane and 580  $\mu\text{m}$  in the  $z$ -direction [27]. The  
809 SCT plays an important role in precise  $p_{\text{T}}$  measurement of charged particles as well as track  
810 reconstruction.

## 811 Transition Radiation Tracker

812 The outermost layer of the ID, the Transition Radiation Tracker (TRT) [27], consists of  
813 layers of 4 mm diameter straw tubes filled with a xenon-based gas mixture and a 30  $\mu\text{m}$   
814 gold-plated wire in the center. The TRT contains a total of about 351 thousand readout  
815 channels with a resolution of 130  $\mu\text{m}$  for each straw tube in the  $R\text{-}\phi$  plane, and provides  
816 extended track measurement, particularly estimation of track curvature under the solenoidal  
817 magnetic field. Importantly, the TRT also serves to identify electrons through absorption of  
818 emitted transition-radiation within the Xe-based gas mixture.

### 819 3.2.2 Calorimeter systems

820 Surrounding the ID is the ATLAS calorimeter system [27] with electromagnetic (EM) and  
821 hadronic calorimeters, covering a range of  $|\eta| < 4.9$ . The calorimeters are sampling calorime-

822 ters with alternating absorbing layers to stop incoming particles and active layers to collect  
 823 read-out signals from energy deposits. Incoming particles passing through the calorimeters  
 824 interact with the absorbing layers, producing EM or hadronic showers of secondary particles.  
 825 The particle showers deposit energy in the corresponding layer of the calorimeters, which  
 826 are collected and aggregated to identify and reconstruct the original particle's energy and  
 827 direction. Figure 3.6 shows a schematic overview of the ATLAS calorimeter system.

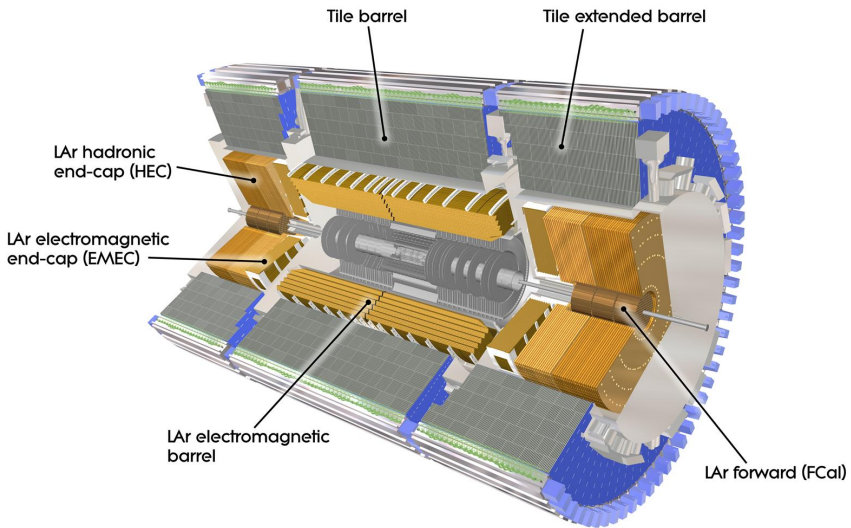


Figure 3.6: Cutaway illustration of the calorimeter system including the EM, hadronic and LAr forward calorimeters [95].

## 828 Electromagnetic calorimeter

829 The EM calorimeter [27] covers the innermost part of the calorimeter system, with lead  
 830 (Pb) absorbing layers and liquid argon (LAr) active layers to capture the majority of electrons  
 831 and photons exiting the ID. The EM calorimeter is divided into regions depending on  $\eta$   
 832 coverage: a barrel region ( $|\eta| < 1.475$ ), two endcap regions ( $1.375 < |\eta| < 3.2$ ) and a  
 833 transition region ( $1.372 < |\eta| < 1.52$ ). The endcap calorimeters are further divided into an

834 outer wheel region ( $1.372 < |\eta| < 2.5$ ) and an inner wheel region ( $2.5 < |\eta| < 3.2$ ) in order  
835 to provide precise coverage within the same  $\eta$  range as the ID. Overlap between the barrel  
836 and endcap regions compensates for the lower material density in the transition region.

837 **Hadronic calorimeter**

838 The hadronic calorimeter [27] covers up to  $|\eta| < 4.9$  and is comprised of three parts: the  
839 tile calorimeter with a barrel region ( $|\eta| < 1.0$ ) and extended barrel regions ( $0.8 < |\eta| < 1.7$ );  
840 the hadronic endcap calorimeter (HEC) covering  $1.5 < |\eta| < 3.2$ ; and the forward calorimeter  
841 (FCal) covering  $3.2 < |\eta| < 4.9$ . The tile calorimeter covers the EM calorimeter barrel region  
842 and uses steel as material for the absorbing layers with scintillating tiles for the active layers.  
843 Signals captured by scintillating tiles are read out from both sides using photomultiplier  
844 tubes. The HEC calorimeter covers the endcap regions of the EM calorimeter and uses a  
845 copper-LAr calorimeter layer scheme. The FCal is located close to the beamline providing  
846 coverage for particles traveling close to parallel with the beam axis. The subdetector contains  
847 three modules: one with copper absorbing layers optimized for EM measurements, and two  
848 with tungsten absorbing layers targeting hadronic cascades. All modules in the FCal use  
849 LAr as the active layer.

850 **3.2.3 Muon spectrometer**

851 Generally, the only particles that penetrate past the calorimeter layer are muons and  
852 neutrinos. The muon spectrometer (MS) [27] is situated on the outermost of the ATLAS  
853 detector and aims to track and measure muons within  $|\eta| < 2.7$ . The MS utilizes an array  
854 of toroid magnets to provide a magnetic field perpendicular to the muon trajectory, bending  
855 the track in order to measure its curvature. The magnetic field is powered by a large barrel

856 toroid ( $|\eta| < 1.4$ ) with strength of 0.5 T and two endcap toroid magnets ( $1.6 < |\eta| < 2.7$ ) of  
857 1 T. Both types contribute to the magnetic field in the transition region ( $1.4 < |\eta| < 1.6$ ).

858 To measure the muon itself, four types of large gas-filled chambers known as muon cham-  
859 bers [27] are designed and constructed for two main goals: triggering on potential muon  
860 candidates entering the MS and tracking their trajectories through the detector with high  
861 precision. The tracking system include Monitored Drift Tubes (MDTs), which record muon  
862 track information over the entire MS  $\eta$  range ( $|\eta| < 2.7$ ). The MDTs are built with multi-  
863 ple layers of drift tubes and filled with a mixture of 93% Ar and 7% CO<sub>2</sub>. Muons passing  
864 through drift tubes in the MDT ionize the gas within each tube; signals are then recorded  
865 as freed electrons drift to read-out channels under an applied electric field. In the forward  
866 region ( $2.0 < |\eta| < 2.7$ ), Cathode Strip Chambers (CSCs) are included along with MDTs.  
867 The CSCs are multiwire proportional chambers built with higher granularity and shorter  
868 drift time than the MDTs to handle tracking in an environment with high background rates.

869 The MS trigger system includes Resistive Plate Chambers (RPCs) [27], which provide  
870 triggering in the barrel region ( $|\eta| < 1.05$ ) using parallel electrode plates made of resistive  
871 materials with a gas mixture inbetween. High voltage is applied to the plates, accelerat-  
872 ing the electrons freed from ionized gas and creating a fast avalanche of charge, which is  
873 collected on external read-out strips almost instantaneously. Triggering and coarse position  
874 measurements in the endcap region ( $1.05 < |\eta| < 2.5$ ) is handled by Thin-Gap Chambers  
875 (TGCs). Similar to CSCs, TGCs are multiwire proportional chambers with a small wire gap  
876 ("thin-gap") and high applied voltage across the gap, resulting in fast response time giving  
877 TGCs the capabilities to identify muon candidates in real time.

878 **3.2.4 Trigger & data acquisition**

879 The LHC produces a colossal amount of collision data at a bunch crossing rate of 40 MHz  
880 with bunch spacing of 25 ns. The ATLAS Trigger and Data Acquisition (TDAQ) system [96]  
881 synchronously identifies and records interesting events for in-depth analysis. The ATLAS  
882 trigger system in Run 2 consists of two steps: Level-1 (L1) trigger and High-Level Trigger  
883 (HLT). Events failing any step in the trigger chain are permanently lost.

884 The L1 trigger hardware is divided into L1 calorimeter triggers (L1Calo) and L1 muon  
885 triggers (L1Muon) [96]. L1Calo trigger uses information from ATLAS calorimeter system  
886 to quickly identify signs of high  $p_T$  objects e.g. EM clusters, jets and missing transverse  
887 energy  $E_T^{\text{miss}}$  (section 4.4). Similarly, L1Muon uses information from the RPCs and TGCs  
888 of the MS to make quick decisions on potentially interesting muon candidates. Outputs  
889 from L1Calo and L1Muon are fed into the L1 topological trigger (L1Topo) for additional  
890 filtering based on event topology and multi-object correlation, allowing for more selective  
891 and physics-motivated triggering. Decisions from all three types of L1 triggers are provided  
892 as inputs for the Central Trigger Processor (CTP) for a final Level-1 Accept (L1A) decision.

893 The entire L1 trigger chain results in a 2.5  $\mu\text{s}$  latency and reduces the event rate to 100 kHz.

894 Events passing L1 triggers are sent to HLTs before being saved to offline storage at  
895 CERN data centers. HLTs are software-based triggers used for more complex and specific  
896 selections on physics objects required by targeted analysis goals, in turn requiring more  
897 computing power with longer latency. After HLT selections, the event rate is reduced to 1  
898 kHz on average [96]. Overall, the full trigger chain reduces the event rate for ATLAS by  
899 approximately a factor of  $4 \times 10^4$ .

# 900 Chapter 4. Particle Reconstruction & Identification

## 901

902 Activity within the ATLAS detector is recorded as raw electronic signals, which can  
903 be utilized by ATLAS reconstruction software to derive physics objects for analysis. This  
904 chapter describes the reconstruction and identification of basic objects (e.g. interaction  
905 vertices, tracks, topological clusters of energy deposits) and subsequently of complex physics  
906 objects i.e. particles and particle signatures.

### 907 4.1 Primary reconstruction

#### 908 4.1.1 Tracks

909 Charged particles traveling through the ATLAS detector deposit energy in different layers  
910 of the ID and MS. The ID track reconstruction software consists of two algorithm chains:  
911 inside-out and outside-in track reconstruction [97–99].

912 The inside-out algorithm is primarily used for the reconstruction of primary particles  
913 i.e. particles directly produced from  $pp$  collisions or decay products of short-lived particles.  
914 The process starts by forming space points from seeded hits in the silicon detectors within  
915 the pixel & SCT detectors. Hits further away from the interaction vertex are added to  
916 the track candidate using a combinatorial Kalman filter [100] pattern recognition algorithm.  
917 Track candidates are then fitted with a  $\chi^2$  filter [101] and loosely matched to a fixed-sized  
918 EM cluster. Successfully matched track candidates are re-fitted with a Gaussian-sum filter  
919 (GSF) [102], followed by a track scoring strategy to resolve fake tracks & hit ambiguity

920 between different tracks [103]. The track candidate is then extended to the TRT to form  
921 final tracks satisfying  $p_T > 400$  MeV. The outside-in algorithm handles secondary tracks  
922 mainly produced from long-lives particles or decays of primary particles by back-tracking  
923 from TRT segments, which are then extended inward to match silicon hits in the pixel and  
924 SCT detectors to form track reconstruction objects.

### 925 4.1.2 Vertices

926 Vertices represent the point of interaction or decay for particles within the ATLAS de-  
927 tector. Primary vertices (PVs) are defined as the point of collision for hard-scattering  $pp$   
928 interactions, while secondary or displaced vertices result from particle decays occurring at a  
929 distance from its production point.

930 Reconstruction of PVs is crucial to accurately profile the kinematic information of an  
931 event and form a basis for subsequent reconstruction procedures. Primary vertex recon-  
932 struction occurs in two stages: vertex finding and vertex fitting [104]. The vertex finding  
933 algorithm uses the spatial coordinates of reconstructed tracks to form the seed for a vertex  
934 candidate. An adaptive vertex fitting algorithm [105] then iteratively evaluates track-vertex  
935 compatibility to estimate a new best vertex position. Less compatible tracks are down-  
936 weighted in each subsequent iteration, and incompatible tracks are removed and can be  
937 used for another vertex seed; the process is repeated until no further PV can be found.  
938 All reconstructed vertices without at least two matched tracks are considered invalid and  
939 discarded.

940 Secondary vertex reconstruction uses the Secondary Vertex Finder (SVF) algorithm [106]  
941 which is primarily designed to reconstruct  $b$ - and  $c$ -hadrons for flavor tagging purposes. The  
942 SVF aims to reconstruct one secondary vertex per jet and only considers tracks that are

943 matched to a two-track vertex and contained within a  $p_T$ -dependent cone around the jet  
944 axis. The tracks are then used to reconstruct a secondary vertex candidate using an iterative  
945 process similar to the PV vertex fitting procedure.

946 **Pile-up**

947 At high luminosities, multiple interactions can be associated with one bunch crossing,  
948 resulting in many PVs. The effect is called pile-up [107], and usually result from soft QCD  
949 interactions. Pile-up can be categorized into two types: in-time pile-up, stemming from  
950 additional  $pp$  collisions in the same bunch crossing that is not the hard-scatter process; out-  
951 of-time pile-up, resulting from leftover energy deposits in the calorimeters from other bunch  
952 crossings.

953 **4.1.3 Topological clusters**

954 Topological clusters (topo-clusters) [108] consist of clusters of spatially related calorimeter  
955 cell signals. Topo-clusters are primarily used to reconstruct hadron- and jet-related objects  
956 in an effort to extract signal while minimizing electronic effects and physical fluctuations, and  
957 also allow for recovery of energy lost through bremsstrahlung or photon conversions. Cells  
958 with signal-to-noise ratio  $\zeta_{\text{cell}}^{\text{EM}}$  passing a primary seed threshold are seeded into a dynamic  
959 topological cell clustering algorithm as part of a proto-cluster. Neighboring cells satisfying a  
960 cluster growth threshold are collected into the proto-cluster. If a cell is matched to two proto-  
961 clusters, the clusters are merged. Two or more local signal maxima in a cluster satisfying  
962  $E_{\text{cell}}^{\text{EM}} > 500 \text{ MeV}$  suggest the presence of multiple particles in close proximity, and the cluster  
963 is split accordingly to maintain good resolution of the energy flow. The process continues  
964 iteratively until all cells with  $\zeta_{\text{cell}}^{\text{EM}}$  above a principal cell filter level have been matched to a

965 cluster.

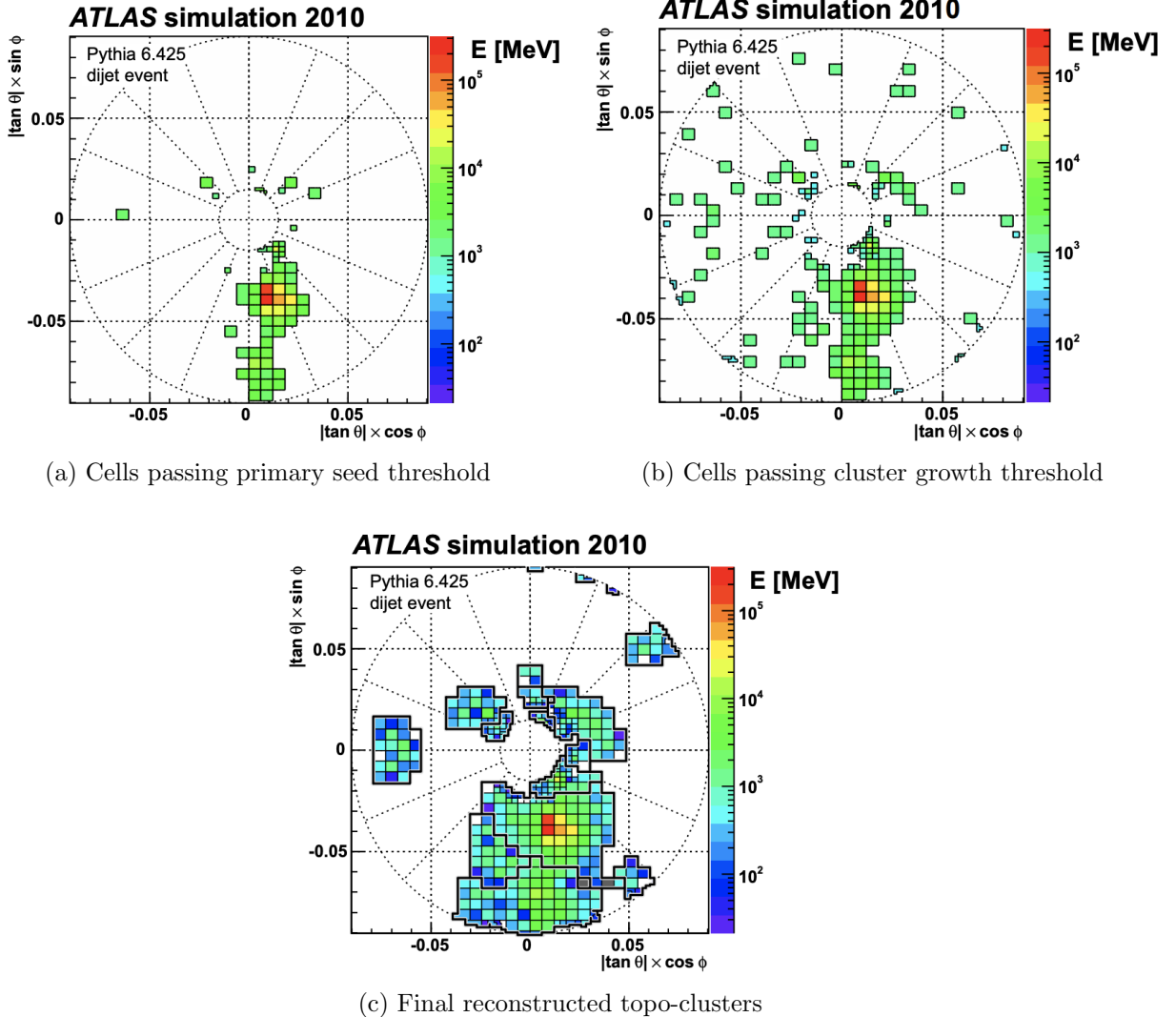


Figure 4.1: Stages of topo-cluster formation corresponding to each threshold. In (a), proto-clusters are seeded from cells with adequate signal significance  $\zeta_{\text{cell}}^{\text{EM}}$ . The clusters are further merged and split in (b) following a predefined cluster growth threshold. The process stops in (c) when all sufficiently significant signal hits have been matched to a cluster [108].

## 966 4.2 Jets

967 Quarks, gluons and other hadrons with non-neutral color charge cannot be observed  
968 individually due to QCD color confinement, which forces a non-color-neutral hadron to

almost immediately undergo hadronization, producing a collimated cone of color-neutral hadrons defined as a jet. Jet signals can be used to reconstruct and indirectly observe the quarks or gluons from which the jet originated in the original hard-scattering process.

### 4.2.1 Jet reconstruction

The ATLAS jet reconstruction pipeline is largely carried out using a particle flow (PFlow) algorithm combined with an anti- $k_t$  jet clustering algorithm. The PFlow algorithm [109] utilizes topo-clusters along with information from both the calorimeter systems and the ID in order to make use of the tracker system’s advantages in low-energy momentum resolution and angular resolution. First, the energy from charged particles is removed from the calorimeter topo-clusters; then, it is replaced by particle objects created using the remaining energy in the calorimeter and tracks matched to topo-clusters. The ensemble of ”particle flow objects” and corresponding matched tracks are used as inputs for the iterative anti- $k_t$  algorithm [110].

The main components of the anti- $k_t$  algorithm involve the distance  $d_{ij}$  between two jet candidates  $i$  and  $j$ , and the distance  $d_{iB}$  between the harder jet candidate of the two (defined as  $i$ ) and the beamline  $B$ . If  $d_{ij} < d_{iB}$ , then the two jet candidates are combined and returned to the pool of candidates; otherwise, jet candidate  $i$  is considered a jet and removed from the pool. The distance  $d_{ij}$  is inversely proportional to a predefined radius parameter  $\Delta R$  in order to control reconstruction quality for small- $R$  and large- $R$  jets. This analysis uses  $\Delta R = 0.4$  to better handle heavily collimated small- $R$  jets resulting from parton showers.

The anti- $k_t$  jets so far have only been reconstructed at the EM level and need to be calibrated to match the energy scale of jets reconstructed at particle level. This is done via a MC-based jet energy scale (JES) calibration sequence, along with further calibrations

992 to account for pile-up effects and energy leakage. The full JES calibration sequence is  
 993 shown in Figure 4.2. All calibrations except origin correction are applied to the jet's four-  
 994 momentum i.e. jet  $p_T$ , energy and mass. Afterwards, a jet energy resolution (JER) [111]  
 995 calibration step is carried out in a similar manner to JES to match the resolution of jets in  
 996 dijet events. To further suppress pile-up effects, a neural-network based jet vertex tagger  
 997 (NNJvt) discriminant was developed based on the previous jet vertex tagger (JVT) algorithm  
 998 [107] and applied to low- $p_T$  reconstructed jets.

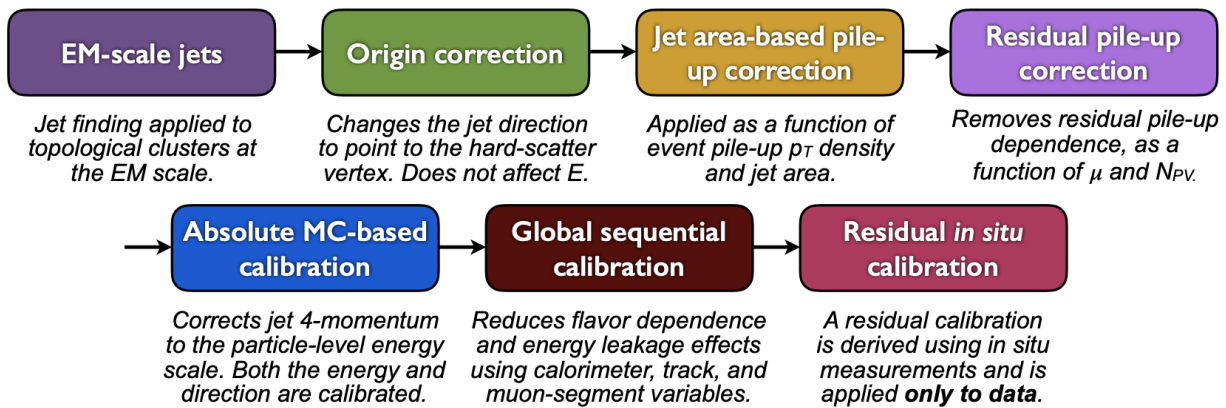


Figure 4.2: Jet energy scale calibration sequence for EM-scale jets [112].

### 999 4.2.2 Flavor tagging

1000 Identifying and classifying hadronic jets are important tasks for ATLAS physics, for  
 1001 example analyses involving Higgs decays  $H \rightarrow b\bar{b}$  or top quarks. Flavor tagging or  $b$ -tagging  
 1002 is the process of identifying jets containing  $b$ -hadrons,  $c$ -hadrons, light-hadrons ( $uds$ -hadrons)  
 1003 or jets from hadronically decaying  $\tau$  leptons. Distinguishing  $b$ -jets is possible due to their  
 1004 characteristically long lifetime ( $\tau \approx 1.5$  ps), displaced secondary decay vertex and high decay  
 1005 multiplicity.

1006 Usage of  $b$ -tagging in this analysis is done via five operating points (OPs), corresponding

1007 to 65%, 70%, 77%, 85% and 90%  $b$ -jet tagging efficiency  $\varepsilon_b$  in simulated  $t\bar{t}$  events, in order  
1008 from the tightest to loosest discriminant cut point. The OPs are defined by placing selections  
1009 on the tagger output to provide a predefined  $\varepsilon_b$  level; the selection cuts act as a variable  
1010 trade-off between  $b$ -tagging efficiency and  $b$ -jet purity i.e.  $c$ - or light-jet rejection. For this  
1011 analysis, a jet is considered  $b$ -tagged if it passes the 85% OP. The  $b$ -tagged jet is then  
1012 assigned a pseudo-continuous  $b$ -tagging (PCBT) score, which quantifies a jet's ability to  
1013 satisfy different OPs. The score can take integer values between 1 and 6, where a score of 6  
1014 is assigned to jets passing all OP thresholds; a score of 2 for jets that pass only the tightest  
1015 OP (90%); and a score of 1 for jets that pass no OP. A value of -1 is also defined for any jet  
1016 that does not satisfy  $b$ -tagging criteria. Since the targeted  $t\bar{t}t\bar{t}$  final states contain at least  
1017 four  $b$ -hadrons from top and  $W$  decays, a  $b$ -tagging OP of 85% is used to maintain high  
1018 purity during  $b$ -tagged jet selections in the signal region.

## 1019 **GN2 $b$ -tagging algorithm**

1020 For this analysis,  $b$ -jets are identified and tagged with the GN2v01  $b$ -tagger [113]. The  
1021 GN2 algorithm uses a Transformer-based model [114] modified to incorporate domain knowl-  
1022 edge and additional auxiliary physics objectives: grouping tracks with a common vertex and  
1023 predicting the underlying physics process for a track. The network structure is shown in  
1024 Figure 4.3. The GN2  $b$ -tagger form the input vector by concatenating 2 jet variables and  
1025 19 track reconstruction variables (for up to 40 tracks), normalized to zero mean and unit  
1026 variance. The output consists of a track-pairing output layer of size 2, a track origin clas-  
1027 sification layer of 7 categories, and a jet classification layer of size 4 for the probability of  
1028 each jet being a  $b$ -,  $c$ -, light- or  $\tau$ -jet respectively. For  $b$ -tagging purpose, a discriminant is

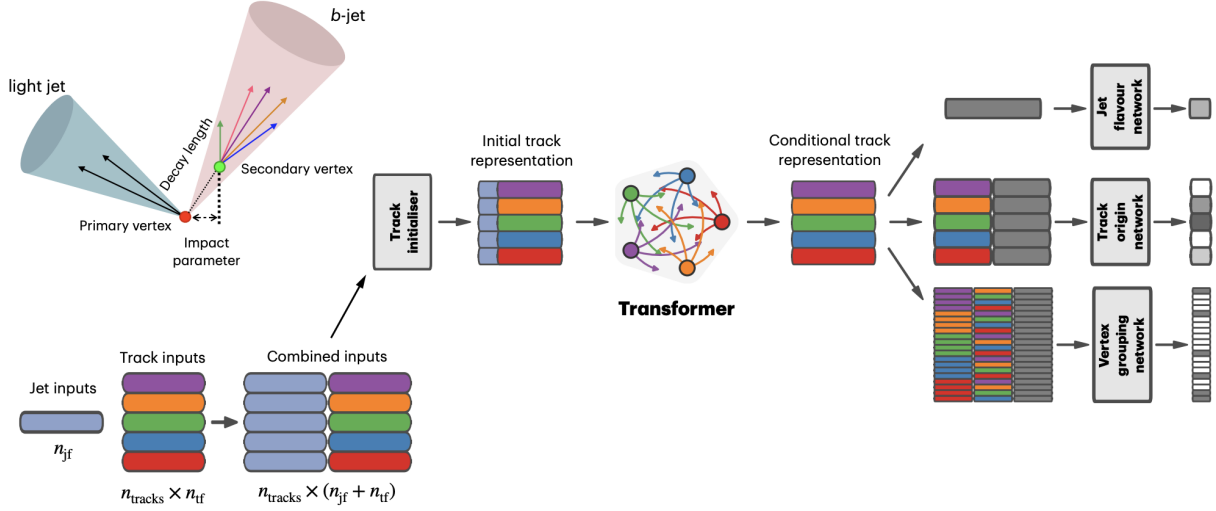


Figure 4.3: Overview of the GN2 architecture. The number of jet and track features are represented by  $n_{jf}$  and  $n_{tf}$  respectively. The global jet representation and track embeddings output by the Transformer encoder are used as inputs for three task-specific networks [113].

1029 defined using these four outputs

$$D_b = \ln \left( \frac{p_b}{f_c p_c + f_\tau p_\tau + (1 - f_c - f_\tau)p_{\text{light}}} \right) \quad (4.1)$$

1030 where  $p_x$  is the probability of the jet being an  $x$ -jet as predicted by GN2, and  $f_c, f_\tau$  are tun-  
 1031 able free parameters controlling balance between  $c$ - and light-jet rejection. Simulated SM  $t\bar{t}$   
 1032 and BSM  $Z'$  events from  $pp$  collisions were used as training and evaluation samples. In order  
 1033 to minimize bias, both  $b$ - and light-jet samples are re-sampled to match  $c$ -jet distributions.  
 1034 Figure 4.4 shows the performance of GN2 compared to the previous convolutional neural  
 1035 network-based standard  $b$ -tagging algorithm DL1d, in terms of  $c$ -, light- and  $\tau$ -jet rejection  
 1036 as a function of  $b$ -tagging efficiency. The network gives a factor of 1.5-4 improvement in  
 1037 experimental applications compared to DL1d [113], without dependence on the choice of  
 1038 MC event generator or inputs from low-level flavor tagging algorithm.

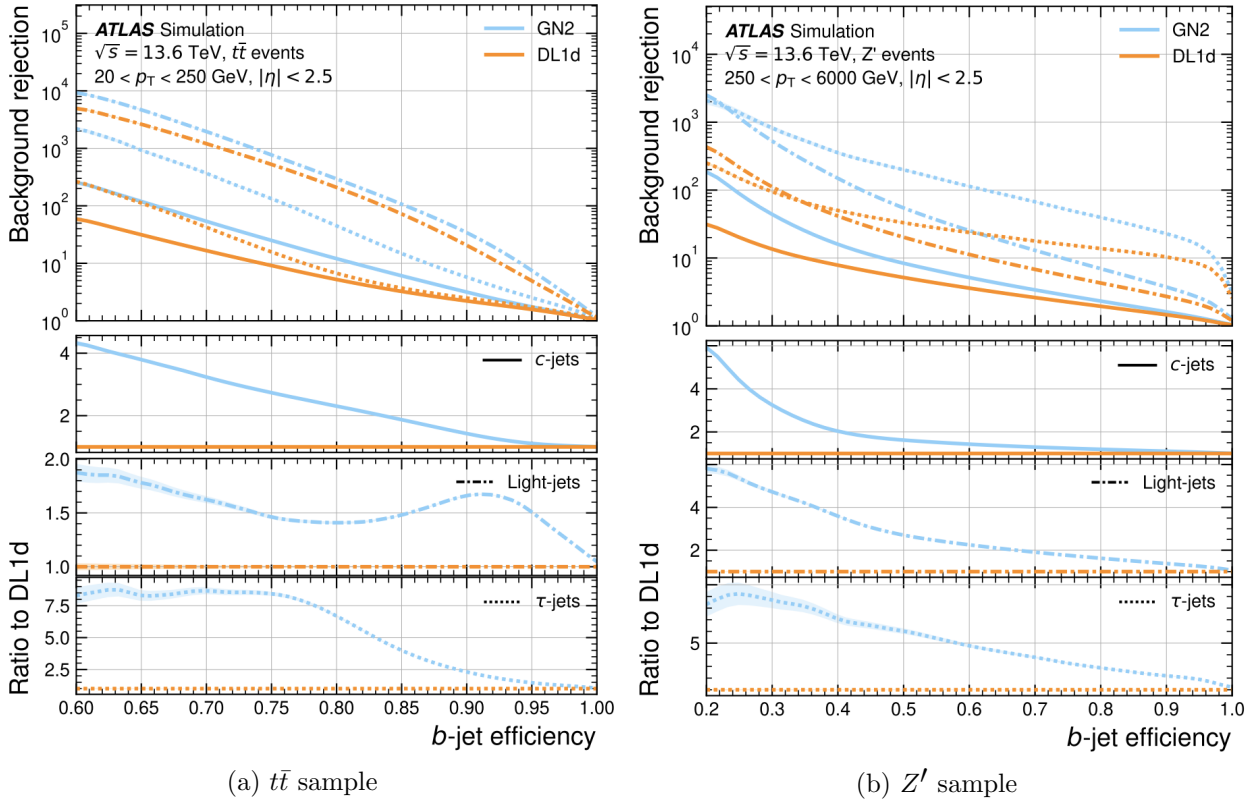


Figure 4.4: The  $c$ -, light- and  $\tau$ -jet rejection rate as a function of  $b$ -tagging efficiency for GN2 and DL1d using (a) jets in the  $t\bar{t}$  sample, and (b) jets in the  $Z'$  sample. The performance ratios of GN2 to DL1d are shown in the bottom panels [113].

### 1039 Efficiency calibration

1040 Due to imperfect description of detector response and physics modeling effects in simu-  
 1041 lation, the  $b$ -tagging efficiency predicted by MC simulation  $\varepsilon_b^{\text{sim}}$  requires a correction factor  
 1042 to match the efficiency measured in collision data  $\varepsilon_b^{\text{data}}$ . The correction scale factors (SFs)  
 1043 are defined as  $\text{SF} = \varepsilon_b^{\text{data}} / \varepsilon_b^{\text{sim}}$  and are determined by data-to-MC calibration using samples  
 1044 enriched in dileptonic  $t\bar{t}$  decays [115]. The resulting SFs are applied to MC simulated jets  
 1045 individually.

## 1046 4.3 Leptons

1047 Lepton reconstruction in ATLAS involves electron and muon reconstruction since tau  
1048 decays quickly, and depending on decay mode can be reconstructed using either jets or light  
1049 leptons. From here on out within this dissertation, leptons will be used exclusively to refer to  
1050 electrons and muons. Leptons can be classified into two categories: prompt leptons resulting  
1051 from heavy particle decays and non-prompt leptons resulting from detector or reconstruction  
1052 effects, or from heavy-flavor hadron decays.

### 1053 4.3.1 Electrons

1054 Electrons leave energy signature in the detector by interacting with the detector materials  
1055 and losing energy in the form of bremsstrahlung photons. A bremsstrahlung photon can  
1056 produce an electron-positron pair which can itself deposit signals in the detector, creating a  
1057 cascade of particles that can leave multiple of either tracks in the ID or EM showers in the  
1058 calorimeters, all of which are considered part of the same EM topo-cluster. Electron signal  
1059 signature has three characteristic components: localized energy deposits in the calorimeters,  
1060 multiple tracks in the ID and compatibility between the above tracks and energy clusters in  
1061 the  $\eta \times \phi$  plane [116]. Electron reconstruction in ATLAS follows these steps accordingly.

1062 Seed-cluster reconstruction and track reconstruction are performed sequentially in ac-  
1063 cordance with the iterative topo-clustering algorithm and track reconstruction method de-  
1064 scribed in section 4.1. The seed-cluster and GSF-refitted track candidate not associated  
1065 with a conversion vertex are matched to form an electron candidate. The cluster energy is  
1066 then calibrated using multivariate techniques on data and simulation to match the original  
1067 electron energy.

1068 **Electron identification**

1069 Additional LH-based identification selections using ID and EM calorimeter information  
1070 are implemented to further improve the purity of reconstructed electrons in the  $|\eta| < 2.47$  re-  
1071 gion of the detector [116]. The electron LH function is built with the signal being prompt elec-  
1072 trons and background being objects with similar signature to prompt electrons i.e. hadronic  
1073 jet deposits, photon conversions or heavy-flavor hadron decays. Three identification OPs  
1074 are defined for physics analyses: *Loose*, *Medium* and *Tight*, optimized for 9 bins in  $|\eta|$  and  
1075 12 bins in  $E_T$  with each OP corresponding to a fixed efficiency requirement for each bin.  
1076 For typical EW processes, the target efficiencies for *Loose*, *Medium* and *Tight* start at 93%,  
1077 88% and 80% respectively and increase with  $E_T$ . Similar to  $b$ -tagging OPs, the electron  
1078 identification OPs represent a trade-off in signal efficiency and background rejection. The  
1079 electron efficiency are estimated using tag-and-probe method on samples of  $J/\Psi \rightarrow ee$  and  
1080  $Z \rightarrow ee$  [116]. The *Tight* electron identification OP is used for this analysis.

1081 **Electron isolation**

1082 A characteristic distinction between prompt electrons and electrons from background  
1083 processes is the relative lack of activity in both the ID and calorimeters within an  $\Delta\eta \times \Delta\phi$   
1084 area surrounding the reconstruction candidate. Calorimeter-based and track-based electron  
1085 isolation variables [116] are defined to quantify the amount of activity around the electron  
1086 candidate using topo-clusters and reconstructed tracks respectively.

1087 Calorimeter-based isolation variables  $E_T^{\text{cone}XX}$  are computed by first summing the energy  
1088 of topo-clusters with barycenters falling within a cone of radius  $\Delta R = \sqrt{(\Delta\eta)^2 + (\Delta\phi)^2} =$   
1089  $XX/100$  around the direction of the electron candidate. The final isolation variables are

obtained by subtracting from the sum the energy belonging to the candidate electron at the core of the cone, then applying corrections for pile-up effects and energy leakage outside of the core. Similar to calorimeter-based variables, track-based isolation variables  $p_T^{\text{varcone}XX}$  are calculated by summing all track  $p_T$  within a cone of radius  $\Delta R$  around the electron candidate, minus the candidate's contribution. The cone radius is variable as a function of  $p_T$  and is described as

$$\Delta R \equiv \min \left( \frac{10}{p_T}, \Delta R_{\max} \right), \quad (4.2)$$

where  $p_T$  is expressed in GeV and  $\Delta R_{\max}$  is the maximum cone size, defined to account for closer proximity of decay products to the electron in high-momentum heavy particle decays. Four isolation operating points are implemented to satisfy specific needs by physics analyses: *Loose*, *Tight*, *HighPtCaloOnly* and *Gradient* [116]. For this analysis, electrons isolation uses *Tight* requirements.

## 1101 Electron charge misidentification

Charge misidentification is a crucial irreducible background, particularly for analyses with electron charge selection criteria. Electron charge is determined by the curvature of the associated reconstructed track, and misidentification of charge can occur via either an incorrect curvature measurement or an incorrectly matched track. Inaccurate measurement is more likely for high energy electrons due to the small curvature in track trajectories at high  $p_T$ , while track matching error usually results from bremsstrahlung pair-production generating secondary tracks in close proximity [116]. Suppression of charge misidentification background in Run 2 is additionally assisted by a boosted decision tree discriminant known

1110 as the Electron Charge ID Selector (ECIDS). For this analysis, all electrons are required to  
1111 pass the ECIDS criterion.

### 1112 4.3.2 Muons

1113 Muons act as minimum-ionizing particles, leaving tracks in the MS or characteristics  
1114 energy deposits in the calorimeter and can be reconstructed globally using information from  
1115 the ID, MS and calorimeters. Five reconstruction strategies corresponding to five muon  
1116 types [117] are utilized in ATLAS:

- Combined (CB): the primary ATLAS muon reconstruction method. Combined muons  
1117 are first reconstructed using MS tracks then extrapolated to include ID tracks (outside-in strategy). A global combined track fit is performed on both MS and ID tracks.
- Inside-out combined (IO): complementary to CB reconstruction. IO muon tracks are  
1118 extrapolated from ID to MS, then fitted with MS hits and calorimeter energy loss in a  
1119 combined track fit.
- MS extrapolated (ME): ME muons are defined as muons with a MS track that cannot  
1120 be matched to an ID track using CB reconstruction. ME muons allow extension of  
1121 muon reconstruction acceptance to regions not covered by the ID ( $2.5 < |\eta| < 2.7$ )
- Segment-tagged (ST): ST muons are defined as a successfully matched ID track that  
1122 satisfies tight angular matching criteria to at least one reconstructed MDT or CSC  
1123 segment when extrapolated to the MS. MS reconstruction is used primarily when  
1124 muons only crossed one layer of MS chambers.
- Calorimeter-tagged (CT): CT muons are defined as an ID track that can be matched to

1131 energy deposits consistent with those of a minimum-ionizing particle when extrapolated  
1132 through the calorimeter. CT reconstruction extends acceptance range to regions in the  
1133 MS with sparse instrumentation ( $|\eta| < 0.1$ ) with a higher  $p_T$  threshold of 5 GeV,  
1134 compared to the 2 GeV threshold used by other muon reconstruction algorithms due  
1135 to large background contamination at the low  $p_T$  range of  $15 < p_T < 100$  GeV [118].

## 1136 Muon identification

1137 Reconstructed muons are further filtered by identification criteria to select for high-  
1138 quality prompt muons. Requirements include number of hits in the MS and ID, track fit  
1139 properties and compatibility between measurements of the two systems. Three standard  
1140 OPs (*Loose*, *Medium*, *Tight*) are defined to better match the needs of different physics  
1141 analyses concerning prompt muon  $p_T$  resolution, identification efficiency and non-prompt  
1142 muon rejection. The default identification OP for ATLAS physics and also the OP used in  
1143 this analysis is *Medium*, which provides efficiency and purity suitable for a wide range of  
1144 studies while minimizing systematic uncertainties [117].

## 1145 Muon isolation

1146 Muons from heavy particle decays are often produced in an isolated manner compared to  
1147 muons from semileptonic decays, and is therefore an important tool for background rejection  
1148 in many physics analyses. Muon isolation strategies are similar to that of electron in section  
1149 4.3.1, with track-based and calorimeter-based isolation variables. Seven isolation OPs are  
1150 defined using either or both types of isolation variables, balancing between prompt muon  
1151 acceptance and non-prompt muon rejection. The full definition and description for the muon  
1152 isolation OPs are detailed in Ref. [117].

## 1153 4.4 Missing transverse momentum

1154 Collisions at the LHC happen along the  $z$ -axis of the ATLAS coordination system between  
1155 two particle beam of equal center-of-mass energy. By conservation of momentum, the sum of  
1156 transverse momenta of outgoing particles should be zero. A discrepancy between measured  
1157 momentum and zero would then suggest the presence of undetectable particles, which would  
1158 consist of either SM neutrinos or some unknown BSM particles, making missing transverse  
1159 momentum ( $E_T^{\text{miss}}$ ) an important observable to reconstruct.

1160 Reconstructing  $E_T^{\text{miss}}$  utilizes information from fully reconstructed leptons, photons, jets  
1161 and other matched track-vertex objects not associated with a prompt object (soft signals),  
1162 defined with respect to the  $x(y)$ -axis as

$$E_{x(y)}^{\text{miss}} = - \sum_{i \in \{\text{hard objects}\}} p_{x(y),i} - \sum_{j \in \{\text{soft signals}\}} p_{x(y),j}, \quad (4.3)$$

1163 where  $p_{x(y)}$  is the  $x(y)$ -component of  $p_T$  for each particle [119]. The following observables  
1164 can then be defined:

$$\begin{aligned} \mathbf{E}_T^{\text{miss}} &= (E_x^{\text{miss}}, E_y^{\text{miss}}), \\ E_T^{\text{miss}} &= |\mathbf{E}_T^{\text{miss}}| = \sqrt{(E_x^{\text{miss}})^2 + (E_y^{\text{miss}})^2}, \\ \phi^{\text{miss}} &= \tan^{-1}(E_y^{\text{miss}}/E_x^{\text{miss}}), \end{aligned} \quad (4.4)$$

1165 where  $E_T^{\text{miss}}$  represents the magnitude of the missing transverse energy vector  $\mathbf{E}_T^{\text{miss}}$ , and  
1166  $\phi^{\text{miss}}$  its direction in the transverse plane. The vectorial sum  $\mathbf{E}_T^{\text{miss}}$  can be broken down into

$$\mathbf{E}_T^{\text{miss}} = - \underbrace{\sum_{\text{selected electrons}} \mathbf{p}_T^e - \sum_{\text{selected muons}} \mathbf{p}_T^\mu - \sum_{\text{accepted photons}} \mathbf{p}_T^\gamma - \sum_{\text{accepted } \tau\text{-leptons}} \mathbf{p}_T^\tau}_{\text{hard term}} - \underbrace{\sum_{\text{accepted jets}} \mathbf{p}_T^{\text{jet}} - \sum_{\text{unused tracks}} \mathbf{p}_T^{\text{track}}}_{\text{soft term}}. \quad (4.5)$$

1167 Two OPs are defined for  $E_T^{\text{miss}}$ , *Loose* and *Tight*, with selections on jet  $p_T$  and JVT criteria  
1168 [120]. The *Tight* OP is used in this analysis; *Tight* reduces pile-up dependence of  $E_T^{\text{miss}}$   
1169 by removing the phase space region containing more pile-up than hard-scatter jets, at the  
1170 expense of resolution and scale at low pile-up,

## 1171 4.5 Overlap removal

1172 Since different objects are reconstructed independently, it is possible for the same de-  
1173 tector signals to be used to reconstruct multiple objects. An overlap removal strategy is  
1174 implemented to resolve ambiguities; the overlap removal process for this analysis applies  
1175 selections in Table 4.1 sequentially, from top to bottom.

Table 4.1: Overlap removal process for this analysis, applied sequentially from top to bottom.

| Remove   | Keep     | Matching criteria  |
|----------|----------|--|
| Electron | Electron | Shared ID track, $p_{T,1}^e < p_{T,2}^e$                         |
| Muon     | Electron | Shared ID track, CT muon   |
| Electron | Muon     | Shared ID track  |
| Jet      | Electron | $\Delta R < 0.2$   |
| Electron | Jet      | $\Delta R < 0.4$   |
| Jet      | Muon     | ( $\Delta R < 0.2$ or ghost-associated) & $N_{\text{track}} < 3$ |
| Muon     | Jet      | $\Delta R < \min(0.4, 0.04 + 10\text{GeV}/p_T^\mu)$              |

## 1176 4.6 Object definition

1177 Table 4.2 summarizes the selections on physics objects used in this analysis. Each se-  
1178 lection comes with associated calibration scale factors (SFs) to account for discrepancies  
1179 between data and MC simulation, and are applied multiplicatively to MC event weights.

Table 4.2: Summary of object selection criteria used in this analysis.  $\ell_0$  refers to the leading lepton in the event.

| Selection                                   | Electrons                                  | Muons                    | Jets   |
|---|--|--------------------------|--|
| $p_T$ [GeV]                                 | $> 15$<br>$p_T(\ell_0) > 28$               | $> 15$                   | $> 20$   |
| $ \eta $                                    | $1.52 \leq  \eta  < 2.47$<br>$< 1.37$      | $< 2.5$                  | $< 2.5$  |
| Identification                              | <i>TightLH</i><br>pass ECIDS ( $ee/e\mu$ ) | <i>Medium</i>            | NNJvt <i>FixedEffPt</i><br>( $p_T < 60$ , $ \eta  < 2.4$ ) |
| Isolation                                   | <i>Tight_VarRad</i>                        | <i>PflowTight_VarRad</i> |  |
| Track-vertex assoc.                         |  |                          |  |
| $ d_0^{\text{BL}}(\sigma) $                 | $< 5$                                      | $< 3$                    |  |
| $ \Delta z_0^{\text{BL}} \sin \theta $ [mm] | $< 0.5$                                    | $< 0.5$                  |  |

# 1180 Chapter 5. Data & Simulated Samples

## 1181 5.1 Data samples

1182 Data samples used in this analysis were collected by the ATLAS detector during the Run  
1183 2 data-taking campaign between 2015-2018. The samples contain  $pp$  collisions at center-of-  
1184 mass energy of  $\sqrt{s} = 13$  TeV with 25 ns bunch-spacing, which corresponds to an integrated  
1185 luminosity of  $140 \text{ fb}^{-1}$  with an uncertainty of 0.83% [89]. The HLT trigger strategy is similar  
1186 to that of previous  $t\bar{t}t\bar{t}$  observation analysis [44] and include single lepton and dilepton  
1187 triggers. Calibration for di-muon and electron-muon triggers were not ready for the samples  
1188 used in this analysis, and are therefore not included. Events are also required to contain at  
1189 least one lepton matched to the corresponding object firing the trigger. Triggers utilized in  
1190 this analysis are summarized in Table 5.1, with efficiency close to 100% when used together.

## 1191 5.2 Monte Carlo samples

1192 Monte Carlo simulated samples are used to estimate signal acceptance before unblinding,  
1193 profile the physics background for the analysis and to study object optimizations. Simulated  
1194 samples for this analysis use are generated from ATLAS generalized MC20a/d/e samples for  
1195 Run 2, using full detector simulation (FS) and fast simulation (AF3) to simulate detector  
1196 response. MC samples used and simulation processes are summarized in Table 5.2.

Table 5.1: Summary of all HLT triggers used in this analysis. Events are required to pass at least one trigger.

| Trigger                           | Data period |      |      |      |
|-----------------------------------|-------------|------|------|------|
|                                   | 2015        | 2016 | 2017 | 2018 |
| Single electron triggers          |             |      |      |      |
| HLT_e24_lhmedium_L1EM20VH         | ✓           | -    | -    | -    |
| HLT_e60_lhmedium                  | ✓           | -    | -    | -    |
| HLT_e120_lhloose                  | ✓           | -    | -    | -    |
| HLT_e26_lhtight_nod0_ivarloose    | -           | ✓    | ✓    | ✓    |
| HLT_e60_lhmedium_nod0             | -           | ✓    | ✓    | ✓    |
| HLT_e140_lhloose_nod0             | -           | ✓    | ✓    | ✓    |
| Di-electron triggers              |             |      |      |      |
| HLT_2e12_lhloose_L12EM10VH        | ✓           | -    | -    | -    |
| HLT_2e17_lhvloose_nod0            | -           | ✓    | -    | -    |
| HLT_2e24_lhvloose_nod0            | -           | -    | ✓    | ✓    |
| HLT_2e17_lhvloose_nod0_L12EM15VHI | -           | -    | -    | ✓    |
| Single muon trigger               |             |      |      |      |
| HLT_mu20_iloose_L1MU15            | ✓           | -    | -    | -    |
| HLT_mu40                          | ✓           | -    | -    | -    |
| HLT_mu26_ivarmedium               | -           | ✓    | ✓    | ✓    |
| HLT_mu50                          | -           | ✓    | ✓    | ✓    |

### <sup>1197</sup> 5.2.1 $t\bar{t}Z'$ signal samples

<sup>1198</sup> Signal  $t\bar{t}Z'$  samples were generated based on the simplified topophilic resonance model in  
<sup>1199</sup> section 2.2.1. Six  $Z'$  mass points were utilized for the generation of the signal sample: 1000,  
<sup>1200</sup> 1250, 1500, 2000, 2500 and 3000 GeV. The top- $Z'$  coupling  $c_t$  is chosen to be 1 for a narrow  
<sup>1201</sup> resonance peak, and the chirality angle  $\theta$  is chosen to be  $\pi/4$  to suppress loop production  
<sup>1202</sup> of  $Z'$ . The samples were then generated with MADGRAPH5\_AMC@NLO v.3.5.0 [121] at  
<sup>1203</sup> LO with the NNPDF3.1LO [122] PDF set interfaced with PYTHIA8 [123] using A14 tune  
<sup>1204</sup> and NNPDF2.3lo PDF set for parton showering and hadronization. The resonance width is  
<sup>1205</sup> calculated to be 4% for  $c_t = 1$ .

Table 5.2: Summary of all Monte-Carlo samples used in this analysis.  $V$  refers to an EW ( $W^\pm/Z/\gamma^*$ ) or Higgs boson. Matrix element (ME) order refers to the order in QCD of the perturbative calculation. Tune refers to the underlying-event tune of the parton shower (PS) generator.

| Process   | ME Generator          | ME Order                   | ME PDF             | PS | Tune                 | Sim. |
|---|-----------------------|----------------------------|--------------------|----|----------------------|------|
| <b>Signals</b>  |                       |                            |                    |    |                      |      |
| $t\bar{t}Z'$  | MADGRAPH5_AMC@NLO LO  |                            | NNPDF3.1LO         |    | PYTHIA8 A14          | FS   |
| <b><math>t\bar{t}t\bar{t}</math> and <math>t\bar{t}\bar{t}</math></b> |                       |                            |                    |    |                      |      |
| $t\bar{t}t\bar{t}$  | MADGRAPH5_AMC@NLO NLO |                            | NNPDF3.0nlo        |    | PYTHIA8 A14          | AF3  |
|   | MADGRAPH5_AMC@NLO NLO |                            | MMHT2014 LO        |    | HERWIG7 H7-UE-MMHT   | AF3  |
|   | SHERPA                | NLO                        | NNPDF3.0nnlo       |    | HERWIG7 SHERPA       | FS   |
| $t\bar{t}\bar{t}$   | MADGRAPH5_AMC@NLO LO  |                            | NNPDF2.3lo         |    | PYTHIA8 A14          | AF3  |
| <b><math>t\bar{t}V</math></b>   |                       |                            |                    |    |                      |      |
| $t\bar{t}H$   | POWHEGBOX v2          | NLO                        | NNPDF3.0nlo        |    | PYTHIA8 A14          | FS   |
|   | POWHEGBOX v2          | NLO                        | NNPDF3.0nlo        |    | HERWIG7 H7.2-Default | FS   |
| $t\bar{t}(Z/\gamma^*)$  | MADGRAPH5_AMC@NLO NLO |                            | NNPDF3.0nlo        |    | PYTHIA8 A14          | FS   |
|   | SHERPA                | NLO                        | NNPDF3.0nnlo       |    | SHERPA SHERPA        | FS   |
| $t\bar{t}W$   | SHERPA                | NLO                        | NNPDF3.0nnlo       |    | SHERPA SHERPA        | FS   |
|   | SHERPA                | LO                         | NNPDF3.0nnlo       |    | SHERPA SHERPA        | FS   |
| <b><math>t\bar{t}</math> and Single-Top</b>                           |                       |                            |                    |    |                      |      |
| $t\bar{t}$  | POWHEGBOX v2          | NLO                        | NNPDF3.0nlo        |    | PYTHIA8 A14          | FS   |
| $tW$  | POWHEGBOX v2          | NLO                        | NNPDF3.0nlo        |    | PYTHIA8 A14          | FS   |
| $t(q)b$   | POWHEGBOX v2          | NLO                        | NNPDF3.0nlo (s)    |    | PYTHIA8 A14          | FS   |
|   |                       |                            | NNPDF3.0nlo 4f (t) |    |                      | FS   |
| $tWZ$   | MADGRAPH5_AMC@NLO NLO |                            | NNPDF3.0nlo        |    | PYTHIA8 A14          | FS   |
| $tZ$  | MADGRAPH5_AMC@NLO LO  |                            | NNPDF3.0nlo 4f     |    | PYTHIA8 A14          | FS   |
| <b><math>t\bar{t}VV</math></b>  |                       |                            |                    |    |                      |      |
| $t\bar{t}WW$  | MADGRAPH5_AMC@NLO LO  |                            | NNPDF3.0nlo        |    | PYTHIA8 A14          | FS   |
| $t\bar{t}WZ$  | MADGRAPH              | LO                         | NNPDF3.0nlo        |    | PYTHIA8 A14          | AF3  |
| $t\bar{t}HH$  | MADGRAPH              | LO                         | NNPDF3.0nlo        |    | PYTHIA8 A14          | AF3  |
| $t\bar{t}WH$  | MADGRAPH              | LO                         | NNPDF3.0nlo        |    | PYTHIA8 A14          | AF3  |
| $t\bar{t}ZZ$  | MADGRAPH              | LO                         | NNPDF3.0nlo        |    | PYTHIA8 A14          | AF3  |
| <b><math>V(VV)+\text{jets}</math> and <math>VH</math></b>             |                       |                            |                    |    |                      |      |
| $V+\text{jets}$   | SHERPA                | NLO                        | NNPDF3.0nnlo       |    | SHERPA SHERPA        | FS   |
| $VV+\text{jets}$  | SHERPA                | NLO                        | NNPDF3.0nnlo       |    | SHERPA SHERPA        | FS   |
|   |                       | LO ( $gg \rightarrow VV$ ) |                    |    |                      | FS   |
| $VVV+\text{jets}$   | SHERPA                | NLO                        | NNPDF3.0nnlo       |    | SHERPA SHERPA        | FS   |
| $VH$  | POWHEGBOX v2          | NLO                        | NNPDF3.0aznlo      |    | PYTHIA8 A14          | FS   |

<sub>1206</sub> **5.2.2 Background samples**

<sub>1207</sub> **SM  $t\bar{t}t\bar{t}$  background**

<sub>1208</sub> The nominal SM  $t\bar{t}t\bar{t}$  sample was generated with MADGRAPH5\_AMC@NLO [121] at  
<sub>1209</sub> NLO in QCD with the NNPDF3.0nlo [122] PDF set and interfaced with PYTHIA8.230 [123]  
<sub>1210</sub> using A14 tune [124]. Decays for top quarks are simulated at LO with MADSPIN [125,  
<sub>1211</sub> 126] to preserve spin information, while decays for  $b$ - and  $c$ -hadrons are simulated with  
<sub>1212</sub> EVTGEN v1.6.0 [127]. The renormalization and factorization scales  $\mu_R$  and  $\mu_F$  are set  
<sub>1213</sub> to  $1/4\sqrt{m^2 + p_T^2}$ , which represents the sum of transverse mass of all particles generated  
<sub>1214</sub> from the ME calculation [128]. The ATLAS detector response was simulated with AF3.  
<sub>1215</sub> Additional auxiliary  $t\bar{t}t\bar{t}$  samples are also generated to evaluate the impact of generator and  
<sub>1216</sub> PS uncertainties as shown in 5.2.

<sub>1217</sub>  **$t\bar{t}W$  background**

<sub>1218</sub> Nominal  $t\bar{t}W$  sample was generated using SHERPA v2.2.10 [129] at NLO in QCD with  
<sub>1219</sub> the NNPDF3.0nnlo [122] PDF with up to one extra parton at NLO and two at LO, which  
<sub>1220</sub> are matched and merged with the SHERPA PS based on Catani-Seymour dipole factorization  
<sub>1221</sub> [130] using the MEPS@NLO prescription [131–134] and a merging scale of 30 GeV. Higher-  
<sub>1222</sub> order ME corrections are provided in QCD by the OpenLoops 2 library [135–137] and in  
<sub>1223</sub> EW from  $\mathcal{O}(\alpha^3) + \mathcal{O}(\alpha_S^2\alpha^2)$  (LO3 & NLO2) via two sets of internal event weights. An  
<sub>1224</sub> alternative sample with only EW corrections at LO from  $\mathcal{O}(\alpha_S\alpha^3)$  (NLO3) diagrams were  
<sub>1225</sub> also simulated with the same settings.

1226  **$t\bar{t}(Z/\gamma^*)$  background**

1227 Nominal  $t\bar{t}(Z/\gamma^*)$  samples were generated separately for different ranges of dilepton in-  
1228 variant mass  $m_{\ell\ell}$  to account for on-shell and off-shell  $Z/\gamma^*$  production. Sample for  $m_{\ell\ell}$   
1229 between 1 and 5 GeV was produced using MADGRAPH5\_AMC@NLO [121] at NLO with  
1230 the NNPDF3.0nlo [122] PDF set, interfaced with PYTHIA8.230 [123] using A14 tune [124] and  
1231 NNPDF2.3l0 PDF set. Sample for  $m_{\ell\ell} < 5$  GeV was produced with SHERPA v2.2.10 [129]  
1232 at NLO using NNPDF3.0nnlo PDF set. To account for generator uncertainty, an alternative  
1233  $m_{\ell\ell} > 5$  GeV sample was generated with identical settings to the low  $m_{\ell\ell}$  sample. The  
1234 ATLAS detector response was simulated with full detector simulation (FS).

1235  **$t\bar{t}H$  background**

1236 Generation of  $t\bar{t}H$  background was done using POWHEGBox [138–141] at NLO in QCD  
1237 with the NNPDF3.0nlo PDF [122] set. The nominal sample is interfaced with PYTHIA8.230  
1238 [123] using the A14 tune [124] and the NNPDF2.3l0 [142] PDF set. Detector response is  
1239 simulated using FS. An alternative  $t\bar{t}H$  sample generated similarly, but instead interfaced  
1240 with HERWIG7.2.3 [143, 144] to study the impact of parton shower and hadronization model.  
1241 Detector response for the alternative sample is simulated using AF3.

1242  **$t\bar{t}t$  background**

1243 The  $t\bar{t}t$  sample is generated using MADGRAPH5\_AMC@NLO [121] at LO in QCD, inter-  
1244 faced with PYTHIA8 [123] using the A14 tune [124]. The sample is produced in the five-flavor  
1245 scheme [145] to prevent LO interference with  $t\bar{t}t\bar{t}$ .

1246  **$t\bar{t}$  background**

1247 The  $t\bar{t}$  sample is modeled with POWHEGBox [138–141] at NLO in QCD with the NNPDF3.0nlo  
1248 [122] PDF set and the  $h_{\text{damp}}$  parameter set to  $1.5m_{\text{top}}$  [146]. Events are interfaced with  
1249 PYTHIA8.230 [123] using the A14 tune [124] and the NNPDF2.3lō [142] PDF set.

1250 **Single-top ( $tW$  &  $t(q)b$ ) background**

1251 Single-top  $tW$ -associated production is modeled using the POWHEGBox generator [138–  
1252 141] at NLO in QCD in the five-flavor scheme [145] with the NNPDF3.0nlo [122] PDF set. In-  
1253 terference with  $t\bar{t}$  production [146] is handled using the diagram removal scheme [147]. Single-  
1254 top  $t(q)b$  production is modeled using the POWHEGBox generator at NLO in QCD with the  
1255 s-channel production modeled in the five-flavor scheme with the NNPDF3.0nlo PDF set, while  
1256 the t-channel production is modeled in the four-flavor scheme with the NNPDF3.0nlo 4f [122]  
1257 PDF set. The  $t\bar{t}WW$  contributions are normalized to NLO theoretical cross section. All  
1258 single-top samples are interfaced with PYTHIA8.230 [123] using the A14 tune [124] and the  
1259 NNPDF2.3lō [142] PDF set.

1260  **$tWZ$  +jets background**

1261 The  $tWZ$  sample is generated using MADGRAPH5\_AMC@NLO [121] at NLO in QCD  
1262 with the NNPDF3.0nlo [122] PDF set, interfaced with PYTHIA8.212 [123] using the A14 tune  
1263 [124] and the NNPDF2.3lō [142] PDF set.

1264  **$tZ$  &  $t\bar{t}VV$  background**

1265 Production of  $tZ$  is modeled using MADGRAPH5\_AMC@NLO [121] at NLO in QCD  
1266 with scale of  $H_T/6$  and the NNPDF3.0nlo 4f [122] PDF set. Production of  $t\bar{t}WW$  is modeled

1267 using `MADGRAPH5_AMC@NLO` [121] at LO, while production of  $t\bar{t}WZ$ ,  $t\bar{t}HH$ ,  $t\bar{t}WH$  and  
1268  $t\bar{t}ZZ$  are modeled using `MADGRAPH` at LO. All  $t\bar{t}VV$  samples use the `NNPDF3.0nlo` [122]  
1269 PDF set, and all samples in this section are interfaced with `PYTHIA8` [123] using the A14  
1270 tune [124].

### 1271 Single boson ( $V$ ) +jets background

1272 Production of  $V$ +jets is modeled with `SHERPA v2.2.10` [129] using NLO ME for up to two  
1273 jets and LO ME for up to four jets, with the `NNPDF3.0nlo` [122] PDF set. Matrix elements  
1274 are calculated with the Comix [148] and OpenLoops libraries [135, 136] and matched with  
1275 the `SHERPA` PS based on Catani-Seymour dipole factorization [130] using the MEPS@NLO  
1276 prescription [131–134]. The sample is normalized to the NNLO [149] theoretical cross section.

### 1277 Diboson ( $VV$ ) +jets background

1278 Diboson samples are simulated with `SHERPA v2.2.14` [129] with the `NNPDF3.0nlo` [122]  
1279 PDF set. Fully leptonic and semileptonic final states are generated using NLO ME for up to  
1280 one extra parton and LO ME for up to three extra parton emissions. Loop-induced processes  
1281 are generated using LO ME for up to one extra parton. Matrix elements are matched and  
1282 merged with the `SHERPA` PS based on Catani-Seymour dipole factorization [130] using the  
1283 MEPS@NLO prescription [131–134]. Virtual QCD ME corrections are provided by the  
1284 OpenLoops library [135, 136].

### 1285 Triboson ( $VVV$ ) +jets background

1286 The triboson sample is modeled with `SHERPA v2.2.10` [129] using factorized gauge boson  
1287 decays. Matrix elements for the inclusive process at NLO and up to two extra partons at

1288 LO are matched and merged with the SHERPA PS based on Catani-Seymour dipole factor-  
1289 ization [130] using the MEPS@NLO prescription [131–134]. Virtual QCD ME corrections  
1290 are provided by the OpenLoops library [135, 136].

1291 ***VH* background**

1292 Generation of  $WH$  and  $ZH$  samples is performed using PowhegBox [138–141] at NLO  
1293 with the NNPDF3.0aznlo [122] PDF set, interfaced with PYTHIA8.230 [123] using the A14  
1294 tune [124] and the NNPDF2.3lo [142] PDF set.

<sub>1295</sub> **Chapter 6. Analysis Strategy**

<sub>1296</sub> **6.1 Event selection**

<sub>1297</sub> Events for the analysis first are preselected following a list of criteria to optimize for event  
<sub>1298</sub> quality and background rejection. The following criteria are applied sequentially from top  
<sub>1299</sub> to bottom along with cleaning and veto cuts

<sub>1300</sub> 1. **Good Run List (GRL)**: data events must be part of a predefined list of suitable  
<sub>1301</sub> runs and luminosity blocks [[150](#)].

<sub>1302</sub> 2. **Primary vertex**: events must have at least one reconstructed vertex matched to 2 or  
<sub>1303</sub> more associated tracks with  $p_T > 500$  MeV.

<sub>1304</sub> 3. **Trigger**: events must be selected by at least one trigger in Table 5.1.

<sub>1305</sub> 4. **Kinematic selection**: events must have exactly two *Tight* leptons with the same  
<sub>1306</sub> electric charge, or at least three *Tight* leptons of any charge. The leading lepton must  
<sub>1307</sub> have  $p_T > 28$  GeV, and all leptons must satisfy  $p_T > 15$  GeV.

<sub>1308</sub> Events are separated into two channels based on the number of leptons: same-sign di-  
<sub>1309</sub> lepton (SS2L) for events with exactly two leptons of the same charge, or multilepton (ML)  
<sub>1310</sub> for events with three or more leptons. The channels are further separated into regions defined  
<sub>1311</sub> in section 6.2 to prepare for analysis.

<sub>1312</sub> Additional selections are applied based on the lepton flavors present. In the SS2L channel,  
<sub>1313</sub> if both leptons are electrons, the invariant mass  $m_{ll}$  must satisfy  $m_{ll} < 81$  GeV and  $m_{ll} > 101$   
<sub>1314</sub> GeV to suppress background involving  $Z$ -bosons. In the ML channel, the same criteria must  
<sub>1315</sub> be satisfied for every opposite-sign same-flavor pair of leptons in an event.

### 1316 6.1.1 Event categorization

1317 Simulated events are categorized using truth information of leptons ( $e/\mu$ ) and their orig-  
1318 inating MC particle (mother-particle). Each lepton can be classified as either prompt or  
1319 non-prompt, with non-prompt leptons further categorized for background estimation pur-  
1320 poses. If an event contains only prompt leptons, the event is classified as its correspond-  
1321 ing process. If the event contains one non-prompt lepton, the event is classified as the corre-  
1322 sponding type of the non-prompt lepton. If the event contains more than one non-prompt  
1323 lepton, the event is classified as other.

1324 • **Prompt:** if the lepton originates from  $W/Z/H$  boson decays, or from a mother-  
1325 particle created by a final state photon.

1326 • **Non-prompt:**

1327 – **Charge-flip ( $e$  only):** if the reconstructed charge of the lepton differs from that  
1328 of the first mother-particle.

1329 – **Material conversion ( $e$  only):** if the lepton originated from a photon conversion  
1330 and the mother-particle is an isolated prompt photon, non-isolated final state  
1331 photon, or heavy boson.

1332 –  **$\gamma^*$ -conversion ( $e$  only):** if the lepton originated from a photon conversion and  
1333 the mother-particle is a background electron.

1334 – **Heavy flavor decay:** if the lepton originated from a  $b$ - or  $c$ -hadron.

1335 – **Fake:** if the lepton originated from a light- or  $s$ -hadron, or if the truth type of  
1336 the lepton is hadron.

1337 – **Other:** any lepton that does not belong to one of the above categories.

1338 **6.2 Analysis regions**

1339 Events are selected and categorized into analysis regions belonging to one of two types:  
1340 control regions (CRs) enriched in background events, and signal regions (SRs) enriched in  
1341 signal events. This allows for the examination and control of backgrounds and systematic  
1342 uncertainties, as well as study of signal sensitivities. The signal is then extracted from the  
1343 SRs with a profile LH fit using all regions. The full selection criteria for each region are  
1344 summarized in Table 6.1. The post-fit background compositions in different CRs and SR  
1345 sub-regions are shown in Figure 6.1.

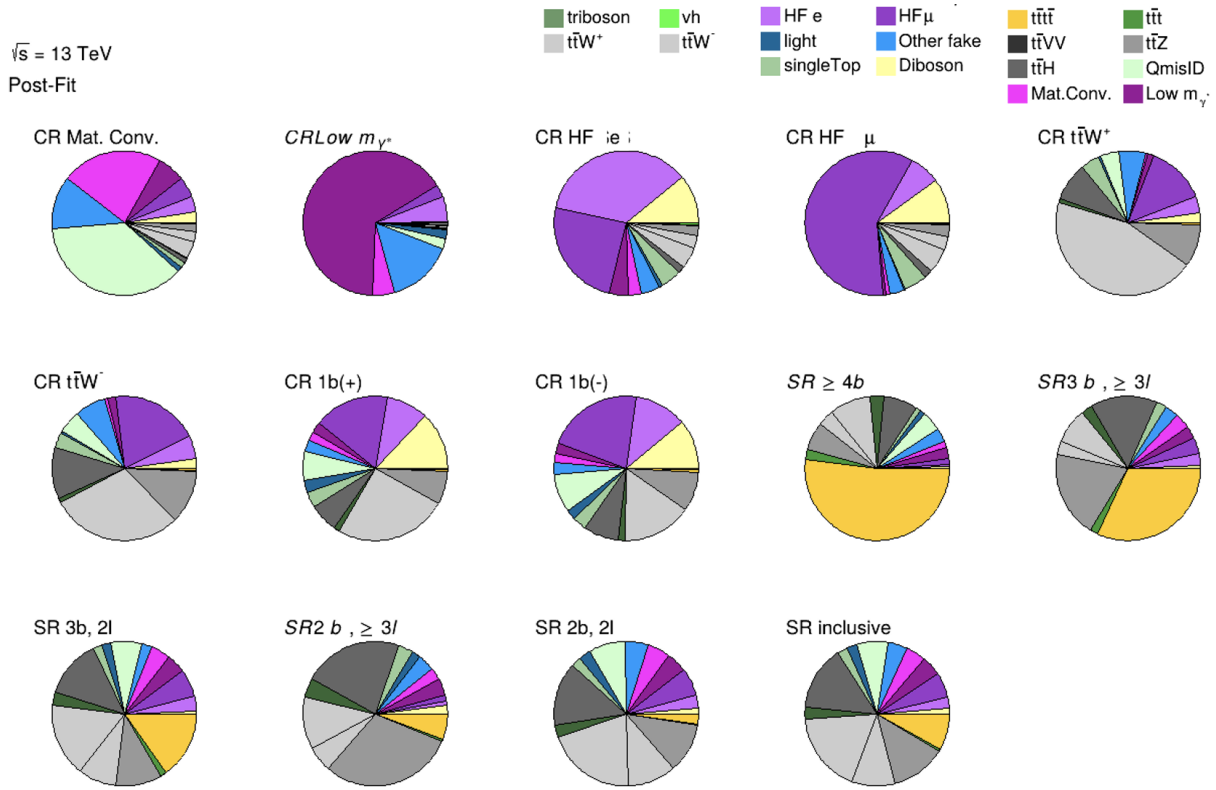


Figure 6.1: Post-fit background composition in each analysis region and sub-region. The fit was performed using ideal pseudo-datasets (Asimov data) in the SR.

Table 6.1: Definitions of signal, control and validation regions (VR) used in this analysis.  $N_{\text{jets}}$  and  $N_b$  refers to the number of jets and number of  $b$ -tagged jets respectively.  $\ell_1$  refers to the leading lepton,  $\ell_2$  refers to the subleading lepton and so on.  $H_T$  refers to the  $p_T$  scalar sum of all leptons and jets in the event.  $m_{\ell\ell}$  refers to the dilepton invariant mass, which must not coincide with the  $Z$ -boson mass range of 81-101 GeV for SS2L+3L events.

| Region                | Channel               | $N_{\text{jets}}$ | $N_b$    | Other selections  | Fitted variable                 |
|-----------------------|-----------------------|-------------------|----------|---|---------------------------------|
| CR Low $m_{\gamma^*}$ | SS $e\ell$            | [4, 6)            | $\geq 1$ | $\ell_1/\ell_2$ is from virtual photon decay<br>$\ell_1 + \ell_2$ not from material conversion  | event yield                     |
| CR Mat. Conv.         | SS $e\ell$            | [4, 6)            | $\geq 1$ | $\ell_1/\ell_2$ is from material conversion<br>$\ell_1 + \ell_2$ not conversion candidates  | event yield                     |
| CR HF $\mu$           | $\ell\mu\mu$          | $\geq 1$          | 1        | $100 < H_T < 300$ GeV<br>$E_T^{\text{miss}} > 35$ GeV<br>total charge = $\pm 1$   | $p_T(\ell_3)$                   |
| CR HF $e$             | $e\ell\ell$           | $\geq 1$          | 1        | $\ell_1 + \ell_2$ not conversion candidates<br>$100 < H_T < 275$ GeV<br>$E_T^{\text{miss}} > 35$ GeV<br>total charge = $\pm 1$          | $p_T(\ell_3)$                   |
| CR $t\bar{t}W^+$      | SS $\ell\mu$          | $\geq 4$          | $\geq 2$ | $ \eta(e)  < 1.5$<br>for $N_b = 2$ : $H_T < 500$ GeV or $N_{\text{jets}} < 6$<br>for $N_b \geq 3$ : $H_T < 500$ GeV<br>total charge > 0 | $N_{\text{jets}}$               |
| CR $t\bar{t}W^-$      | SS $\ell\mu$          | $\geq 4$          | $\geq 2$ | $ \eta(e)  < 1.5$<br>for $N_b = 2$ : $H_T < 500$ GeV or $N_{\text{jets}} < 6$<br>for $N_b \geq 3$ : $H_T < 500$ GeV<br>total charge < 0 | $N_{\text{jets}}$               |
| CR 1b(+)              | SS2L+3L               | $\geq 4$          | 1        | $\ell_1 + \ell_2$ not from material conversion<br>$H_T > 500$ GeV<br>total charge > 0   | $N_{\text{jets}}$               |
| CR 1b(-)              | SS2L+3L               | $\geq 4$          | 1        | $\ell_1 + \ell_2$ not from material conversion<br>$H_T > 500$ GeV<br>total charge < 0   | $N_{\text{jets}}$               |
| VR $t\bar{t}Z$        | 3L $\ell^\pm\ell^\mp$ | $\geq 4$          | $\geq 2$ | $m_{\ell\ell} \in [81, 101]$ GeV  | $N_{\text{jets}}, m_{\ell\ell}$ |
| VR $t\bar{t}W +1b$    | SS2L+3L               |                   |          | CR $t\bar{t}W^\pm$    CR 1b( $\pm$ )  | $N_{\text{jets}}$               |
| VR $t\bar{t}W +1b+SR$ | SS2L+3L               |                   |          | CR $t\bar{t}W^\pm$    CR 1b( $\pm$ )    SR  | $N_{\text{jets}}$               |
| SR                    | SS2L+3L               | $\geq 6$          | $\geq 2$ | $H_T > 500$ GeV<br>$m_{\ell\ell} \notin [81, 101]$ GeV  | $H_T$                           |

<sub>1346</sub> **6.2.1 Signal regions**

<sub>1347</sub> All events selected for the SR must satisfy the following criteria:

- <sub>1348</sub> • Contains 6 or more jets, with at least 2 jets  $b$ -tagged at the 85% OP.
- <sub>1349</sub> • Scalar sum of the transverse momenta of all leptons and jets  $H_T > 500$  GeV.
- <sub>1350</sub> • Dilepton invariant mass  $m_{\ell\ell}$  does not coincide with the  $Z$ -boson mass range of 81 – 101
- <sub>1351</sub> GeV

<sub>1352</sub> The SR is further divided into sub-regions by the number of  $b$ -tagged jets and leptons  
<sub>1353</sub> present to study signal behavior and sensitivity with respect to the selection variables.

Table 6.2: Definitions of SR sub-regions. Events are sorted into different sub-regions based on the number of  $b$ -tagged jets and leptons present.

| Sub-region | Selection criteria |              |
|------------|--------------------|--------------|
|            | $b$ -jets          | leptons      |
| SR 2b2l    | $N_b = 2$          | $N_l = 2$    |
| SR 2b3l4l  | $N_b = 2$          | $N_l \geq 3$ |
| SR 3b2l    | $N_b = 3$          | $N_l = 2$    |
| SR 3b3l4l  | $N_b = 3$          | $N_l \geq 3$ |
| SR 4b      | $N_b \geq 4$       |              |

<sub>1354</sub> **Signal extraction**

<sub>1355</sub> Signal extraction in the SR is performed via a binned profile likelihood (LH) fit as de-  
<sub>1356</sub> scribed in section 8.1 using  $H_T$  as the discriminant observable. The discriminant observable  
<sub>1357</sub> for a LH fit serves as the set of observed data upon which the LH function is constructed.  
<sub>1358</sub> Ideally, the chosen observable shows significant separation between the functional forms of  
<sub>1359</sub> the signal and background distributions, allowing for effective separation of the two. Fig-  
<sub>1360</sub> ure 6.2 shows several pre-fit kinematic distributions in the inclusive SR. From empirical

1361 optimization studies,  $H_T$  possesses good discriminating power compared to other observ-  
1362 ables constructed using event-level information.

1363 **6.2.2 Control regions**

1364 Control regions are defined for each background to be enriched in the targeted process, in  
1365 order to maximize the background's purity and minimize contamination from other sources  
1366 within the region. This helps to constrain and reduce correlation between background nor-  
1367 malization factors in the final fit. Fit variables and selection criteria are determined via  
1368 optimization studies performed on CRs that aimed to achieve the largest discriminating  
1369 power possible between the target background and other event types.

1370  **$t\bar{t}W$  background CRs**

1371 Theoretical modeling for  $t\bar{t}W + \text{jets}$  background in the phase space of this analysis suffers  
1372 from large uncertainties, especially at high jet multiplicities [151]. A data-driven method was  
1373 employed in a similar manner to the SM  $t\bar{t}t\bar{t}$  observation analysis [44] to mitigate this effect  
1374 and is described in further details in section 6.3.3. The method necessitates the definition of  
1375 two groups of dedicated CRs to estimate the flavor composition and normalization of  $t\bar{t}W$   
1376 + jets background: CR  $t\bar{t}W + \text{jets}$  to constrain flavor composition, and CR 1b to constrain  
1377 the jet multiplicity spectrum. These are further split into CR  $t\bar{t}W^\pm$  and CR 1b( $\pm$ ) to  
1378 account for the pronounced asymmetry in  $t\bar{t}W$  production from  $pp$  collisions at the LHC.  
1379 The cross section of  $t\bar{t}W^+$  production is approximately twice that of  $t\bar{t}W^-$  [152] due to the  
1380 combination of the main  $W^+$  emission process being  $u \rightarrow dW^+$  and the ratio of two  $u$ -quarks  
1381 to one  $d$ -quark in the proton.

1382 Events in CR  $t\bar{t}W^\pm$  are required to contain at least two  $b$ -tagged jets similar to the SR

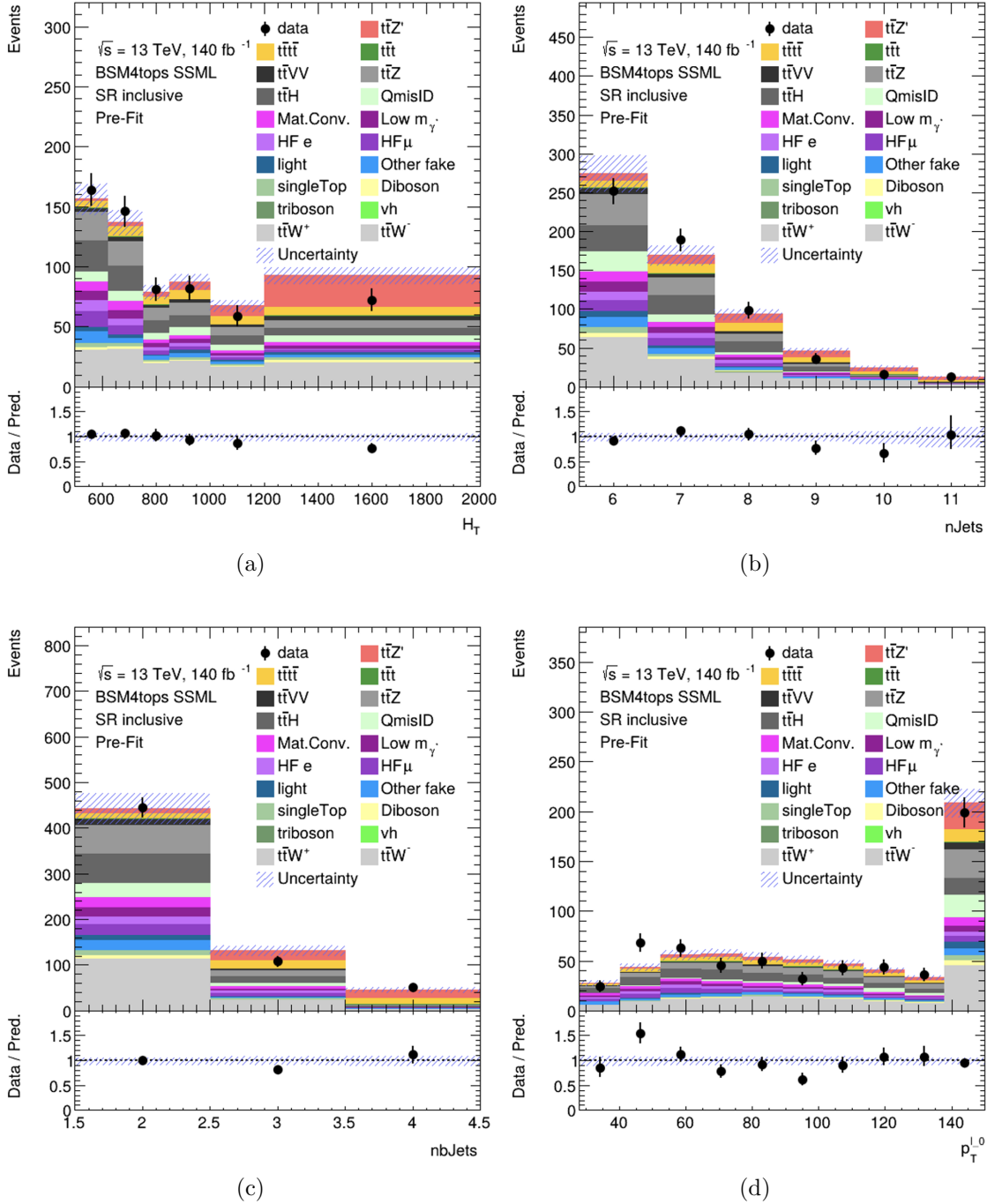


Figure 6.2: Pre-fit kinematic distributions and event compositions in the inclusive SR for (a)  $H_T$  i.e. scalar sum of  $p_T$  of all objects in the event, (b) jet multiplicity, (c)  $b$ -jet multiplicity, (d) leading lepton  $p_T$ . The shaded band represents the uncertainty in the total distribution. The first and last bins of each distribution contain underflow and overflow events respectively.

1383 to determine the  $t\bar{t}W$  normalization within an SR-related phase space. Orthogonality with  
 1384 SR is ensured by requiring  $H_T < 500$  GeV or  $N_{\text{jets}} < 6$  when  $N_b = 2$ , and  $H_T < 500$   
 1385 GeV when  $N_b \geq 3$ . Events in CR 1b( $\pm$ ) are required to have  $H_T > 500$  GeV and at least  
 1386 four jets to encompass events with high  $N_{\text{jets}}$ , which can be used to determine the  $t\bar{t}W$  jet  
 1387 multiplicity spectrum for fitting  $a_{0,1}$ . The selection criteria also include exactly one  $b$ -tagged  
 1388 jet to maintain orthogonality with the SR.

### 1389 **Fake/non-prompt background CRs**

1390 Selection for fake/non-prompt CRs are determined using the `DFCommonAddAmbiguity`  
 1391 (`DFCAA`) variable for reconstructed leptons.

Table 6.3: List of possible assigned values for DFCAA.

| DFCAA | Description                          |
|-------|--------------------------------------|
| -1    | No 2nd track found                   |
| 0     | 2nd track found, no conversion found |
| 1     | Virtual photon conversion candidate  |
| 2     | Material conversion candidate        |

1392 Four CRs are defined for the three main types of fake/non-prompt backgrounds in the  
 1393 analysis - virtual photon ( $\gamma^*$ ) conversion, photon conversion in detector material (Mat.  
 1394 Conv.) and heavy flavor decays (HF). The full selection criteria for fake/non-prompt CRs  
 1395 are shown in Table 6.1.

1396 • **Low  $m_\gamma^*$ :** events with an  $e^+e^-$  pair produced from a virtual photon.

1397 Events are selected if there are two same-sign leptons with at least one electron recon-  
 1398 structed as an internal conversion candidate, and neither reconstructed as a material  
 1399 conversion candidate.

- 1400 • **Mat. Conv.**: events with an electron originating from photon conversion within the  
1401 detector material.

1402 Events are selected if there are two same-sign leptons with at least one electron recon-  
1403 structed as a material conversion candidate.

- 1404 • **HF  $e(\mu)$** : events with a reconstructed non-prompt lepton from semi-leptonic decays of  
1405  $b$ - and  $c$ -hadrons (heavy flavor decays).

1406 Events are selected if there are three leptons with at least two electrons (muons), with  
1407 no lepton reconstructed as a conversion candidate.

## 1408 6.3 Background estimation

1409 Background in this analysis consist of SM processes that can result in a signal signature  
1410 similar to a  $t\bar{t}t\bar{t}$  SSML final state and can be divided into two types, reducible and irreducible.  
1411 Reducible background consists of processes that do not result in a SSML final state physically,  
1412 but are reconstructed as such due to detector and reconstruction effects. The main types  
1413 of reducible background considered are charge misidentification (QmisID) and fake/non-  
1414 prompt leptons. Fake/non-prompt lepton backgrounds contaminate the SR when a non-  
1415 prompt lepton is reconstructed as a prompt lepton in a  $t\bar{t}$ -associated process, leading to  
1416 a similar final state to that of SSML  $t\bar{t}t\bar{t}$ . These backgrounds are estimated using the  
1417 template fitting method described in subsection 6.3.1, where MC simulations are normalized  
1418 to their theoretical SM cross section via floating normalization factors (NFs) constrained by  
1419 the corresponding CRs. Lepton charge misidentification background contaminates the SR  
1420 similarly when one of the two leptons in a  $t\bar{t}$ -associated process with two opposite-sign leptons  
1421 is misidentified, producing a SS2L  $t\bar{t}t\bar{t}$  final state. Charge misidentification background is

<sup>1422</sup> estimated using a data-driven method described in section 6.3.2 along with ECIDS described

<sup>1423</sup> in section 4.3.1.

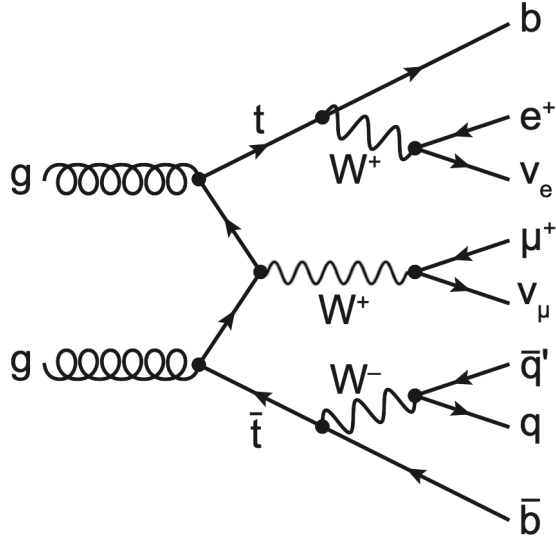


Figure 6.3: Feynman diagram for one possible  $t\bar{t}W$  decay process with similar SS2L lepton signature to the  $t\bar{t}Z'$  signal. Usually only two  $b$ -jets are present due to CKM suppression of  $b$ -quark production from  $W$ -boson decays; this is enough to allow  $t\bar{t}W$  decays to enter and contaminate the SR.

<sup>1424</sup> Irreducible background consists of SM processes that result in SSML final states with all

<sup>1425</sup> leptons being prompt. The dominating background in the SR are SM  $t\bar{t}t\bar{t}$ ,  $t\bar{t}W$ ,  $t\bar{t}Z$ , and

<sup>1426</sup>  $t\bar{t}H$  production with smaller contributions from  $VV$ ,  $VVV$ ,  $VH$  and rarer processes like

<sup>1427</sup>  $t\bar{t}VV$ ,  $tWZ$ ,  $tZq$  and  $t\bar{t}t$ . Most irreducible backgrounds are estimated using template fitting

<sup>1428</sup> method, with the exception of  $t\bar{t}W + \text{jets}$  background. The  $t\bar{t}W + \text{jets}$  background is instead

<sup>1429</sup> given four dedicated CRs, and estimated using a data-driven method with a fitted function

<sup>1430</sup> parameterized in  $N_{\text{jets}}$ . All CRs and SR are included in the final profile LH fit to data.

1431 **6.3.1 Template fitting for fake/non-prompt estimation**

1432 The template fitting method is a semi-data-driven approach [151] that estimates fake/non-  
1433 prompt background distributions by fitting the MC kinematic profile of background processes  
1434 arising from fake/non-prompt leptons to data. The four main sources of fake/non-prompt  
1435 leptons are generated from  $t\bar{t}$  + jets samples and are constrained by four CRs enriched with  
1436 the corresponding backgrounds. Each of the aforementioned background is assigned a free-  
1437 floating NF resulting in  $NF_{HF\ e}$ ,  $NF_{HF\ \mu}$ ,  $NF_{Mat.\ Conv.}$  and  $NF_{Low\ m_{\gamma^*}}$ . The NFs are fitted  
1438 simultaneously with the signal within their constraining CRs.

1439 **6.3.2 Charge misidentification data-driven estimation**

1440 The  $ee$  and  $e\mu$  channels in the SS2L  $t\bar{t}t\bar{t}$  region are contaminated with opposite-sign  
1441 (OS) dilepton  $t\bar{t}$ -associated events where one electron has its charge misidentified. Charge  
1442 misidentification (QmisID) largely affects electrons due to muons' precise curvature informa-  
1443 tion using ID and MS measurements and low bremsstrahlung rate. The charge flip rates are  
1444 significant at higher  $p_T$  and varies with  $|\eta|$  which is proportional to the amount of detector  
1445 material the electron interacted with.

1446 The charge flip probability  $\epsilon$  is estimated in this analysis with a data-driven method  
1447 [153] using a sample of  $Z \rightarrow e^+e^-$  events with additional constraints on the invariant mass  
1448  $m_{ee}$  to be within 10 GeV of the  $Z$ -boson mass. The  $Z$ -boson mass window is defined to  
1449 be within  $4\sigma$  to include most events within the peak, and is determined by fitting the  $m_{ee}$   
1450 spectrum of the two leading electrons to a Breit-Wigner function, resulting in a range of  
1451  $[65.57, 113.49]$  for SS events and  $[71.81, 109.89]$  for OS events. Background contamination  
1452 near the peak is assumed to be uniform and subtracted using a sideband method. Since the

1453  $Z$ -boson decay products consist of a pair of opposite-sign electrons, all same-sign electron

1454 pairs are considered affected by charge misidentification.

1455 Let  $N_{ij}^{\text{SS}}$  be the number of events with SS electrons with the leading electron in the  
1456  $i^{\text{th}}$  2D bin in  $(p_T, |\eta|)$  and the sub-leading electron in the  $j^{\text{th}}$  bin. Assuming the QmisID  
1457 probabilities of electrons in an event are uncorrelated,  $N_{ij}^{\text{SS}}$  can be estimated as

$$N_{ij}^{\text{SS}} = N_{ij}^{\text{tot}} [\epsilon_i(1 - \epsilon_j) + \epsilon_j(1 - \epsilon_i)], \quad (6.1)$$

1458 where  $N_{ij}^{\text{tot}}$  is the total number of events in the  $i^{\text{th}}$  and  $j^{\text{th}}$  bin regardless of charge, and

1459  $\epsilon_{i(j)}$  is the QmisID rate in the  $i^{\text{th}}(j^{\text{th}})$  bin. Assuming  $N_{ij}^{\text{SS}}$  follows a Poisson distribution  
1460 around the expectation value  $\bar{N}_{ij}^{\text{SS}}$ , the  $(i, n)^{\text{th}}$  rate  $\epsilon$  can be estimated by minimizing a  
1461 negative-LLH function parameterized in  $p_T$  and  $|\eta|$ ,

$$\begin{aligned} -\ln(\mathcal{L}(\epsilon | N_{\text{SS}})) &= -\ln \prod_{ij} \frac{(N_{ij}^{\text{tot}})^{N_{ij}^{\text{SS}}} \cdot e^{N_{ij}^{\text{tot}}}}{N_{ij}^{\text{SS}}!} \\ &= -\sum_{ij} \left[ N_{ij}^{\text{SS}} \ln(N_{ij}^{\text{tot}}(\epsilon_i(1 - \epsilon_j) + \epsilon_j(1 - \epsilon_i))) - N_{ij}^{\text{tot}}(\epsilon_i(1 - \epsilon_j) + \epsilon_j(1 - \epsilon_i)) \right]. \end{aligned} \quad (6.2)$$

1462 The QmisID rates are then calculated separately for SR and CRs with different electron

1463 definitions i.e. CR Low  $m_{\gamma^*}$ , CR Mat. Conv., CR  $t\bar{t}W^\pm$ , using events from data after

1464 applying region-specific lepton selections and ECIDS. The events are required to satisfy

1465 SS2L kinematic selections but contains OS electrons. The following weight is applied to OS

<sup>1466</sup> events to correct for misidentified SS events within the region,

$$w = \frac{\epsilon_i + \epsilon_j - 2\epsilon_i\epsilon_j}{1 - \epsilon_i - \epsilon_j + 2\epsilon_i\epsilon_j}. \quad (6.3)$$

<sup>1467</sup> The QmisID rates calculated for SR and CR  $t\bar{t}W$  are shown in Figure 6.4

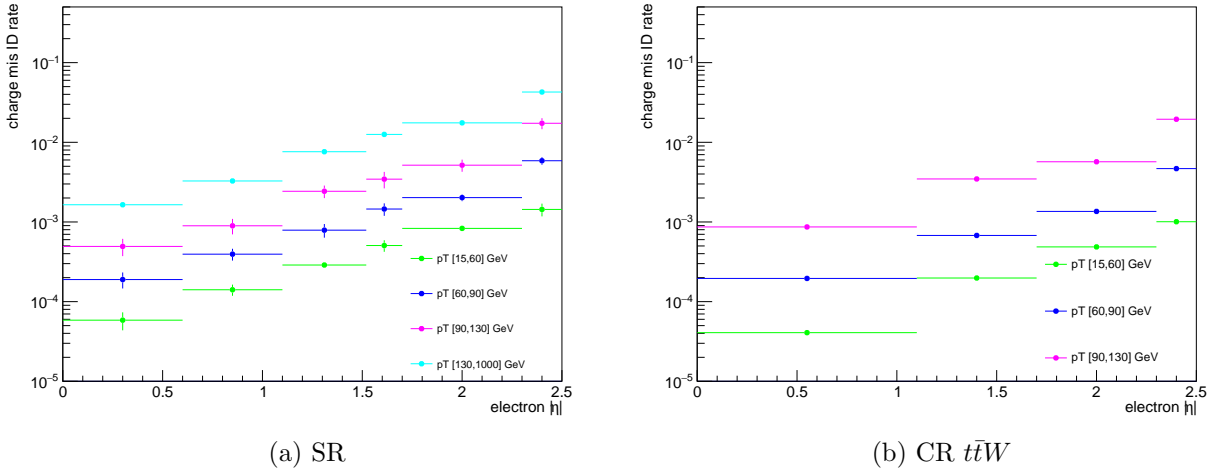


Figure 6.4: Charge flip rate calculated for SR and CR  $t\bar{t}W$  in bins of  $|\eta|$  and  $p_T$ .

<sup>1468</sup> The QmisID rates obtained after applying  $w$  contain a dependency on jet multiplicity  
<sup>1469</sup> and are underestimated at higher  $N_{\text{jets}}$ . This dependency affect the SR which require events  
<sup>1470</sup> with  $\geq 6$  jets, and is corrected by applying a correction factor  $SF_{i,n} = \epsilon_{i,n}/\epsilon_{i,N}$  where  $N$  is  
<sup>1471</sup> the inclusive bin containing all  $N_{\text{jets}}$  and  $\epsilon_{i,n}$  is the QmisID rate obtained from Equation 6.2  
<sup>1472</sup> in the  $(i, n)^{\text{th}}$  2D bin in  $(p_T, N_{\text{jets}})$ . Jet multiplicity and consequently the obtained SFs are  
<sup>1473</sup> assumed to be independent of  $|\eta|$ .

### <sup>1474</sup> 6.3.3 $t\bar{t}W$ background data-driven estimation

<sup>1475</sup> Previously, the  $t\bar{t}W$  background in  $t\bar{t}t\bar{t}$  final state analyses was handled by assigning large  
<sup>1476</sup> ad-hoc systematic uncertainties to  $t\bar{t}W$  events with 7 or more jets [47]. A semi-data-driven

<sub>1477</sub> method [154] was shown to be effective in the SM  $t\bar{t}t\bar{t}$  observation analysis [44] by improving  
<sub>1478</sub>  $t\bar{t}W$  modeling, especially in the showering step and switching  $t\bar{t}W$  systematic uncertainties  
<sub>1479</sub> from predominantly modeling to statistical.

<sub>1480</sub> The data-driven method applies correction factors obtained from a fitted function pa-  
<sub>1481</sub> rameterized in  $N_{\text{jets}}$  to  $t\bar{t}W$  MC kinematic distributions. The QCD scaling patterns [155] can  
<sub>1482</sub> be represented by ratio of successive exclusive jet cross-sections

$$R_{(n+1)/n} = \frac{\sigma_{n+1}}{\sigma_n} = e^{-b} + \frac{\bar{n}}{n+1} = a_0 + \frac{a_1}{1+(j-4)}, \quad (6.4)$$

<sub>1483</sub> where  $a_{0(1)}$  and  $b$  are constants,  $n$  is the number of jets in addition to the hard process,  $j$   
<sub>1484</sub> is the inclusive number of jets, and  $\bar{n}$  is the expectation value for the Poisson distribution  
<sub>1485</sub> of exclusive jet cross-section at jet multiplicity  $n$ . The  $t\bar{t}W$  ME for SS2L events gives 4 jets  
<sub>1486</sub> in the hard process, so  $n$  is defined starting from the 5<sup>th</sup> jets and the inclusive number of  
<sub>1487</sub> jets  $j = n + 4$ . The two terms in Equation 6.4 correspond to staircase and Poisson scaling  
<sub>1488</sub> in cross section between successive jet multiplicities and are sensitive to high and low jet  
<sub>1489</sub> multiplicity events respectively [155]. The scaling pattern can then be reparameterized in  
<sub>1490</sub>  $a_0$  and  $a_1$  to obtain the  $t\bar{t}W$  yield at  $j' \equiv j + 1$  jets

$$\text{Yield}_{t\bar{t}W(j')} = \text{Yield}_{t\bar{t}W(N_{\text{jets}}=4)} \times \prod_{j=4}^{j'-1} \left( a_0 + \frac{a_1}{1+(j-4)} \right) \quad (6.5)$$

<sub>1491</sub> with  $j \geq 4$ . The  $t\bar{t}W$  yield in the 4-jet bin can be represented by a NF applied to  $t\bar{t}W$  MC  
<sub>1492</sub> simulation

$$\text{Yield}_{t\bar{t}W(N_{\text{jets}}=4)} = \text{NF}_{t\bar{t}W(N_{\text{jets}}=4)} \times \text{MC}_{t\bar{t}W(N_{\text{jets}}=4)}. \quad (6.6)$$

<sub>1493</sub> To account for the asymmetry in  $t\bar{t}W^+$  and  $t\bar{t}W^-$  cross-sections,  $\text{NF}_{t\bar{t}W(N_{\text{jets}}=4)}$  is further

1494 split into  $\text{NF}_{t\bar{t}W^\pm(N_{\text{jets}}=4)}$  assuming the scaling is the same for both processes. Both NFs

1495 are left free-floating to constrain  $t\bar{t}W$  yields in the 4-jet bin within CR 1b(+) and CR 1b(-).

1496 The final  $N_{\text{jets}}$ -parameterized function can then be represented by  $\text{NF}_{t\bar{t}W(j')}$  as

$$\text{NF}_{t\bar{t}W(j')} = \left( \text{NF}_{t\bar{t}W^+(N_{\text{jets}}=4)} + \text{NF}_{t\bar{t}W^-(N_{\text{jets}}=4)} \right) \times \prod_{j=4}^{j'-1} \left( a_0 + \frac{a_1}{1+(j-4)} \right). \quad (6.7)$$

1497 The normalization is calculated and applied separately for each sub-sample of  $t\bar{t}W^+$  and

1498  $t\bar{t}W^-$  in a  $N_{\text{jets}}$  bin for  $4 \leq N_{\text{jets}} < 10$ . Due to small contributions in the CRs, events

1499 with  $N_{\text{jets}} < 4$  and  $N_{\text{jets}} \geq 10$  are not normalized with this scheme. Instead,  $N_{\text{jets}} < 4$

1500 events are fitted by propagating the normalization in the 4-jet bin without additional shape

1501 correction. The correction factor for  $t\bar{t}W$  events with  $N_{\text{jets}} \geq 10$  is obtained by summing

1502 up the overflow from  $N_{\text{jets}} = 10$  to  $N_{\text{jets}} = 12$ , described as  $\sum_{j'=10}^{12} \prod_{j=4}^{j'-1} \left( a_0 + \frac{a_1}{1+(j-4)} \right)$ .

1503 Events with  $N_{\text{jets}} \geq 13$  are negligible and are not included in the sum.

1504 The four regions, CR  $t\bar{t}W^\pm$  and CR 1b( $\pm$ ), are constructed to fit  $\text{NF}_{t\bar{t}W^\pm(N_{\text{jets}}=4)}$  and

1505 the scaling parameters  $a_{0(1)}$ , as well as validating the parameterization. Assuming the  $N_{\text{jets}}$

1506 distribution of  $t\bar{t}W$  is similar across bins of  $N_b$ -jets, a fitted  $N_{\text{jets}}$  distribution in CR 1b( $\pm$ )

1507 can be used to describe the  $t\bar{t}W$  parameterization at higher  $N_{\text{jets}}$ .

# 1508 Chapter 7. Systematic Uncertainties

1509 Physics analysis inherently incurs uncertainties in the form of statistical and systematic  
1510 uncertainties, depending on the source. Statistical uncertainties occur in this analysis from  
1511 sample size of collected data and simulated MC samples, and from the maximizing of the  
1512 LH function. Systematic uncertainties depend on identifiable sources in the analysis i.e.  
1513 from detector and reconstruction effects (experimental uncertainties) or theoretical modeling  
1514 (theoretical uncertainties). Systematic uncertainties are represented as nuisance parameters  
1515 ( $NP_x$ ) in the profile LH fit. During the fit, systematic uncertainties with negligible impact  
1516 on the final results can be pruned to simplify the statistical model and reduce computational  
1517 complexity. This section outlines all uncertainties considered in this analysis.

## 1518 7.1 Experimental uncertainties

### 1519 7.1.1 Luminosity & pile-up reweighting

1520 The uncertainty on the integrated luminosity of the 2015-2018 Run 2 data set is 0.83%  
1521 [89], obtained by the LUCID-2 detector [156] for the primary luminosity measurements and  
1522 complemented by the ID and calorimeters. Pile-up was modeled in MC and calibrated  
1523 to data through pile-up reweighting, resulting in a set of calibration SFs and associated  
1524 uncertainties.

### 1525 7.1.2 Leptons

1526 In general, calibrating MC simulations to match performance in data incurs uncertainties  
1527 associated obtaining the MC-to-data calibration SFs, which are in turn propagated to observ-

ables in the analysis. The data-to-MC calibration of trigger, reconstruction, identification and isolation efficiencies for electrons and muons incur associated uncertainties, with separate systematic and statistical components for those related to muons. Similarly, electron energy scale, muon momentum scale and resolution are also subjected to calibration uncertainties estimated by re-simulating the events while varying the energy/momenta scale and resolution. Electron has an additional uncertainty related to ECIDS efficiency. Muon has additional uncertainties for charge-independent and charge-dependent momentum scale, as well as detector-specific track resolution. Systematic uncertainties for electron reconstruction, identification, isolation, ECIDS efficiencies and muon ID/MS energy resolution were not ready for the sample version used in this analysis, and are therefore not included.

### 7.1.3 Jets

Experimental uncertainties for jets are dominated by flavor tagging-related uncertainties, with subleading contributions from uncertainties related to JES [112], JER [111] and JVT [157] calibrations.

#### Jet energy scale

Uncertainties associated with JES are determined using data from LHC collisions along with MC simulated samples [112], decomposed into uncorrelated components:

- **Effective NPs:** 15 total  $p_T$ -dependent uncertainty components measured in situ, grouped based on their origin (2 detector-related, 4 modeling-related, 3 mixed, 6 statistical-related)
- $\eta$  **intercalibration:** 6 total components (1 modeling-related, 4 non-closure and 1

1549 statistical-related) associated with the correction of the forward jets' ( $0.8 \leq |\eta| < 4.5$ )  
1550 energy scale to that of the central jets ( $|\eta| < 0.8$ ).

1551 • **Flavor composition & response:** 2 components for relative quark-gluon flavor com-  
1552 positions in background and signal samples, and 2 components for responses to gluon-  
1553 initiated versus quark-initiated jets.

1554 • **Pile-up subtraction:** 4 components, 2 for  $\mu$  (`OffsetMu`) and  $N_{\text{PV}}$  (`OffsetNPV`) mod-  
1555 eling, 1 for residual  $p_{\text{T}}$ -dependency (`PtTerm`) and 1 for topology dependence on the  
1556 per-event  $p_{\text{T}}$  density modeling (`RhoTopology`).

1557 • **Punch-through effect treatment:** 2 terms for GSC punch-through jet response  
1558 deviation between data and MC, one for each detector response simulation method  
1559 (AF3 and FS).

1560 • **Non-closure:** 1 term applied to AF3 sample to account for the difference between  
1561 AF3 and FS simulation.

1562 • **High- $p_{\text{T}}$  single-particle response:** 1 term for the response to high- $p_{\text{T}}$  jets from  
1563 single-particle and test-beam measurements.

1564 •  **$b$ -jets response:** 1 term for the difference between  $b$ -jets and light-jets response.

## 1565 Jet energy resolution

1566 Measurements of JER were performed in bins of  $p_{\text{T}}$  and  $\eta$ , separately in data using in-  
1567 situ techniques and in MC simulation using dijet events [111]. This analysis uses the full  
1568 correlation JER uncertainty scheme provided for Run 2 analysis with 14 total components:

<sub>1569</sub> 12 for effective NPs and 2 for difference between data and MC, separately for AF3 and FS  
<sub>1570</sub> [111].

<sub>1571</sub> **Jet vertex tagging**

<sub>1572</sub> The uncertainty associated with JVT is obtained by varying the JVT efficiency SFs  
<sub>1573</sub> within their uncertainty range [157]. This uncertainty accounts for remaining contamination  
<sub>1574</sub> from pile-up jets after applying pile-up suppression and MC generator choice.

<sub>1575</sub> **Flavor tagging**

<sub>1576</sub> Calibration SFs for  $b$ -tagging efficiencies and  $c$ -/light-jets mistagging rates are derived as  
<sub>1577</sub> a function of  $p_T$  for  $b$ -,  $c$ -, light-jets and PCBT score. The full set of flavor tagging-related  
<sub>1578</sub> uncertainties was reduced in dimensions by diagonalizing the uncertainty covariance matrix  
<sub>1579</sub> via eigendecomposition [115], resulting in a compact set of orthogonal NPs for this analysis:  
<sub>1580</sub> 85 for  $b$ -jets, 56 for  $c$ -jets and 42 for light-jets.

<sub>1581</sub> **7.1.4 Missing transverse energy**

<sub>1582</sub> Uncertainties on  $E_T^{\text{miss}}$  arise from possible mis-calibration of the soft-track component  
<sub>1583</sub> and are estimated using data-to-MC comparison of the  $p_T$  scale and resolution between  
<sub>1584</sub> the hard and soft  $E_T^{\text{miss}}$  components [119]. These uncertainties are represented by three  
<sub>1585</sub> independent terms: 1 for scale uncertainty and 2 for resolution uncertainty of the parallel  
<sub>1586</sub> and perpendicular components.

<sub>1587</sub> **7.2 Modeling uncertainties**

<sub>1588</sub> **7.2.1 Signal and irreducible background uncertainties**

<sub>1589</sub> The signal and background samples used are modeled using MC simulation. Most uncer-  
<sub>1590</sub> tainties on simulation parameters (e.g. generator choice, PS model) are estimated by varying  
<sub>1591</sub> the relevant parameters and comparing them with the nominal sample. Uncertainties in-  
<sub>1592</sub> volving PDF in particular for most processes in the analysis are set to a flat 1% uncertainty.  
<sub>1593</sub> Cross-section uncertainties were considered for all irreducible background except  $t\bar{t}W$ , which  
<sub>1594</sub> is normalized in dedicated CRs following section 6.3.3. Extra uncertainties for the produc-  
<sub>1595</sub> tion of four or more  $b$ -jets (additional  $b$ -jets) in association with  $t\bar{t}X$  and HF jets were also  
<sub>1596</sub> considered due to a lack of theoretical predictions or dedicated measurements, rendering  
<sub>1597</sub> MC modeling challenging. Uncertainties from missing higher-order QCD corrections in MC  
<sub>1598</sub> simulation are estimated by varying the renormalization scale  $\mu_R$  and factorization scale  $\mu_F$   
<sub>1599</sub> within seven different combinations

$$(\mu_R, \mu_F) = \{(0.5, 0.5), (0.5, 1), (1, 0.5), (1, 1), (1, 2), (2, 1), (2, 2)\}.$$

<sub>1600</sub> Process-specific uncertainty treatments are detailed below.

<sub>1601</sub> **SM  $t\bar{t}t\bar{t}$  background**

<sub>1602</sub> The generator uncertainty for the SM  $t\bar{t}t\bar{t}$  background was evaluated between a nominal  
<sub>1603</sub> sample of MADGRAPH5\_AMC@NLO and SHERPA. The parton shower uncertainty was  
<sub>1604</sub> evaluated between PYTHIA8 and HERWIG. The cross-section uncertainty was estimated to

1605 be 20% computed from a prediction at NLO in QCD+EW [128].

## 1606 $t\bar{t}t$ background

1607 The cross-section uncertainty for  $t\bar{t}t$  was estimated to be 30% computed from a prediction  
1608 at NLO in QCD+EW [128]. Events with additional  $b$ -jets also incur a 50% uncertainty.

## 1609 $t\bar{t}W$ , $t\bar{t}Z$ , $t\bar{t}H$ backgrounds

1610 For  $t\bar{t}W$ ,  $t\bar{t}Z$  and  $t\bar{t}H$  backgrounds, an uncertainty of 50% is assigned to events with one  
1611 additional truth  $b$ -jets that did not originate from a top quark decay, and an added 50%  
1612 uncertainty is assigned to events with two or more [158] additional  $b$ -jets. The generator  
1613 uncertainty was estimated for  $t\bar{t}Z$  using a MADGRAPH5\_AMC@NLO nominal sample and  
1614 a SHERPA sample, and for  $t\bar{t}H$  using POWHEGBOX samples interfaced with PYTHIA8 (nom-  
1615 inal) and HERWIG7. Cross-section uncertainties of 12% and 10% were applied to  $t\bar{t}Z$  and  
1616  $t\bar{t}H$  respectively [159]. No  $t\bar{t}W$  cross-section or PDF uncertainty was considered since the  
1617 normalizations and jet multiplicity spectrum for  $t\bar{t}W$  are estimated using the data-driven  
1618 method described in section 6.3.3.

## 1619 Other backgrounds

1620 Other backgrounds include processes with small overall contribution in the SR. The  
1621 cross-section uncertainty for  $tZ$  and  $tWH$  is considered to be 30% [160, 161]. A conservative  
1622 cross-section uncertainty of 50% is applied to  $t\bar{t}VV$ ,  $VVV$  and  $VH$ . For  $VV$ , the cross-  
1623 section uncertainty is dependent on jet multiplicity and is considered to be 20%/50%/60%  
1624 for events with  $\leq 3/4 \geq 5$  jets [162]. For  $VV$ ,  $t\bar{t}VV$ ,  $VVV$  and  $VH$  events with additional  
1625 truth  $b$ -jets, an uncertainty of 50% is applied.

## 1626 7.2.2 Reducible background uncertainties

1627 Reducible backgrounds consist of  $t\bar{t}/V + \text{HF}$  jets and single top events. Reducible back-  
1628 ground has small contamination within the SR, thus uncertainties related to reducible back-  
1629 ground have minor impact. Treatment for reducible background in this analysis largely  
1630 follows Ref. [44], except for QmisID.

## 1631 Charge misidentification

1632 Uncertainties on the QmisID background originate from the charge flip rates obtained  
1633 using the data-driven method described in section 6.3.2. Four sources of uncertainty were  
1634 considered: statistical uncertainty from the maximum LLH estimation using Equation 6.2;  
1635 uncertainty from choice of the  $Z$ -mass window and sidebands; non-closure uncertainty de-  
1636 fined as the relative difference between the number of SS and OS events; and statistical  
1637 uncertainty from the  $N_{\text{jets}}$  dependency correction SFs. The combined uncertainties from  
1638 all four sources are calculated separately for each region involved in section 6.3.2, and are  
1639 treated as correlated across all regions. Figure 7.1 shows the uncertainty calculated for SR.

## 1640 Internal (low $\gamma^*$ ) and material conversion

1641 The normalization for internal and material conversion backgrounds are free parameters  
1642 in the fit, as a result the only uncertainties evaluated are from the shape of the distributions  
1643 used in the template fit method (see section 6.3.1). The uncertainties on internal (material)  
1644 conversion are estimated based on the difference between data and MC prediction in a region  
1645 enriched in  $Z + \gamma \rightarrow \mu^+\mu^- + e^+e^-$  events.

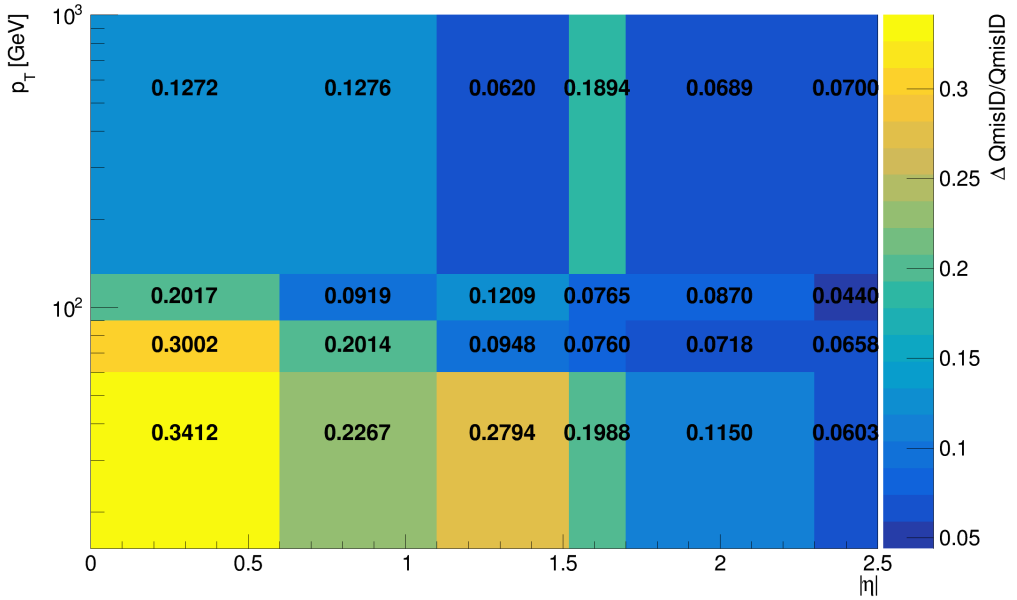


Figure 7.1: Combined QmisID uncertainty rate for SR in bins of  $|\eta|$  and  $p_T$ .

### <sup>1646</sup> Heavy-flavor non-prompt lepton

<sup>1647</sup> Similar to the conversion backgrounds, the uncertainties on non-prompt HF decays come  
<sup>1648</sup> from the shape of the distributions, and are estimated by comparing data and MC prediction  
<sup>1649</sup> between all regions in the analysis on a per bin basis. The events used are required to  
<sup>1650</sup> contain at least one *Loose* reconstructed lepton used in the region selection criteria detailed  
<sup>1651</sup> in Table 6.1 to maintain orthogonality with the SR.

### <sup>1652</sup> Light-flavor decays and other fake/non-prompt backgrounds

<sup>1653</sup> A conservative normalization uncertainty of 100% is assigned for light-flavor non-prompt  
<sup>1654</sup> lepton background [151], and an ad-hoc normalization uncertainty of 30% is applied to all  
<sup>1655</sup> other fake and non-prompt backgrounds. The shape uncertainties for these backgrounds are  
<sup>1656</sup> negligible.

1657 **Chapter 8. Results**

1658 **8.1 Statistical interpretation**

1659 This section provides an overview of the statistical methods needed to interpret the  
1660 collected and simulated data to estimate unknown physics parameters and determine com-  
1661 patibility between data and the analysis hypothesis. For the BSM resonance search, the null  
1662 hypothesis  $H_0$  assumes only SM background contributions and none from any new BSM  
1663 resonance in the data.

1664 **8.1.1 Profile likelihood fit**

1665 Given a set of observed data points  $\mathbf{x} = [x_1, x_2, \dots]$  and unknown parameters  $\boldsymbol{\theta} =$   
1666  $[\theta_1, \theta_2, \dots, \theta_n]$ , the maximum likelihood method aims to find an estimate  $\hat{\boldsymbol{\theta}}$  that maximizes  
1667 the joint probability function  $f(\mathbf{x}, \boldsymbol{\theta})$ , or in other words the set of parameters that gives the  
1668 highest probability of observing the collected data points for a particular model. The func-  
1669 tion to be maximized for this purpose is the log-likelihood (LLH) function  $\ln \mathcal{L}(\mathbf{x}, \boldsymbol{\theta})$  where  
1670  $\mathcal{L}(\mathbf{x}, \boldsymbol{\theta}) \equiv \prod_i f(x_i, \boldsymbol{\theta})$  is defined as the likelihood (LH) function. The LLH is maximized  
1671 when  $\partial/\partial\theta_i (\ln \mathcal{L}) = 0$  for each parameter  $\theta_i$ .

1672 For an usual binned physics analysis, the above variables for the LH function  $\mathcal{L}$  can  
1673 be expressed as nuisance parameters (NP)  $\boldsymbol{\theta}$  and number of events for a model  $N_i(\mu)$  for  
1674 the  $i^{\text{th}}$  bin, where  $\mu$  is the targeted parameter of interest (POI). In this analysis,  $N_i$  is  
1675 assumed to follow a Poisson distribution and depends on the following quantities: the signal  
1676 strength  $\mu$  defined as the ratio of observed to expected cross sections  $\sigma_{\text{obs}}/\sigma_{\text{exp}}$ ; nuisance  
1677 parameters  $\boldsymbol{\theta}$  which represents the effects of systematic uncertainties, implemented in the

1678 LH function as Gaussian constraints; and normalization factors (NFs)  $\boldsymbol{\lambda}$  that control the  
 1679 normalization of background components that do not have a well-known cross section. The  
 1680 Poisson probability of observing exactly  $N_i$  events for an expected number of event  $n_i$  is

$$\mathcal{P}(N_i|n_i(\mu, \boldsymbol{\lambda})) = \frac{n_i^{N_i} e^{-n_i}}{N_i!}. \quad (8.1)$$

1681 The expected Poisson event number in a bin  $i$  can be parameterized as

$$n_i = \mu s_i(\boldsymbol{\theta}) + \sum_j \lambda_j b_{ij}(\boldsymbol{\theta}), \quad (8.2)$$

1682 where  $s_i$  is the number of signal events in bin  $i$  of every region, and  $b_{ij}$  is the number of  
 1683 events for a certain background source index  $j$  in bin  $i$ . The LH function in this analysis  
 1684 can be written as

$$\mathcal{L}(\mathbf{N}|\mu, \boldsymbol{\theta}, \boldsymbol{\lambda}) = \left( \prod_i \mathcal{P}(N_i|n_i) \right) \cdot \prod_k \mathcal{G}(\theta_k), \quad (8.3)$$

1685 where  $\mathcal{G}(\theta_k)$  is the Gaussian constraint for a NP  $k$ . The signal significance  $\mu$  and NFs  $\boldsymbol{\lambda}$  are  
 1686 left unconstrained and are fitted simultaneously in the profile LH fit. Define the profile LH  
 1687 ratio [163] as

$$\lambda(\mu) = \frac{\mathcal{L}(\mu, \hat{\boldsymbol{\theta}}_\mu, \hat{\boldsymbol{\lambda}}_\mu)}{\mathcal{L}(\hat{\mu}, \hat{\boldsymbol{\theta}}, \hat{\boldsymbol{\lambda}})}, \quad (8.4)$$

1688 where  $\hat{\mu}$ ,  $\hat{\boldsymbol{\theta}}$  and  $\hat{\boldsymbol{\lambda}}$  are parameter values that optimally maximizes the LH function, and  $\hat{\boldsymbol{\theta}}_\mu$ ,  
 1689  $\hat{\boldsymbol{\lambda}}_\mu$  are NP and NF values respectively that maximize the LH function for a given signal  
 1690 strength  $\mu$ . Using Neyman-Pearson lemma [164], the optimal test statistic for hypothesis  
 1691 testing is

$$q_\mu \equiv -2 \ln \lambda(\mu), \quad (8.5)$$

1692 where  $q_\mu = 0$  or  $\lambda(\mu) = 1$  corresponds to perfect agreement between the optimal parameter  
 1693  $\hat{\mu}$  obtained from data and the hypothesized value  $\mu$ . From Wilks' theorem [165], the test  
 1694 statistic  $q_\mu$  approaches a  $\chi^2$  distribution and can be evaluated as  $q_\mu = (\mu - \hat{\mu})^2 / \sigma_\mu^2$ .

1695 When evaluating against the background-only hypothesis ( $\mu = 0$ ), it can be assumed  
 1696 that the number of events observed under the signal hypothesis is higher than that of the  
 1697 background-only hypothesis, or  $\mu \geq 0$  according to Equation 8.2. This leads to a corre-  
 1698 sponding lower bound on the test statistic

$$q_0 = \begin{cases} -2 \ln \lambda(0), & \text{if } \hat{\mu} \geq 0, \\ 0, & \text{if } \hat{\mu} < 0. \end{cases} \quad (8.6)$$

### 1699 ***p*-value**

1700 To quantify the incompatibility between the observed data and the background-only hy-  
 1701 pothesis, the *p*-value is defined as  $p = P(q_\mu \geq q_{\mu, \text{obs}} | H_0)$  or in other words, the probability  
 1702 of observing data with a test statistic  $q_\mu$  under the null hypothesis  $H_0$  that is less compat-  
 1703 ible with  $H_0$  than the actual observed data with test statistic  $q_{\mu, \text{obs}}$ . The *p*-value can be  
 1704 expressed in terms of  $q_\mu$  as

$$p_\mu = \int_{q_{\mu, \text{obs}}}^{\infty} f(q_\mu | \mu) dq_\mu, \quad (8.7)$$

1705 where  $f(q_\mu | \mu) dq_\mu$  is the conditional probability density function of  $q_\mu$  given  $\mu$ .

1706 In some cases, it is more convenient to evaluate compatibility using the *Z*-value, defined  
 1707 as the number of standard deviations between the observed data and the mean in a Gaussian

1708 distribution. The  $p$ -value can be converted to  $Z$ -value via the relation

$$Z = \Phi^{-1}(1 - p), \quad (8.8)$$

1709 where  $\Phi$  is the quantile of the standard Gaussian. Rejecting the signal hypothesis usually  
1710 requires a 95% confidence level (CL) which corresponds to a  $p$ -value of 0.05 or a  $Z$ -value of  
1711 1.64, while rejecting the background-only hypothesis generally requires a  $Z$ -value of 5 or a  
1712  $p$ -value of  $2.84 \times 10^{-7}$ .

### 1713 8.1.2 Exclusion limit

1714 If the signal hypothesis is rejected, the exclusion upper limits can still be computed at  
1715 a certain CL (usually 95%) to establish the maximum value of  $\mu$  that is not excluded by  
1716 or in conflict with the observed data. The exclusion limits are calculated based on the CLs  
1717 method [166, 167] under which the test statistic is defined as  $q_\mu = -2 \ln \frac{\mathcal{L}_{s+b}}{\mathcal{L}_b}$  with  $\mathcal{L}_{s+b}$   
1718 being the LH function for the signal and background hypothesis ( $\mu > 0$ ) and  $\mathcal{L}_b$  being the  
1719 LH function for the background-only hypothesis ( $\mu = 0$ ). The  $p$ -value for both hypotheses  
1720 can then be expressed as

$$\begin{aligned} p_{s+b} &= P(q \geq q_{\text{obs}} | s + b) = \int_{q_{\text{obs}}}^{\infty} f(q | s + b) dq \\ p_b &= P(q \geq q_{\text{obs}} | b) = \int_{-\infty}^{q_{\text{obs}}} f(q | b) dq. \end{aligned} \quad (8.9)$$

1721 The signal hypothesis is excluded for a CL  $\alpha$  when the following condition is satisfied

$$\text{CL}_s \equiv \frac{p_{s+b}}{p_b} \geq 1 - \alpha. \quad (8.10)$$

1722 The value of  $\mu$  such that the signal hypothesis leads to  $CL_s = 1 - \alpha = 0.05$  is then the  
 1723 exclusion upper limit at a 95% CL. Exclusion limits are usually reported in terms of expected  
 1724 and observed limits. The expected limits show the exclusion limits obtained under the  
 1725 background-only hypothesis and represent the analysis' sensitivity, while the observed limits  
 1726 represent exclusion limits derived from observed data.

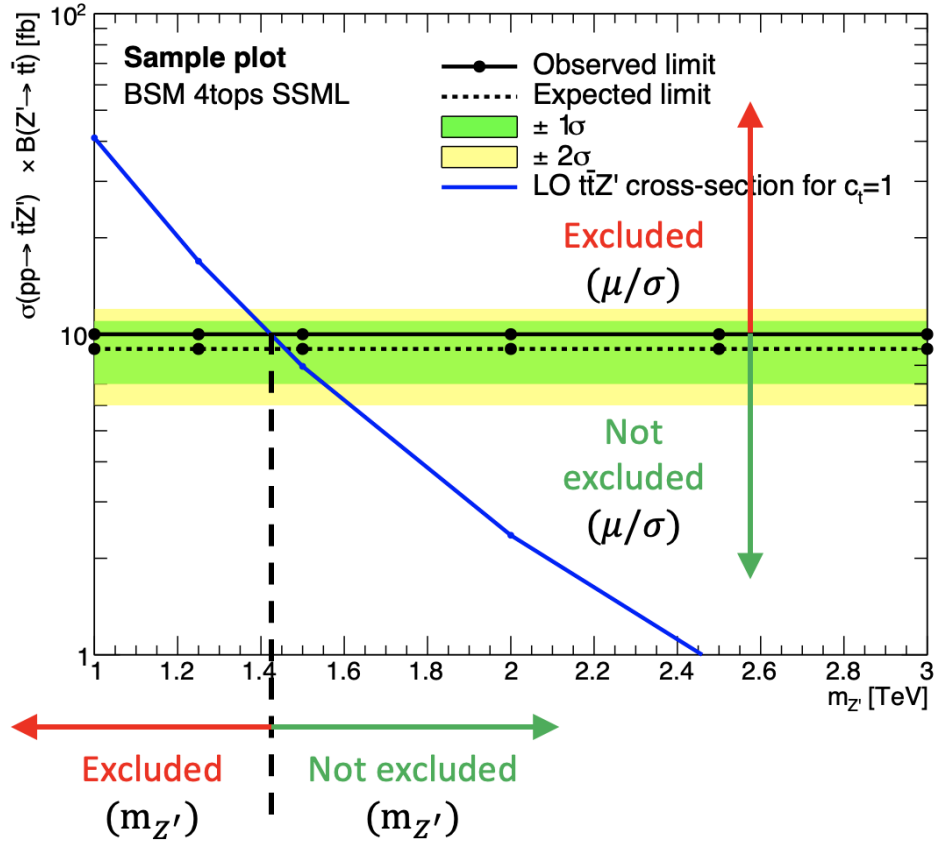


Figure 8.1: Example of an exclusion limit graph. The solid (dotted) line represents the observed (expected) upper limits as a function of the  $Z'$  mass at 95% CL on the cross-section of  $pp \rightarrow t\bar{t}Z'$  production times the  $Z' \rightarrow t\bar{t}$  branching ratio. The solid blue line represents the theoretical signal cross-section with  $c_t = 1$  at LO in QCD [74]. The green and yellow bands represent the 68% ( $\pm 1\sigma$ ) and 95% ( $\pm 2\sigma$ ) confidence intervals for the expected upper limits. Values of  $\mu$  within the region above the observed limit is excluded under the current model. Masses below the  $m_{Z'}$  value at which the observed limit intersect the theoretical cross section are excluded.

1727 In a search for an exotic particle of unknown mass, a lower bound on the mass can

1728 be determined using the theoretical cross section for the particle and the obtained observed  
1729 limits. Figure 8.1 shows a sample exclusion limit graph of the  $t\bar{t}Z'$  cross section as a function  
1730 of the  $Z'$  mass. Values of the signal strength  $\mu$  (and by proxy the cross section  $\sigma$ ) above the  
1731 observed limits are incompatible with the analysis model. Consequently, mass points with a  
1732 smaller observed cross section than the theoretical cross section are excluded from the model;  
1733 the cross section for the particle predicted by the analysis model lies in the exclusion region  
1734 obtained using observed data. Such masses are eliminated as a possibility for the model.

## 1735 8.2 Fit results

1736 The signal strength  $\mu$ , background NFs,  $t\bar{t}W$  scaling factors and uncertainty NPs are  
1737 simultaneously fitted using a binned profile LLH fit under the background-only hypothesis  
1738 to the  $H_T$  distribution in the SR and to corresponding distributions shown in Table 6.1 for  
1739 CRs.

1740 Before fitting to real data (unblinded fit), the fit was first performed in both the SR  
1741 and CRs using Asimov pseudo-datasets, in which the simulated data match exactly to MC  
1742 prediction with nominal  $\mu$  set to 0. This is done for the purpose of optimizing object selection  
1743 criteria and region definition, refining background estimation techniques and testing the  
1744 statistical interpretation model for signal extraction described in section 8.1. The fit is then  
1745 performed with Asimov data in the SR and real data in CRs to validate background modeling,  
1746 estimate sensitivity and assess the influence of statistical effects on fitted parameters. Finally,  
1747 the fully unblinded fit is performed with real data in all regions.

1748 The unblinded fit results are presented below. No significant variation is observed in fit  
1749 output behavior using  $t\bar{t}Z'$  samples of different  $m_{Z'}$ ; results fitted using  $m_{Z'} = 2$  TeV are

1750 shown without substantial loss of generality. The background modeling is evaluated under  
1751 the background-only hypothesis. The fitted background NFs are shown in Table 8.1 and  
1752 are consistent with their nominal values within one standard deviation, or two standard  
1753 deviations in the case of  $\text{NF}_{\text{HF } e}$  and  $\text{NF}_{t\bar{t}W^+(4j)}$ . Figure 8.2 shows good agreement between  
1754 data and post-fit background distributions in non-prompt background CRs and  $t\bar{t}W$  CRs.

1755 The pre-fit and post-fit background yields are shown in Table 8.2. Except for HF  $e$   
1756 background, post-fit yields for various backgrounds e.g.  $t\bar{t}t\bar{t}$ ,  $t\bar{t}H$ , other fake, etc. are  
1757 increased; the pre-fit to post-fit variations are consistent within  $\pm\sigma$ . Data and total post-fit  
1758 yields are also consistent within  $\pm\sigma$ . Post-fit yield for HF  $e$  background is lowered compared  
1759 to pre-fit yield within  $2\sigma$  which can be related to the fitted value of  $\text{NF}_{\text{HF } e}$  in Table 8.1;  
1760 however, this difference in pre- and post-fit yields of HF  $e$  background has negligible impact  
1761 on the  $\mu$  as seen in Table 8.3.

1762 Table 8.3 outlines the impact on the signal strength  $\mu$  of various sources of uncertainty  
1763 grouped by their corresponding category. The background sources of uncertainty with the  
1764 largest impact is  $t\bar{t}t\bar{t}$  modeling, in particular  $t\bar{t}t\bar{t}$  generator choice and cross-section uncer-  
1765 tainties, followed by  $t\bar{t}W$  modeling due to their significant contributions in the SR observed  
1766 in Figure 6.1, especially in the more sensitive regions requiring three or more  $b$ -tagged jets.  
1767 The most significant impact on  $\mu$  within the set of instrumental uncertainties are uncertain-  
1768 ties on jet  $b$ -tagging attributable to the high jet and  $b$ -jet multiplicities in the BSM  $t\bar{t}t\bar{t}$  signal  
1769 signature.

1770 Figure 8.4 shows the post-fit pull from the nominal pre-fit value for each nuisance param-  
1771 eter. Pull for all NPs are consistent within one standard deviation from the nominal pre-fit  
1772 value. Overall, modeling uncertainties suffer from more significant pull compared to experi-  
1773 mental uncertainties. Uncertainty sources with the largest pull are SM  $t\bar{t}t\bar{t}$  cross section and

generator choice, along with  $t\bar{t}Z$  generator choice and diboson cross section. Additionally, no significant constraints are placed on NPs by the fit to data, with the exception of moderate constraint on the diboson cross section.

No significant excess over SM predictions is observed, and the fitted signal strength  $\mu$  is compatible with zero for all  $Z'$  mass points. Figure 8.5 shows the observed and expected upper limits at 95% confidence level on the cross-section of  $pp \rightarrow t\bar{t}Z'$  production times the branching ratio of  $Z' \rightarrow t\bar{t}$  as a function of the  $Z'$  resonance mass. The  $\pm 1\sigma$  and  $\pm 2\sigma$  confidence intervals around the expected exclusion limits are also shown. The observed exclusion limits range from 7.9 fb to 9.44 fb depending on  $m_{Z'}$ . The distribution of limits across  $m_{Z'}$  is flat and show little correlation to signal kinematics and phase space modeling.

The observed limits exclude  $Z'$  masses below  $\approx 15$  TeV.

Table 8.1: Normalization factors for backgrounds with dedicated CRs, obtained from a simultaneous fit in all CRs and SR under the background-only hypothesis. The nominal pre-fit value is 1 for all NFs and 0 for the scaling factors  $a_0$  and  $a_1$ . Uncertainties shown include both statistical and systematic uncertainties.

| Parameter | NF <sub>HF e</sub>     | NF <sub>HF <math>\mu</math></sub> | NF <sub>Mat. Conv.</sub> | NF <sub>Low <math>m_{\gamma^*}</math></sub> | $a_0$                  | $a_1$                  | NF <sub><math>t\bar{t}W+(4j)</math></sub> | NF <sub><math>t\bar{t}W-(4j)</math></sub> |
|-----------|------------------------|-----------------------------------|--------------------------|---|------------------------|------------------------|---|---|
| Fit value | $0.68^{+0.23}_{-0.22}$ | $0.97^{+0.17}_{-0.16}$            | $0.97^{+0.31}_{-0.28}$   | $0.97^{+0.23}_{-0.20}$                      | $0.39^{+0.11}_{-0.11}$ | $0.42^{+0.25}_{-0.24}$ | $1.21^{+0.18}_{-0.18}$                    | $1.10^{+0.26}_{-0.26}$                    |

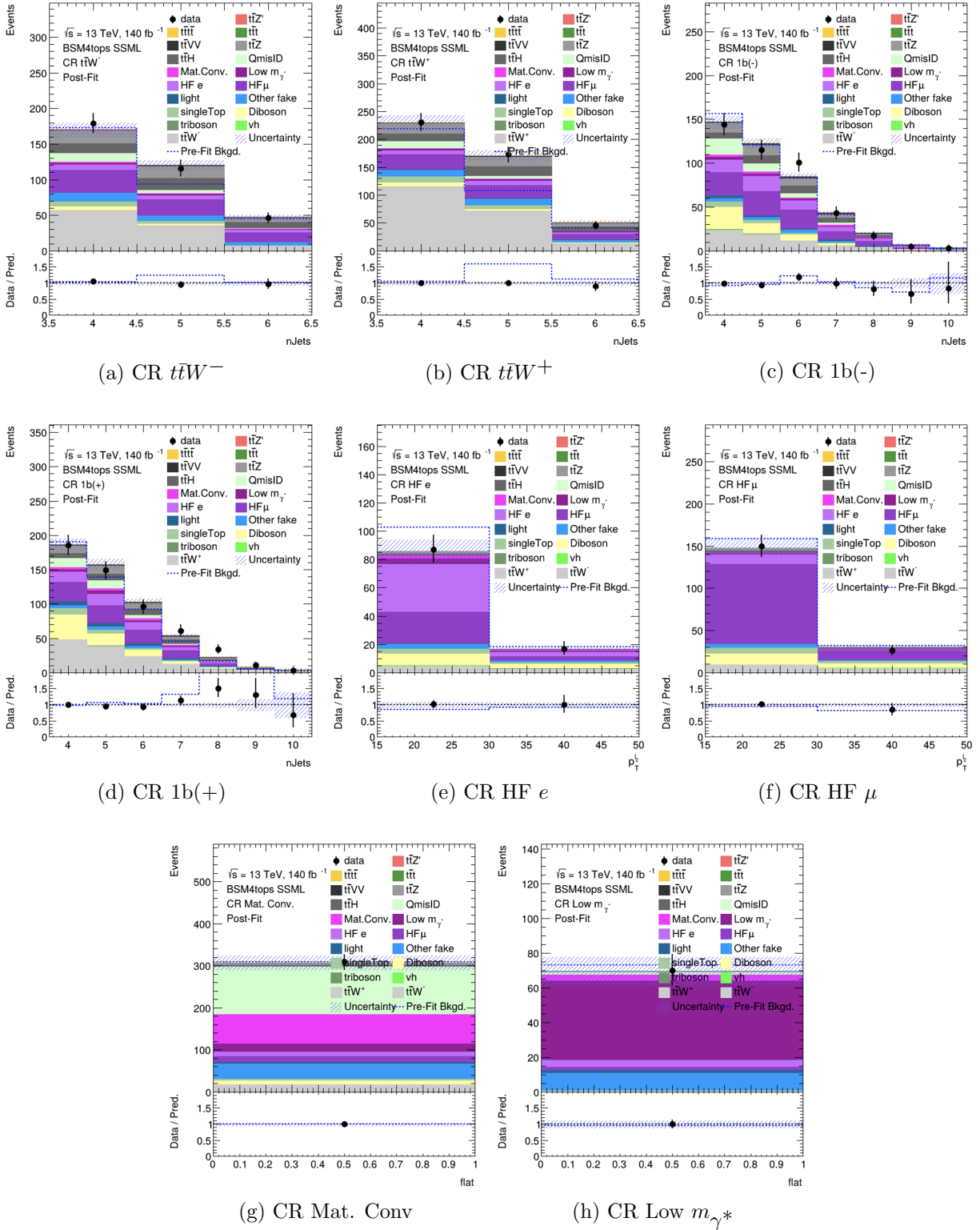
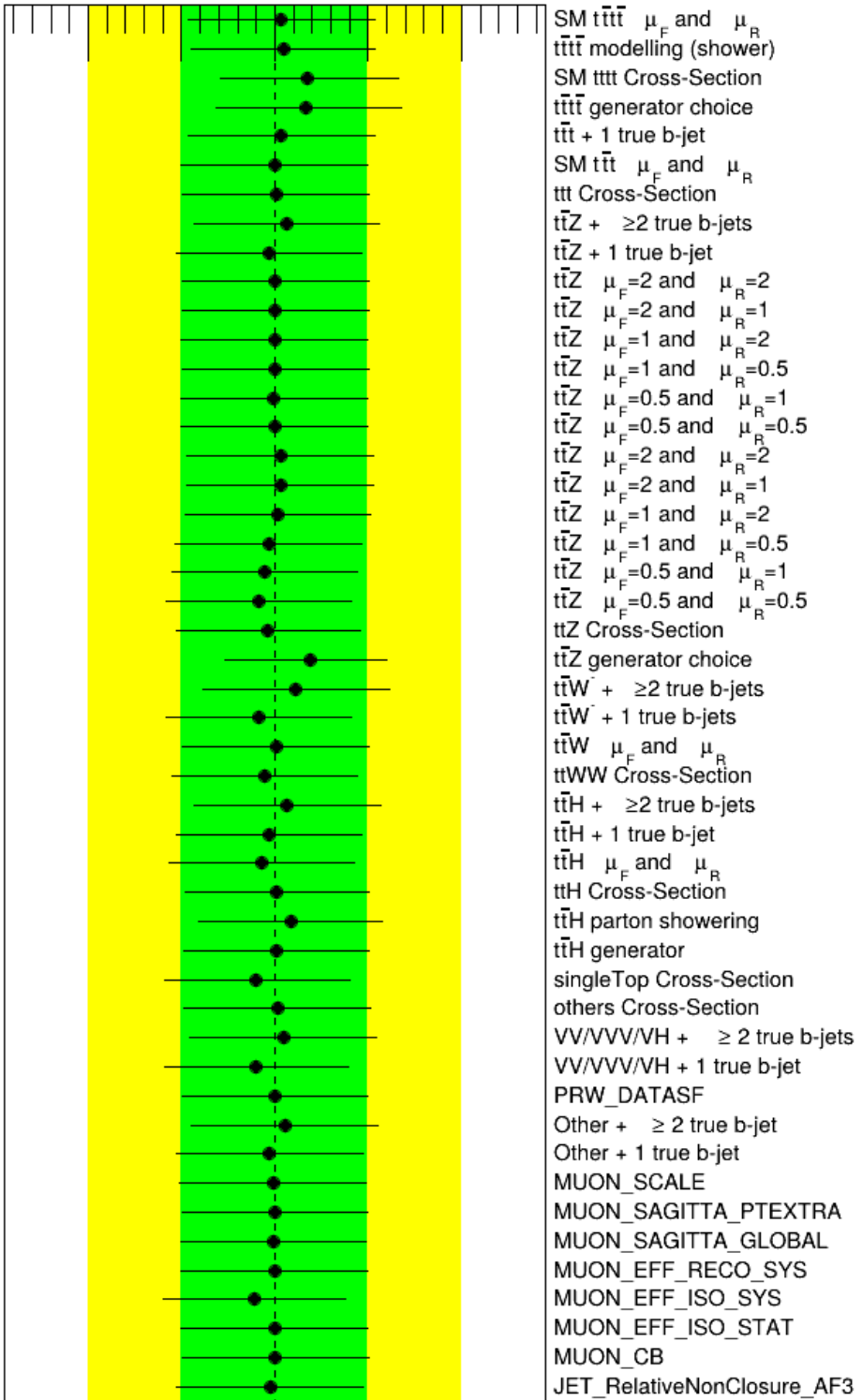
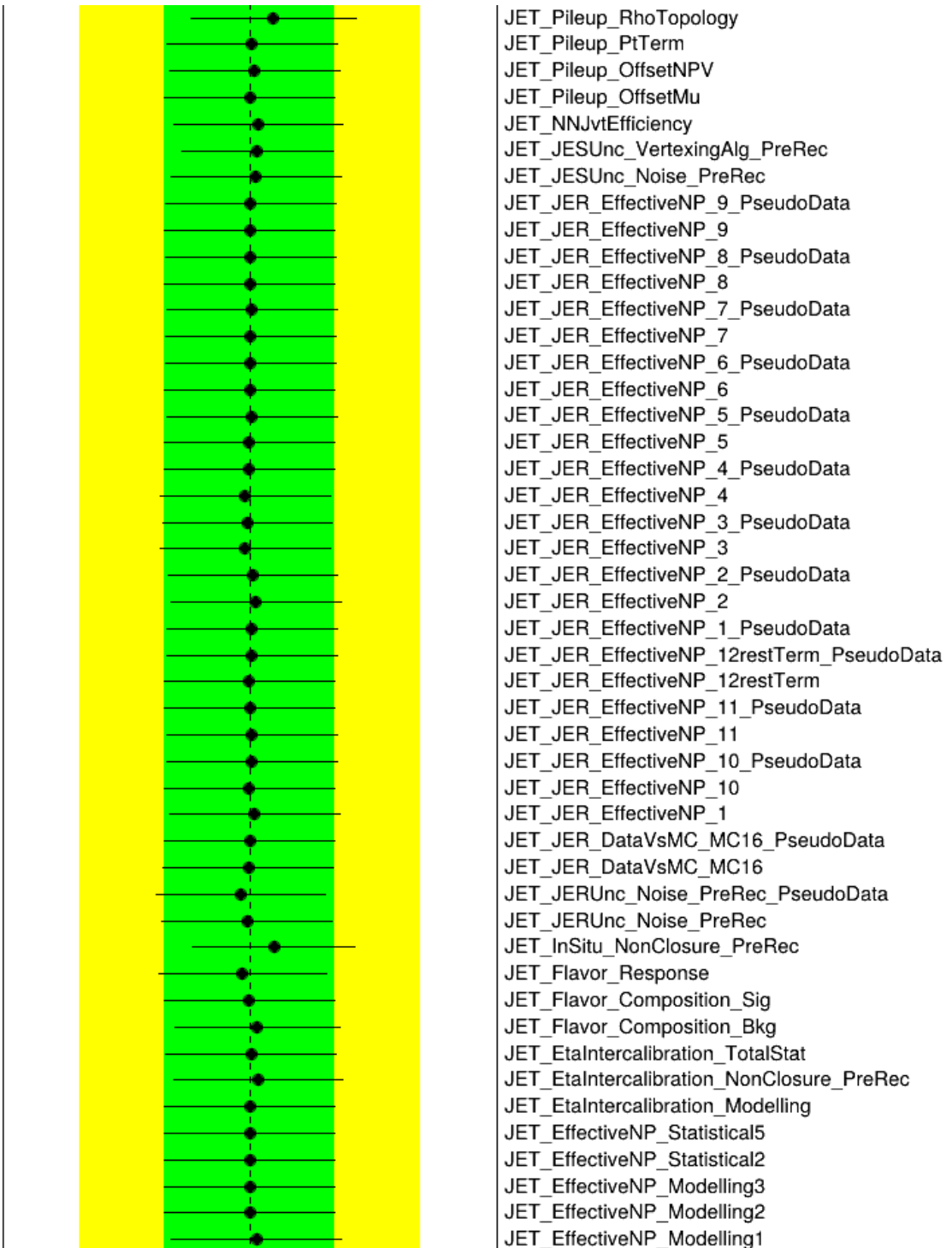


Figure 8.2: Comparison between data and post-fit prediction for the discriminant observable in each CR. Distributions shown are obtained from the fit using the  $t\bar{t}Z'$  signal sample with  $m_{Z'} = 2$  TeV. The lower panel shows the ratio between data and post-fit predictions. The shaded band represents the total uncertainty on the fit. The dashed line represents the pre-fit distribution.





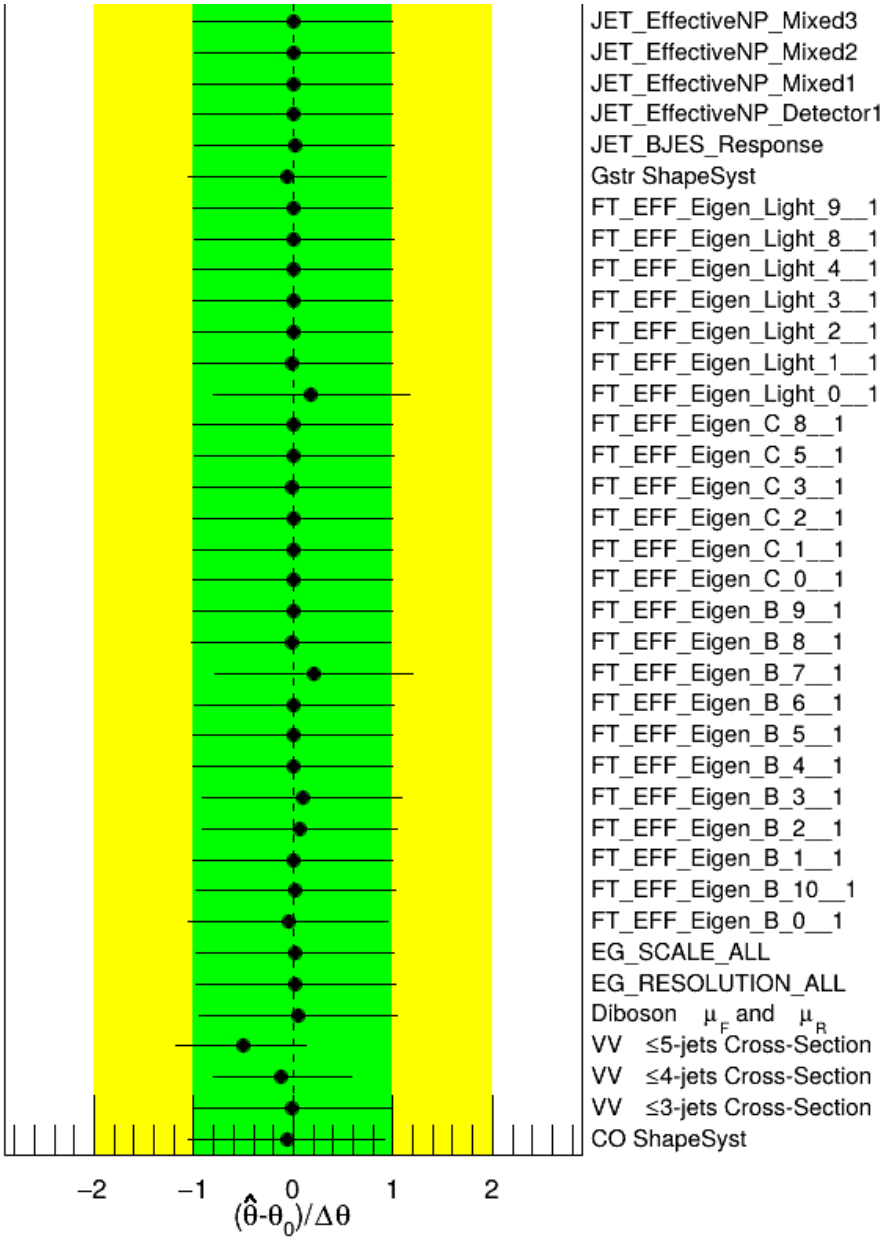


Figure 8.4: Post-fit pull from nominal values for nuisance parameters representing systematic uncertainties. Systematics pruned during the fit are not shown. The dashed line represents the nominal pre-fit values. The green and yellow bands represent the 68% ( $\pm 1\sigma$ ) and 95% ( $\pm 2\sigma$ ) confidence intervals for the nominal fit value.

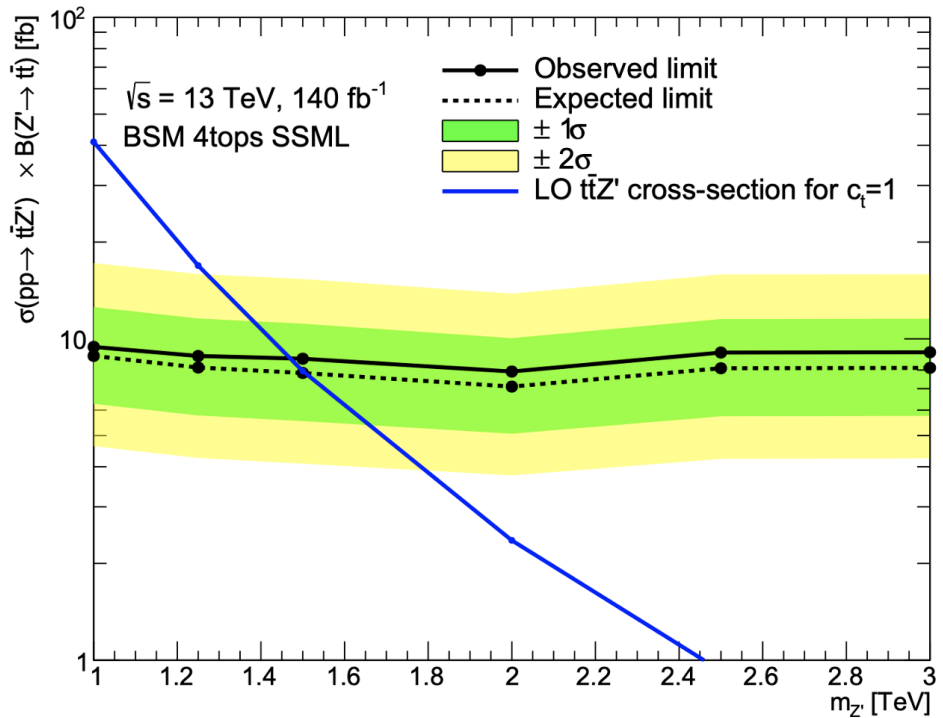


Figure 8.5: Observed (solid line) and expected (dotted line) upper limits as a function of the  $Z'$  mass at 95% CL on the cross-section of  $pp \rightarrow t\bar{t}Z'$  production times the  $Z' \rightarrow t\bar{t}$  branching ratio. The region above the observed limit is excluded. The solid blue line represents the theoretical signal cross-section with  $c_t = 1$  at LO in QCD [74]. The green and yellow bands represent the 68% ( $\pm 1\sigma$ ) and 95% ( $\pm 2\sigma$ ) confidence intervals for the expected upper limits.

Table 8.2: Pre-fit and post-fit background yields in the inclusive SR. The number of data events and pre-fit estimate signal yields are also shown. Background yields shown are obtained using the  $t\bar{t}Z'$  signal sample with  $m_{Z'} = 2$  TeV. Total yield uncertainty differs from the quadrature sum of constituent uncertainties due to (anti-)correlation effects.

<sup>†</sup>Pre-fit yields for  $t\bar{t}W$  background are nominally set to 0 prior to data-driven normalization. Yields shown are estimated using best fit parameters.

| Process  | Pre-fit                  | Post-fit           |
|--|--------------------------|--------------------|
| <b>Background</b>  |                          |                    |
| $t\bar{t}t\bar{t}$   | $42.35 \pm 5.45$         | $46.91 \pm 5.19$   |
| $t\bar{t}W^+$  | $97.38 \pm 0.71^\dagger$ | $103.93 \pm 15.91$ |
| $t\bar{t}W^-$  | $56.92 \pm 0.42^\dagger$ | $55.27 \pm 11.14$  |
| $t\bar{t}Z$  | $78.02 \pm 14.12$        | $75.57 \pm 11.13$  |
| $t\bar{t}H$  | $81.00 \pm 7.10$         | $82.90 \pm 7.30$   |
| $t\bar{t}t$  | $3.33 \pm 0.59$          | $3.37 \pm 0.60$    |
| Single-top ( $tq$ , $tZq$ , $tWZ$ , etc.)                          | $13.38 \pm 2.87$         | $12.69 \pm 2.86$   |
| $t\bar{t}VV/t\bar{t}VH/t\bar{t}HH$                                 | $17.07 \pm 4.66$         | $16.44 \pm 4.64$   |
| Charge misidentification   | $40.31 \pm 0.32$         | $40.33 \pm 0.32$   |
| $VV/VVV/VH$  | $10.01 \pm 4.76$         | $6.69 \pm 2.75$    |
| Mat. Conv.   | $26.20 \pm 0.91$         | $25.76 \pm 6.06$   |
| Low $m_{\gamma^*}$   | $26.14 \pm 0.66$         | $25.62 \pm 4.23$   |
| HF $e$   | $21.99 \pm 1.45$         | $15.42 \pm 3.70$   |
| HF $\mu$   | $31.33 \pm 3.47$         | $31.53 \pm 5.06$   |
| Light-flavor decays  | $13.47 \pm 0.53$         | $13.54 \pm 0.53$   |
| Other fake & non-prompt  | $24.90 \pm 2.26$         | $26.00 \pm 1.96$   |
| Total background   | $56.92 \pm 0.42^\dagger$ | $576.53 \pm 19.86$ |
| <b>Signal <math>t\bar{t}Z' \rightarrow t\bar{t}t\bar{t}</math></b> |                          |                    |
| $m_{Z'} = 1$ TeV   | $52.83 \pm 1.41$         | -                  |
| $m_{Z'} = 1.25$ TeV  | $52.94 \pm 1.35$         | -                  |
| $m_{Z'} = 1.5$ TeV   | $53.07 \pm 1.47$         | -                  |
| $m_{Z'} = 2$ TeV   | $52.49 \pm 1.43$         | -                  |
| $m_{Z'} = 2.5$ TeV   | $53.07 \pm 1.47$         | -                  |
| $m_{Z'} = 3$ TeV   | $52.45 \pm 1.50$         | -                  |
| <b>Data</b>  | 604                      |                    |

Table 8.3: Post-fit impact of uncertainty sources on the signal strength  $\mu$ , grouped by categories. Values shown are obtained from the fit using the  $t\bar{t}Z'$  signal sample with  $m_{Z'} = 2$  TeV. Impact on  $\mu$  is evaluated for each uncertainty category by re-fitting with the corresponding set of NPs fixed to their best-fit values. Total uncertainty differs from the quadrature sum of constituent uncertainties due to correlation between NPs in the fit.

| Uncertainty source  | $\Delta\mu$ |       |
|---|-------------|-------|
| <b>Signal modeling</b>                                      |             |       |
| $t\bar{t}Z'$  | +0.00       | -0.00 |
| <b>Background modeling</b>                                  |             |       |
| $t\bar{t}\bar{t}$   | +0.15       | -0.13 |
| $t\bar{t}W$   | +0.04       | -0.03 |
| $t\bar{t}Z$   | +0.02       | -0.02 |
| $t\bar{t}H$   | +0.02       | -0.02 |
| Non-prompt leptons  | +0.00       | -0.00 |
| Other backgrounds   | +0.02       | -0.02 |
| <b>Instrumental</b>   |             |       |
| Luminosity  | +0.00       | -0.00 |
| Jet uncertainties   | +0.04       | -0.04 |
| Jet flavor tagging ( $b$ -jets)                             | +0.04       | -0.04 |
| Jet flavor tagging ( $c$ -jets)                             | +0.01       | -0.01 |
| Jet flavor tagging (light-jets)                             | +0.02       | -0.01 |
| MC simulation sample size                                   | +0.01       | -0.01 |
| Other experimental uncertainties                            | +0.01       | -0.01 |
| Total systematic uncertainty                                | +0.15       | -0.17 |
| <b>Statistical</b>  |             |       |
| $t\bar{t}W$ NFs and scaling factors                         | +0.01       | -0.01 |
| Non-prompt lepton NFs (HF, Mat. Conv., Low $m_{\gamma^*}$ ) | +0.00       | -0.00 |
| Total statistical uncertainty                               | +0.25       | -0.23 |
| <b>Total uncertainty</b>                                    | +0.29       | -0.29 |

# 1785 Chapter 9. Summary

1786 This dissertation presents a search for BSM top-philic heavy vector resonance based on a  
1787 simplified top-philic color singlet  $Z'(\rightarrow t\bar{t})$  model in the top-quark pair associated production  
1788 channel ( $t\bar{t}Z'$ ). The search is performed in the same-sign dilepton and multilepton channel  
1789 of the  $t\bar{t}t\bar{t}$  final states, using the full Run 2 data set collected between 2015 and 2018 by the  
1790 ATLAS detector at the LHC, corresponding to an integrated luminosity of  $140 \text{ fb}^{-1}$  of  $pp$   
1791 collisions at center-of-mass energy  $\sqrt{s} = 13 \text{ TeV}$ .

1792 New data-driven estimation methods for  $t\bar{t}W$  and charge misidentification background  
1793 are employed to improve background modeling and signal sensitivity compared to previous  
1794 analysis [28]. No significant excess over Standard Model predictions is observed. Observed  
1795 exclusion limits at 95% confidence level as a function of the  $Z'$  mass are set on the production  
1796 cross section of  $pp \rightarrow t\bar{t}Z'$  times the  $Z' \rightarrow t\bar{t}$  branching ratio, ranging from  $7.9 \text{ fb}$  (at  $m_{Z'} = 2$   
1797 TeV) to  $9.4 \text{ fb}$  (at  $m_{Z'} = 1 \text{ TeV}$ ) depending on the  $Z'$  mass. This represent a significant  
1798 improvement in the exclusion limit for  $t\bar{t}Z'$  [28], and are currently the most stringent upper  
1799 limits to date. The analysis probes a  $Z'$  mass range from  $1 \text{ TeV}$  to  $3 \text{ TeV}$  under the  
1800 assumption of a top- $Z'$  coupling strength of  $c_t = 1$  and chirality angle  $\theta = \pi/4$ .

1801 Further improvements in analysis strategies, including multivariate techniques for signal  
1802 discrimination, are expected to increase discovery potential in future searches. Looking  
1803 forward, the upcoming Run 3 data at  $\sqrt{s} = 13.6 \text{ TeV}$  will increase the total integrated  
1804 luminosity by about a factor of 2 [169] and the  $pp \rightarrow t\bar{t}t\bar{t}$  cross section by at least 19% [168],  
1805 which will help to improve modeling for the SM  $t\bar{t}t\bar{t}$  background. Run 3 improvements along  
1806 with prospects of the High-Luminosity LHC will enhance sensitivity to BSM physics and offer  
1807 more opportunities to explore top-philic resonances and other exciting new phenomena.

# References

- 1808 [1] J. Schwinger. *On Quantum-Electrodynamics and the Magnetic Moment of the Elec-*  
tron. *Phys. Rev.* **73** (4 1948), pp. 416–417 (cit. on p. 1).
- 1809 [2] R. P. Feynman. *Space-Time Approach to Quantum Electrodynamics.* *Phys. Rev.* **76**  
1810 (6 1949), pp. 769–789 (cit. on p. 1).
- 1811 [3] S. Tomonaga. *On a relativistically invariant formulation of the quantum theory of*  
wave fields. *Prog. Theor. Phys.* **1** (1946), pp. 27–42 (cit. on p. 1).
- 1812 [4] E. Fermi. *An attempt of a theory of beta radiation. I.* *Nuclear Physics B* **4** (1967).  
1813 Translated from the original 1934 German article by C. P. Enz and C. H. Beck, pp. 1–  
1814 27 (cit. on p. 1).
- 1815 [5] D. J. Griffiths. *Introduction to Elementary Particles.* 2nd. Weinheim: Wiley-VCH,  
1816 2008. ISBN: 978-3-527-40601-2 (cit. on p. 1).
- 1817 [6] C. Yang and R. Mills. *Conservation of Isotopic Spin and Isotopic Gauge Invariance.*  
1818 *Phys. Rev.* **96** (1 1954), pp. 191–195 (cit. on pp. 1, 10).
- 1819 [7] A. Milsted and T. J. Osborne. *Quantum Yang-Mills theory: An overview of a program.*  
1820 *Phys. Rev. D* **98** (1 2018), p. 014505 (cit. on pp. 1, 10).

- 1824 [8] S. L. Glashow. *Partial-symmetries of weak interactions*. Nuclear Physics 22.4 (1961),  
1825 pp. 579–588. ISSN: 0029-5582 (cit. on p. 1).
- 1826 [9] D. J. Gross and F. Wilczek. *Ultraviolet Behavior of Non-Abelian Gauge Theories*.  
1827 Phys. Rev. Lett. 30 (26 1973), pp. 1343–1346 (cit. on p. 1).
- 1828 [10] H. D. Politzer. *Reliable Perturbative Results for Strong Interactions?* Phys. Rev. Lett.  
1829 30 (26 1973), pp. 1346–1349 (cit. on p. 1).
- 1830 [11] P. Higgs. *Broken symmetries and the masses of gauge bosons*. Phys. Rev. Lett. 13 (16  
1831 1964), pp. 508–509 (cit. on pp. 1, 14).
- 1832 [12] P. Higgs. *Broken symmetries, massless particles and gauge fields*. Physics Letters 12.2  
1833 (1964), pp. 132–133. ISSN: 0031-9163 (cit. on pp. 1, 14).
- 1834 [13] F. Englert and R. Brout. *Broken Symmetry and the Mass of Gauge Vector Mesons*.  
1835 Phys. Rev. Lett. 13 (9 1964), pp. 321–323 (cit. on pp. 1, 14).
- 1836 [14] S. Weinberg. *The making of the Standard Model*. The European Physical Journal C  
1837 34.1 (May 2004), 513. ISSN: 1434-6052. arXiv: hep-ph/0401010 [hep-ph] (cit. on  
1838 p. 2).
- 1839 [15] D. P. Barber et al. *Discovery of Three-Jet Events and a Test of Quantum Chromody-  
1840 namics at PETRA*. Phys. Rev. Lett. 43 (12 1979), pp. 830–833 (cit. on p. 2).
- 1841 [16] G. Arnison et al. *Experimental Observation of Isolated Large Transverse Energy Elec-  
1842 trons with Associated Missing Energy at  $\sqrt{s} = 540 \text{ GeV}$* . Phys. Lett. B 122 (1983),  
1843 pp. 103–116 (cit. on p. 2).

- 1844 [17] G. Arnison and others. *Experimental Observation of Lepton Pairs of Invariant Mass*  
1845           *Around  $95 \text{ GeV}/c^2$  at the CERN SPS Collider.* [Phys. Lett. B 126 \(1983\), pp. 398–410](#)  
1846           (cit. on p. 2).
- 1847 [18] CDF Collaboration. *Observation of Top Quark Production in  $\bar{p}p$  Collisions with the*  
1848           *Collider Detector at Fermilab.* [Phys. Rev. Lett. 74 \(14 1995\), pp. 2626–2631](#) (cit. on  
1849           p. 2).
- 1850 [19] DØ Collaboration. *Observation of the Top Quark.* [Phys. Rev. Lett. 74 \(14 1995\),](#)  
1851           pp. 2632–2637 (cit. on p. 2).
- 1852 [20] ATLAS Collaboration. *Observation of a new particle in the search for the Standard*  
1853           *Model Higgs boson with the ATLAS detector at the LHC.* [Phys. Lett. B 716 \(2012\),](#)  
1854           p. 1. arXiv: 1207.7214 [[hep-ex](#)] (cit. on pp. 2, 14).
- 1855 [21] CMS Collaboration. *Observation of a new boson at a mass of 125 GeV with the CMS*  
1856           *experiment at the LHC.* [Phys. Lett. B 716 \(2012\), p. 30.](#) arXiv: 1207.7235 [[hep-ex](#)]  
1857           (cit. on pp. 2, 14).
- 1858 [22] S. Navas et al. *Review of particle physics.* [Phys. Rev. D 110.3 \(2024\), p. 030001](#) (cit.  
1859           on pp. 2, 7, 8).
- 1860 [23] Y. Fukuda et al. *Evidence for Oscillation of Atmospheric Neutrinos.* [Phys. Rev. Lett.](#)  
1861           81 (8 1998), pp. 1562–1567 (cit. on p. 2).
- 1862 [24] M. Cristinziani and M. Mulders. *Top-quark physics at the Large Hadron Collider.*  
1863           Journal of Physics G: Nuclear and Particle Physics 44.6 (2017), p. 063001. arXiv:  
1864           1606.00327 [[hep-ex](#)] (cit. on pp. 2, 8).

- 1865 [25] ATLAS and CMS Collaborations. *Combination of inclusive top-quark pair production*  
1866 *cross-section measurements using ATLAS and CMS data at  $\sqrt{s} = 7$  and 8 TeV.* *JHEP*  
1867 **07** (2023), p. 213. arXiv: [2205.13830 \[hep-ex\]](#) (cit. on p. 3).
- 1868 [26] C. Degrande, J.-M. Grard, C. Grojean, F. Maltoni, and G. Servant. *Non-resonant new*  
1869 *physics in top pair production at hadron colliders.* *Journal of High Energy Physics*  
1870 **2011.3** (Mar. 2011). ISSN: 1029-8479. arXiv: [1010.6304 \[hep-ph\]](#) (cit. on p. 3).
- 1871 [27] ATLAS Collaboration. *The ATLAS Experiment at the CERN Large Hadron Collider.*  
1872 *JINST* **3** (2008), S08003 (cit. on pp. 3, 22, 25, 26, 28–32).
- 1873 [28] ATLAS Collaboration. *Search for top-philic heavy resonances in pp collisions at  $\sqrt{s} =$*   
1874 *13 TeV with the ATLAS detector.* *Eur. Phys. J. C* **84** (2024), p. 157. arXiv: [2304.01678 \[hep-ex\]](#) (cit. on pp. 3, 4, 18, 97).
- 1875 [29] H. P. Nilles. *Supersymmetry, Supergravity and Particle Physics.* *Phys. Rept.* **110**  
1877 (1984), pp. 1–162 (cit. on p. 3).
- 1878 [30] G. R. Farrar and P. Fayet. *Phenomenology of the Production, Decay, and Detection*  
1879 *of New Hadronic States Associated with Supersymmetry.* *Phys. Lett. B* **76** (1978),  
1880 pp. 575–579 (cit. on p. 3).
- 1881 [31] T. Plehn and T. M. P. Tait. *Seeking sgluons.* *Journal of Physics G: Nuclear and*  
1882 *Particle Physics* **36.7** (2009), p. 075001. arXiv: [0810.3919 \[hep-ph\]](#) (cit. on p. 3).
- 1883 [32] S. Calvet, B. Fuks, P. Gris, and L. Valry. *Searching for sgluons in multitop events*  
1884 *at a center-of-mass energy of 8 TeV.* *Journal of High Energy Physics* **2013.4** (Apr.  
1885 2013). ISSN: 1029-8479. arXiv: [1212.3360 \[hep-ph\]](#) (cit. on p. 3).

- 1886 [33] A. Pomarol and J. Serra. *Top quark compositeness: Feasibility and implications*. Phys-  
1887       ical Review D 78.7 (Oct. 2008). ISSN: 1550-2368. arXiv: 0806.3247 [hep-ph] (cit. on  
1888       p. 3).
- 1889 [34] K. Kumar, T. M. Tait, and R. Vega-Morales. *Manifestations of top compositeness at*  
1890       *colliders*. Journal of High Energy Physics 2009.05 (May 2009), 022022. ISSN: 1029-  
1891       8479. arXiv: 0901.3808 [hep-ph] (cit. on p. 3).
- 1892 [35] G. Banelli, E. Salvioni, J. Serra, T. Theil, and A. Weiler. *The present and future of*  
1893       *four top operators*. Journal of High Energy Physics 2021.2 (Feb. 2021). ISSN: 1029-  
1894       8479. arXiv: 2010.05915 [hep-ph] (cit. on p. 3).
- 1895 [36] R. Aoude, H. El Faham, F. Maltoni, and E. Vryonidou. *Complete SMEFT predictions*  
1896       *for four top quark production at hadron colliders*. Journal of High Energy Physics  
1897       2022.10 (Oct. 2022). ISSN: 1029-8479. arXiv: 2208.04962 [hep-ph] (cit. on p. 3).
- 1898 [37] C. Zhang. *Constraining qqtt operators from four-top production: a case for enhanced*  
1899       *EFT sensitivity*. Chinese Physics C 42.2 (Feb. 2018), p. 023104. ISSN: 1674-1137.  
1900       arXiv: 1708.05928 [hep-ph] (cit. on p. 3).
- 1901 [38] L. Darmé, B. Fuks, and F. Maltoni. *Topophilic heavy resonances in four-top final*  
1902       *states and their EFT interpretation*. Journal of High Energy Physics 2021.9 (Sept.  
1903       2021). ISSN: 1029-8479. arXiv: 2104.09512 [hep-ph] (cit. on pp. 3, 17).
- 1904 [39] N. Craig, F. D'Eramo, P. Draper, S. Thomas, and H. Zhang. *The Hunt for the Rest*  
1905       *of the Higgs Bosons*. JHEP 06 (2015), p. 137. arXiv: 1504.04630 [hep-ph] (cit. on  
1906       pp. 3, 17).

- 1907 [40] N. Craig, J. Hajer, Y.-Y. Li, T. Liu, and H. Zhang. *Heavy Higgs bosons at low  $\tan \beta$ :  
1908 from the LHC to 100 TeV*. Journal of High Energy Physics 2017.1 (Jan. 2017). ISSN:  
1909 1029-8479. arXiv: 1605.08744 [hep-ph] (cit. on pp. 3, 17).
- 1910 [41] G. C. Branco et al. *Theory and phenomenology of two-Higgs-doublet models*. Phys.  
1911 Rept. 516 (2012), pp. 1–102. arXiv: 1106.0034 [hep-ph] (cit. on pp. 3, 17).
- 1912 [42] S. Gori, I.-W. Kim, N. R. Shah, and K. M. Zurek. *Closing the wedge: Search strategies  
1913 for extended Higgs sectors with heavy flavor final states*. Phys. Rev. D 93 (7 2016),  
1914 p. 075038 (cit. on pp. 3, 17).
- 1915 [43] P. S. B. Dev and A. Pilaftsis. *Maximally symmetric two Higgs doublet model with  
1916 natural Standard Model alignment*. Journal of High Energy Physics 2014.12 (Dec.  
1917 2014), p. 024. arXiv: 1408.3405 [hep-ph] (cit. on pp. 3, 17).
- 1918 [44] ATLAS Collaboration. *Observation of four-top-quark production in the multilepton  
1919 final state with the ATLAS detector*. Eur. Phys. J. C 83 (2023), p. 496. arXiv: 2303.  
1920 15061 [hep-ex] (cit. on pp. 3, 4, 18, 51, 64, 72, 80).
- 1921 [45] N. Greiner, K. Kong, J.-C. Park, S. C. Park, and J.-C. Winter. *Model-independent  
1922 production of a topophilic resonance at the LHC*. Journal of High Energy Physics  
1923 2015.4 (2015), p. 29. ISSN: 1029-8479. arXiv: 1410.6099 [hep-ph] (cit. on pp. 3, 18–  
1924 20).
- 1925 [46] ATLAS Collaboration. *Search for  $t\bar{t}H/A \rightarrow t\bar{t}t\bar{t}$  production in the multilepton final  
1926 state in proton–proton collisions at  $\sqrt{s} = 13$  TeV with the ATLAS detector*. JHEP 07  
1927 (2023), p. 203. arXiv: 2211.01136 [hep-ex] (cit. on p. 4).

- 1928 [47] ATLAS Collaboration. *Evidence for  $t\bar{t}t\bar{t}$  production in the multilepton final state in*
- 1929 proton–proton collisions at  $\sqrt{s} = 13\text{TeV}$  with the ATLAS detector. *Eur. Phys. J. C*
- 1930 80 (2020), p. 1085. arXiv: 2007.14858 [hep-ex] (cit. on pp. 4, 71).
- 1931 [48] D. H. Perkins. *Introduction to High Energy Physics*. 4th. Cambridge, UK: Cambridge
- 1932 University Press, Apr. 2000. ISBN: 9780521621960 (cit. on p. 5).
- 1933 [49] C. Burgard and D. Galbraith. *Standard Model of Physics*. URL: <https://texample.net/model-physics/> (visited on 06/02/2025) (cit. on p. 6).
- 1935 [50] H. Georgi. *Lie Algebras in Particle Physics: from Isospin to Unified Theories*. 2nd.
- 1936 CRC Press, 2000. ISBN: 9780429499210 (cit. on pp. 7, 10).
- 1937 [51] ATLAS and CMS Collaborations. *Combination of Measurements of the Top Quark*
- 1938 *Mass from Data Collected by the ATLAS and CMS Experiments at  $\sqrt{s} = 7$  and 8 TeV*.
- 1939 *Phys. Rev. Lett.* 132 (2023), p. 261902. arXiv: 2402.08713 [hep-ex] (cit. on p. 8).
- 1940 [52] H. de la Torre and T. Farooque. *Looking beyond the Standard Model with Third Gen-*
- 1941 *eration Quarks at the LHC*. *Symmetry* 14.3 (2022), p. 444 (cit. on p. 8).
- 1942 [53] Q.-H. Cao, J.-N. Fu, Y. Liu, X.-H. Wang, and R. Zhang. *Probing Top-philic New*
- 1943 *Physics via Four-Top-Quark Production*. *Chinese Physics C* 45.9 (2021), p. 093107.
- 1944 arXiv: 2105.03372 [hep-ph] (cit. on p. 8).
- 1945 [54] H. Beauchesne et al. *A case study about BSM vector resonances with direct couplings*
- 1946 *to the third quark generation*. *European Physical Journal C* 80.5 (2020), p. 485. arXiv:
- 1947 1908.11619 [hep-ph] (cit. on p. 8).
- 1948 [55] F. Maltoni, D. Pagani, and S. Tentori. *Top-quark pair production as a probe of light*
- 1949 *top-philic scalars and anomalous Higgs interactions*. *Journal of High Energy Physics*
- 1950 2024.9 (Sept. 2024), p. 098. arXiv: 2406.06694 [hep-ph] (cit. on p. 8).

- 1951 [56] CMS Collaboration. *Search for  $t\bar{t}H$  production in the  $H \rightarrow b\bar{b}$  decay channel with*
- 1952            leptonic  $t\bar{t}$  decays in proton–proton collisions at  $\sqrt{s} = 13$  TeV. JHEP 03 (2019),
- 1953            p. 026. arXiv: 1804.03682 [hep-ex] (cit. on p. 8).
- 1954 [57] Y. Grossman and Y. Nir. *The Standard Model: From Fundamental Symmetries to Ex-*
- 1955            *perimental Tests.* See Chapter 8.2. Cambridge University Press, 2023. ISBN: 9781009320378
- 1956            (cit. on p. 9).
- 1957 [58] M. E. Peskin and D. V. Schroeder. *An Introduction to Quantum Field Theory.* 1st.
- 1958            Reading, MA, USA: AddisonWesley, 1995. ISBN: 978-0-201-50397-5 (cit. on p. 9).
- 1959 [59] D. J. Gross. *The role of symmetry in fundamental physics.* Proceedings of the National
- 1960            Academy of Sciences of the United States of America 93.25 (Dec. 1996), pp. 14256–
- 1961            14259 (cit. on p. 9).
- 1962 [60] M. Bañados and I. Reyes. *A short review on Noethers theorems, gauge symmetries*
- 1963            *and boundary terms.* International Journal of Modern Physics D 25.10 (Aug. 2016),
- 1964            p. 1630021. ISSN: 1793-6594. arXiv: 1601.03616 [hep-th] (cit. on p. 9).
- 1965 [61] A. Pich. *The Standard Model of electroweak interactions.* 2004 European School of
- 1966            High-Energy Physics. Feb. 2005, pp. 1–48. arXiv: hep-ph/0502010 [hep-ex] (cit. on
- 1967            pp. 11–13).
- 1968 [62] P. Dev and A. Pilaftsis. *High-temperature electroweak symmetry non-restoration from*
- 1969            *new fermions and implications for baryogenesis.* Journal of High Energy Physics
- 1970            2020.9 (Sept. 2020), p. 012. arXiv: 2002.05174 [hep-ph] (cit. on p. 13).
- 1971 [63] J. Riebesell. *Higgs Potential.* URL: <https://tikz.net/higgs-potential/> (visited on
- 1972            07/07/2025) (cit. on p. 15).

- 1973 [64] J. Goldstone, A. Salam, and S. Weinberg. *Broken Symmetries*. Phys. Rev. 127 (3  
1974 1962), pp. 965–970 (cit. on p. 15).
- 1975 [65] J. Ellis. *Higgs Physics. 2013 European School of High-Energy Physics*. 2015, pp. 117–  
1976 168. arXiv: 1312.5672 [hep-ph] (cit. on pp. 15, 16).
- 1977 [66] G. Ferretti and D. Karateev. *Fermionic UV completions of composite Higgs models*.  
1978 Journal of High Energy Physics 2014.3 (Mar. 2014). ISSN: 1029-8479 (cit. on p. 17).
- 1979 [67] L. Vecchi. *A dangerous irrelevant UV-completion of the composite Higgs*. JHEP 02  
1980 (2017), p. 094. arXiv: 1506.00623 [hep-ph] (cit. on p. 17).
- 1981 [68] CDF Collaboration. *Search for New Physics in High-Mass Electron-Positron Events  
1982 in  $p\bar{p}$  Collisions at  $\sqrt{s} = 1.96$  TeV*. Phys. Rev. Lett. 99 (17 2007), p. 171802. arXiv:  
1983 0707.2524 [hep-ex] (cit. on p. 17).
- 1984 [69] M. Battaglia and G. Servant. *Four-top production and  $t\bar{t}$ +missing energy events at  
1985 multi TeV  $e^+e^-$  colliders*. Nuovo Cim. C 033N2 (2010), pp. 203–208. arXiv: 1005.4632  
1986 [hep-ex] (cit. on p. 17).
- 1987 [70] N. Arkani-Hamed, A. G. Cohen, and H. Georgi. *Electroweak symmetry breaking from  
1988 dimensional deconstruction*. Physics Letters B 513.1-2 (July 2001), pp. 232–240. arXiv:  
1989 hep-ph/0105239 [hep-ph] (cit. on p. 17).
- 1990 [71] T. Han, H. E. Logan, B. McElrath, and L.-T. Wang. *Phenomenology of the little Higgs  
1991 model*. Phys. Rev. D 67 (9 2003), p. 095004. arXiv: hep-ph/0301040 [hep-ph] (cit. on  
1992 p. 17).
- 1993 [72] P. Langacker and M. Plümacher. *Flavor changing effects in theories with a heavy  $Z'$   
1994 boson with family nonuniversal couplings*. Phys. Rev. D 62 (1 2000), p. 013006. arXiv:  
1995 hep-ph/0001204 [hep-ph].

- 1996 [73] P. Langacker. *The Physics of Heavy  $Z'$  Gauge Bosons*. *Rev. Mod. Phys.* **81** (2009),  
1997 pp. 1199–1228. arXiv: [0801.1345 \[hep-ph\]](#) (cit. on p. 17).
- 1998 [74] J. H. Kim, K. Kong, S. J. Lee, and G. Mohlabeng. *Probing TeV scale top-philic*  
1999 *resonances with boosted top-tagging at the high luminosity LHC*. *Phys. Rev. D* **94** (3  
2000 2016), p. 035023. arXiv: [1604.07421 \[hep-ph\]](#) (cit. on pp. xi, 17, 18, 20, 86, 94).
- 2001 [75] P. J. Fox, I. Low, and Y. Zhang. *Top-philic  $Z'$  forces at the LHC*. *Journal of High*  
2002 *Energy Physics* **2018**.3 (Mar. 2018). ISSN: 1029-8479. arXiv: [1801.03505 \[hep-ph\]](#)  
2003 (cit. on p. 17).
- 2004 [76] CMS Collaboration. *Observation of four top quark production in proton-proton col-*  
2005 *lisions at  $\sqrt{s} = 13\text{TeV}$* . *Physics Letters B* **847** (2023), p. 138290. arXiv: [2305.13439](#)  
2006 [[hep-ex](#)] (cit. on p. 18).
- 2007 [77] G. Brooijmans et al. *New Physics at the LHC. A Les Houches Report: Physics at*  
2008 *TeV Colliders 2009 - New Physics Working Group. 6th Les Houches Workshop on*  
2009 *Physics at TeV Colliders*. See Chapter 12. May 2010, pp. 191–380. arXiv: [1005.1229](#)  
2010 [[hep-ph](#)] (cit. on p. 20).
- 2011 [78] P. Sabatini. *Evidence for four-top-quarks production with the ATLAS detector at the*  
2012 *Large Hadron Collider*. Tech. rep. Geneva: CERN, 2021. URL: <https://cds.cern.ch/record/2784150> (cit. on p. 21).
- 2014 [79] L. Evans and P. Bryant. *LHC Machine*. *JINST* **3** (2008), S08001 (cit. on p. 22).
- 2015 [80] CMS Collaboration. *The CMS Experiment at the CERN LHC*. *JINST* **3** (2008),  
2016 S08004 (cit. on p. 22).
- 2017 [81] The ALICE Collaboration. *The ALICE experiment at the CERN LHC*. *JINST* **3**  
2018 (2008), S08002 (cit. on p. 22).

- 2019 [82] The LHCb Collaboration. *The LHCb Detector at the LHC*. *JINST* **3** (2008), S08005  
2020 (cit. on p. 22).
- 2021 [83] E. e. a. Gschwendtner. *AWAKE, The Advanced Proton Driven Plasma Wakefield*  
2022 *Acceleration Experiment at CERN*. Nuclear Instruments and Methods in Physics Re-  
2023 search Section A **829** (2016), pp. 76–82. arXiv: 1512.05498 [physics.acc-ph] (cit. on  
2024 p. 23).
- 2025 [84] J. L. Feng, I. Galon, F. Kling, and S. Trojanowski. *ForwArd Search ExpeRiment at*  
2026 *the LHC*. *Phys. Rev. D* **97** (3 2018), p. 035001. arXiv: 1708.09389 [hep-ph] (cit. on  
2027 p. 23).
- 2028 [85] The KATRIN collaboration. *The design, construction, and commissioning of the KA-*  
2029 *TRIN experiment*. *Journal of Instrumentation* **16.08** (2021), T08015. arXiv: 2103.  
2030 04755 [physics.ins-det] (cit. on p. 23).
- 2031 [86] E. Lopienska. *The CERN accelerator complex, layout in 2022*. General Photo. 2022.  
2032 URL: <https://cds.cern.ch/record/2800984> (visited on 07/08/2025) (cit. on p. 23).
- 2033 [87] High Luminosity LHC Project Organization. *The HL-LHC project*. 2025. URL: <https://hilumilhc.web.cern.ch/content/hl-lhc-project> (visited on 06/11/2025) (cit. on  
2034 p. 24).
- 2035 [88] ATLAS Collaboration. *Performance of the ATLAS detector using first collision data*.  
2036 *JHEP* **09** (2010), p. 056. arXiv: 1005.5254 [hep-ex] (cit. on p. 24).
- 2038 [89] ATLAS Collaboration. *Luminosity determination in pp collisions at  $\sqrt{s} = 13 \text{ TeV}$*   
2039 *using the ATLAS detector at the LHC*. *Eur. Phys. J. C* **83** (2023), p. 982. arXiv:  
2040 2212.09379 [hep-ex] (cit. on pp. 25, 51, 74).

- 2041 [90] J. M. Butterworth, G. Dissertori, and G. P. Salam. *Hard Processes in Proton-Proton*  
2042 *Collisions at the Large Hadron Collider*. *Annu. Rev. Nucl. Part. Sci.* **62** (2012),  
2043 pp. 387–405. arXiv: [1202.0583 \[hep-ex\]](https://arxiv.org/abs/1202.0583) (cit. on p. 25).
- 2044 [91] J. Campbell, J. Huston, and W. J. Stirling. *Hard interactions of quarks and gluons:*  
2045 *a primer for LHC physics*. *Reports on Progress in Physics* **70**.1 (2006), p. 89. arXiv:  
2046 [hep-ph/0611148 \[hep-ex\]](https://arxiv.org/abs/hep-ph/0611148) (cit. on p. 25).
- 2047 [92] ATLAS Collaboration. *Standard Model Summary Plots October 2023*. ATL-PHYS-  
2048 PUB-2023-039. 2023. URL: <https://cds.cern.ch/record/2882448> (cit. on p. 26).
- 2049 [93] J. Pequenao and P. Schaffner. *How ATLAS detects particles: diagram of particle*  
2050 *paths in the detector*. 2013. URL: <https://cds.cern.ch/record/1505342> (visited on  
2051 07/08/2025) (cit. on p. 27).
- 2052 [94] J. Pequenao. *Computer generated image of the ATLAS inner detector*. 2008. URL:  
2053 <https://cds.cern.ch/record/1095926> (visited on 07/08/2025) (cit. on p. 28).
- 2054 [95] J. Pequenao. *Computer Generated image of the ATLAS calorimeter*. 2008. URL: <https://cds.cern.ch/record/1095927> (visited on 07/08/2025) (cit. on p. 30).
- 2056 [96] ATLAS Collaboration. *Operation of the ATLAS trigger system in Run 2*. *JINST* **15**  
2057 (2020), P10004. arXiv: [2007.12539 \[physics.ins-det\]](https://arxiv.org/abs/2007.12539) (cit. on p. 33).
- 2058 [97] ATLAS Collaboration. *Performance of the ATLAS track reconstruction algorithms*  
2059 *in dense environments in LHC Run 2*. *Eur. Phys. J. C* **77** (2017), p. 673. arXiv:  
2060 [1704.07983 \[hep-ex\]](https://arxiv.org/abs/1704.07983) (cit. on p. 34).
- 2061 [98] T. Cornelissen et al. *Concepts, design and implementation of the ATLAS New Track-*  
2062 *ing (NEWT)*. Tech. rep. Geneva: CERN, 2007. URL: <https://cds.cern.ch/record/1020106> (cit. on p. 34).

- 2064 [99] A. Salzburger. *Optimisation of the ATLAS Track Reconstruction Software for Run-2*.  
2065 Journal of Physics: Conference Series 664.7 (2015), p. 072042 (cit. on p. 34).
- 2066 [100] R. Frühwirth. *Application of Kalman filtering to track and vertex fitting*. Nucl. In-  
2067 strum. Methods Phys. Res. A 262.2 (1987), pp. 444–450. ISSN: 0168-9002 (cit. on  
2068 p. 34).
- 2069 [101] T. Cornelissen et al. *The global  $\chi^2$  track fitter in ATLAS*. Journal of Physics: Con-  
2070 ference Series 119.3 (2008), p. 032013 (cit. on p. 34).
- 2071 [102] ATLAS Collaboration. *Improved electron reconstruction in ATLAS using the Gaus-  
2072 sian Sum Filter-based model for bremsstrahlung*. ATLAS-CONF-2012-047. 2012. URL:  
2073 <https://cds.cern.ch/record/1449796> (cit. on p. 34).
- 2074 [103] D. Wicke. *A new algorithm for solving tracking ambiguities*. Tech. rep. Oct. 1998.  
2075 URL: <https://cds.cern.ch/record/2625731> (cit. on p. 35).
- 2076 [104] ATLAS Collaboration. *Reconstruction of primary vertices at the ATLAS experiment  
2077 in Run 1 proton–proton collisions at the LHC*. Eur. Phys. J. C 77 (2017), p. 332.  
2078 arXiv: [1611.10235 \[physics.ins-det\]](https://arxiv.org/abs/1611.10235) (cit. on p. 35).
- 2079 [105] W. Waltenberger, R. Frühwirth, and P. Vanlaer. *Adaptive vertex fitting*. Journal of  
2080 Physics G: Nuclear and Particle Physics 34.12 (2007), N343 (cit. on p. 35).
- 2081 [106] ATLAS Collaboration. *Secondary vertex finding for jet flavour identification with the  
2082 ATLAS detector*. ATL-PHYS-PUB-2017-011. 2017. URL: <https://cds.cern.ch/record/2270366> (cit. on p. 35).
- 2084 [107] ATLAS Collaboration. *Performance of pile-up mitigation techniques for jets in pp  
2085 collisions at  $\sqrt{s} = 8 \text{ TeV}$  using the ATLAS detector*. Eur. Phys. J. C 76 (2016),  
2086 p. 581. arXiv: [1510.03823 \[hep-ex\]](https://arxiv.org/abs/1510.03823) (cit. on pp. 36, 39).

- 2087 [108] ATLAS Collaboration. *Topological cell clustering in the ATLAS calorimeters and its*  
2088 *performance in LHC Run 1.* *Eur. Phys. J. C* **77** (2017), p. 490. arXiv: [1603.02934](#)  
2089 [[hep-ex](#)] (cit. on pp. 36, 37).
- 2090 [109] ATLAS Collaboration. *Jet reconstruction and performance using particle flow with*  
2091 *the ATLAS Detector.* *Eur. Phys. J. C* **77** (2017), p. 466. arXiv: [1703.10485](#) [[hep-ex](#)]  
2092 (cit. on p. 38).
- 2093 [110] M. Cacciari, G. P. Salam, and G. Soyez. *The anti- $k_t$  jet clustering algorithm.* *JHEP*  
2094 **04** (2008), p. 063. arXiv: [0802.1189](#) [[hep-ph](#)] (cit. on p. 38).
- 2095 [111] ATLAS Collaboration. *Jet energy scale and resolution measured in proton–proton*  
2096 *collisions at  $\sqrt{s} = 13\text{ TeV}$  with the ATLAS detector.* *Eur. Phys. J. C* **81** (2021),  
2097 p. 689. arXiv: [2007.02645](#) [[hep-ex](#)] (cit. on pp. 39, 75–77).
- 2098 [112] ATLAS Collaboration. *Jet energy scale measurements and their systematic uncertain-*  
2099 *ties in proton–proton collisions at  $\sqrt{s} = 13\text{ TeV}$  with the ATLAS detector.* *Phys. Rev.*  
2100 **D 96** (2017), p. 072002. arXiv: [1703.09665](#) [[hep-ex](#)] (cit. on pp. 39, 75).
- 2101 [113] ATLAS Collaboration. *Transforming jet flavour tagging at ATLAS.* Tech. rep. Sub-  
2102 mitted to: Nature Communications. Geneva: CERN, 2025. arXiv: [2505.19689](#) (cit. on  
2103 pp. 40–42).
- 2104 [114] A. Vaswani et al. *Attention Is All You Need.* 2023. arXiv: [1706.03762](#) [[cs.CL](#)] (cit. on  
2105 p. 40).
- 2106 [115] ATLAS Collaboration. *Measurements of  $b$ -jet tagging efficiency with the ATLAS de-*  
2107 *tector using  $t\bar{t}$  events at  $\sqrt{s} = 13\text{ TeV}.$*  *JHEP* **08** (2018), p. 089. arXiv: [1805.01845](#)  
2108 [[hep-ex](#)] (cit. on pp. 42, 77).

- 2109 [116] ATLAS Collaboration. *Electron reconstruction and identification in the ATLAS ex-*  
 2110 *periment using the 2015 and 2016 LHC proton–proton collision data at  $\sqrt{s} = 13$  TeV.*  
 2111 *Eur. Phys. J. C* **79** (2019), p. 639. arXiv: [1902.04655 \[physics.ins-det\]](#) (cit. on  
 2112 pp. 43–45).
- 2113 [117] ATLAS Collaboration. *Muon reconstruction and identification efficiency in ATLAS*  
 2114 *using the full Run 2 pp collision data set at  $\sqrt{s} = 13$  TeV.* *Eur. Phys. J. C* **81** (2021),  
 2115 p. 578. arXiv: [2012.00578 \[hep-ex\]](#) (cit. on pp. 46, 47).
- 2116 [118] ATLAS Collaboration. *Muon reconstruction performance of the ATLAS detector in*  
 2117 *proton–proton collision data at  $\sqrt{s} = 13$  TeV.* *Eur. Phys. J. C* **76** (2016), p. 292. arXiv:  
 2118 [1603.05598 \[hep-ex\]](#) (cit. on p. 47).
- 2119 [119] ATLAS Collaboration. *Performance of missing transverse momentum reconstruction*  
 2120 *with the ATLAS detector using proton–proton collisions at  $\sqrt{s} = 13$  TeV.* *Eur. Phys.*  
 2121 *J. C* **78** (2018), p. 903. arXiv: [1802.08168 \[hep-ex\]](#) (cit. on pp. 48, 77).
- 2122 [120] ATLAS Collaboration.  *$E_T^{\text{miss}}$  performance in the ATLAS detector using 2015–2016*  
 2123 *LHC pp collisions.* ATLAS-CONF-2018-023. 2018. URL: <https://cds.cern.ch/record/2625233> (cit. on p. 49).
- 2125 [121] J. Alwall et al. *The automated computation of tree-level and next-to-leading order*  
 2126 *differential cross sections, and their matching to parton shower simulations.* *JHEP* **07**  
 2127 (2014), p. 079. arXiv: [1405.0301 \[hep-ph\]](#) (cit. on pp. 52, 54–57).
- 2128 [122] NNPDF Collaboration, R. D. Ball, et al. *Parton distributions for the LHC run II.*  
 2129 *JHEP* **04** (2015), p. 040. arXiv: [1410.8849 \[hep-ph\]](#) (cit. on pp. 52, 54–58).
- 2130 [123] T. Sjöstrand et al. *An introduction to PYTHIA 8.2.* *Comput. Phys. Commun.* **191**  
 2131 (2015), p. 159. arXiv: [1410.3012 \[hep-ph\]](#) (cit. on pp. 52, 54–58).

- 2132 [124] ATLAS Collaboration. *ATLAS Pythia 8 tunes to 7 TeV data*. ATL-PHYS-PUB-2014-  
 2133 021. 2014. URL: <https://cds.cern.ch/record/1966419> (cit. on pp. 54–58).
- 2134 [125] S. Frixione, E. Laenen, P. Motylinski, and B. R. Webber. *Angular correlations of*  
 2135 *lepton pairs from vector boson and top quark decays in Monte Carlo simulations*.  
 2136 JHEP 04 (2007), p. 081. arXiv: [hep-ph/0702198](https://arxiv.org/abs/hep-ph/0702198) (cit. on p. 54).
- 2137 [126] P. Artoisenet, R. Frederix, O. Mattelaer, and R. Rietkerk. *Automatic spin-entangled*  
 2138 *decays of heavy resonances in Monte Carlo simulations*. JHEP 03 (2013), p. 015.  
 2139 arXiv: [1212.3460 \[hep-ph\]](https://arxiv.org/abs/1212.3460) (cit. on p. 54).
- 2140 [127] D. J. Lange. *The EvtGen particle decay simulation package*. Nucl. Instrum. Meth. A  
 2141 462 (2001), p. 152 (cit. on p. 54).
- 2142 [128] R. Frederix, D. Pagani, and M. Zaro. *Large NLO corrections in  $t\bar{t}W^\pm$  and  $t\bar{t}t\bar{t}$*   
 2143 *hadroproduction from supposedly subleading EW contributions*. JHEP 02 (2018), p. 031.  
 2144 arXiv: [1711.02116 \[hep-ph\]](https://arxiv.org/abs/1711.02116) (cit. on pp. 54, 79).
- 2145 [129] E. Bothmann et al. *Event generation with Sherpa 2.2*. SciPost Phys. 7.3 (2019), p. 034.  
 2146 arXiv: [1905.09127 \[hep-ph\]](https://arxiv.org/abs/1905.09127) (cit. on pp. 54, 55, 57).
- 2147 [130] S. Schumann and F. Krauss. *A parton shower algorithm based on Catani–Seymour*  
 2148 *dipole factorisation*. JHEP 03 (2008), p. 038. arXiv: [0709.1027 \[hep-ph\]](https://arxiv.org/abs/0709.1027) (cit. on  
 2149 pp. 54, 57, 58).
- 2150 [131] S. Höche, F. Krauss, M. Schönherr, and F. Siegert. *A critical appraisal of NLO+PS*  
 2151 *matching methods*. JHEP 09 (2012), p. 049. arXiv: [1111.1220 \[hep-ph\]](https://arxiv.org/abs/1111.1220) (cit. on pp. 54,  
 2152 57, 58).

- 2153 [132] S. Höche, F. Krauss, M. Schönherr, and F. Siegert. *QCD matrix elements + parton*  
 2154       *showers. The NLO case.* JHEP 04 (2013), p. 027. arXiv: [1207.5030 \[hep-ph\]](#) (cit. on  
 2155       pp. 54, 57, 58).
- 2156 [133] S. Catani, F. Krauss, B. R. Webber, and R. Kuhn. *QCD Matrix Elements + Parton*  
 2157       *Showers.* JHEP 11 (2001), p. 063. arXiv: [hep-ph/0109231](#) (cit. on pp. 54, 57, 58).
- 2158 [134] S. Höche, F. Krauss, S. Schumann, and F. Siegert. *QCD matrix elements and truncated*  
 2159       *showers.* JHEP 05 (2009), p. 053. arXiv: [0903.1219 \[hep-ph\]](#) (cit. on pp. 54, 57, 58).
- 2160 [135] F. Cascioli, P. Maierhöfer, and S. Pozzorini. *Scattering Amplitudes with Open Loops.*  
 2161       Phys. Rev. Lett. 108 (2012), p. 111601. arXiv: [1111.5206 \[hep-ph\]](#) (cit. on pp. 54,  
 2162       57, 58).
- 2163 [136] A. Denner, S. Dittmaier, and L. Hofer. *COLLIER: A fortran-based complex one-loop*  
 2164       *library in extended regularizations.* Comput. Phys. Commun. 212 (2017), pp. 220–238.  
 2165       arXiv: [1604.06792 \[hep-ph\]](#) (cit. on pp. 54, 57, 58).
- 2166 [137] F. Buccioni et al. *OpenLoops 2.* Eur. Phys. J. C 79.10 (2019), p. 866. arXiv: [1907.13071](#)  
 2167       [hep-ph] (cit. on p. 54).
- 2168 [138] S. Frixione, G. Ridolfi, and P. Nason. *A positive-weight next-to-leading-order Monte*  
 2169       *Carlo for heavy flavour hadroproduction.* JHEP 09 (2007), p. 126. arXiv: [0707.3088](#)  
 2170       [hep-ph] (cit. on pp. 55, 56, 58).
- 2171 [139] P. Nason. *A new method for combining NLO QCD with shower Monte Carlo algo-*  
 2172       *rithms.* JHEP 11 (2004), p. 040. arXiv: [hep-ph/0409146](#) (cit. on pp. 55, 56, 58).
- 2173 [140] S. Frixione, P. Nason, and C. Oleari. *Matching NLO QCD computations with parton*  
 2174       *shower simulations: the POWHEG method.* JHEP 11 (2007), p. 070. arXiv: [0709.2092](#)  
 2175       [hep-ph] (cit. on pp. 55, 56, 58).

- 2176 [141] S. Alioli, P. Nason, C. Oleari, and E. Re. *A general framework for implementing NLO*  
 2177 *calculations in shower Monte Carlo programs: the POWHEG BOX*. *JHEP* **06** (2010),  
 2178 p. 043. arXiv: [1002.2581 \[hep-ph\]](#) (cit. on pp. 55, 56, 58).
- 2179 [142] NNPDF Collaboration, R. D. Ball, et al. *Parton distributions with LHC data*. *Nucl.*  
 2180 *Phys. B* **867** (2013), p. 244. arXiv: [1207.1303 \[hep-ph\]](#) (cit. on pp. 55, 56, 58).
- 2181 [143] M. Bähr et al. *Herwig++ physics and manual*. *Eur. Phys. J. C* **58** (2008), p. 639.  
 2182 arXiv: [0803.0883 \[hep-ph\]](#) (cit. on p. 55).
- 2183 [144] J. Bellm et al. *Herwig 7.0/Herwig++ 3.0 release note*. *Eur. Phys. J. C* **76**.4 (2016),  
 2184 p. 196. arXiv: [1512.01178 \[hep-ph\]](#) (cit. on p. 55).
- 2185 [145] S. Alekhin, J. Blümlein, S. Klein, and S. Moch. *The 3-, 4-, and 5-flavor NNLO parton*  
 2186 *distribution functions from deep-inelastic-scattering data at hadron colliders*. *Physical*  
 2187 *Review D* **81**.1 (Jan. 2010). ISSN: 1550-2368. arXiv: [0908.2766 \[hep-ph\]](#) (cit. on  
 2188 pp. 55, 56).
- 2189 [146] ATLAS Collaboration. *Studies on top-quark Monte Carlo modelling for Top2016*.  
 2190 ATL-PHYS-PUB-2016-020. 2016. URL: <https://cds.cern.ch/record/2216168> (cit. on  
 2191 p. 56).
- 2192 [147] S. Frixione, E. Laenen, P. Motylinski, C. White, and B. R. Webber. *Single-top hadropro-*  
 2193 *duction in association with a W boson*. *JHEP* **07** (2008), p. 029. arXiv: [0805.3067](#)  
 2194 [\[hep-ph\]](#) (cit. on p. 56).
- 2195 [148] T. Gleisberg and S. Höche. *Comix, a new matrix element generator*. *JHEP* **12** (2008),  
 2196 p. 039. arXiv: [0808.3674 \[hep-ph\]](#) (cit. on p. 57).

- 2197 [149] C. Anastasiou, L. Dixon, K. Melnikov, and F. Petriello. *High-precision QCD at hadron*  
 2198       *colliders: Electroweak gauge boson rapidity distributions at next-to-next-to leading or-*  
 2199       *der.* Phys. Rev. D 69 (2004), p. 094008. arXiv: [hep-ph/0312266](#) (cit. on p. 57).
- 2200 [150] ATLAS Collaboration. *ATLAS data quality operations and performance for 2015–*  
 2201       *2018 data-taking.* JINST 15 (2020), P04003. arXiv: [1911.04632 \[physics.ins-det\]](#)  
 2202       (cit. on p. 59).
- 2203 [151] ATLAS Collaboration. *Analysis of  $t\bar{t}H$  and  $t\bar{t}W$  production in multilepton final states*  
 2204       *with the ATLAS detector.* ATLAS-CONF-2019-045. 2019. URL: <https://cds.cern.ch/record/2693930> (cit. on pp. 64, 69, 81).
- 2206 [152] ATLAS Collaboration. *Measurement of the total and differential cross-sections of  $t\bar{t}W$*   
 2207       *production in  $pp$  collisions at  $\sqrt{s} = 13 \text{ TeV}$  with the ATLAS detector.* JHEP 05 (2024),  
 2208       p. 131. arXiv: [2401.05299 \[hep-ex\]](#) (cit. on p. 64).
- 2209 [153] ATLAS Collaboration. *Search for new phenomena in events with same-charge leptons*  
 2210       *and  $b$ -jets in  $pp$  collisions at  $\sqrt{s} = 13 \text{ TeV}$  with the ATLAS detector.* JHEP 12 (2018),  
 2211       p. 039. arXiv: [1807.11883 \[hep-ex\]](#) (cit. on p. 69).
- 2212 [154] ATLAS Collaboration. *Search for  $R$ -parity-violating supersymmetry in a final state*  
 2213       *containing leptons and many jets with the ATLAS experiment using  $\sqrt{s} = 13 \text{ TeV}$*   
 2214       *proton–proton collision data.* Eur. Phys. J. C 81 (2021), p. 1023. arXiv: [2106.09609 \[hep-ex\]](#) (cit. on p. 72).
- 2216 [155] E. Gerwick, T. Plehn, S. Schumann, and P. Schichtel. *Scaling Patterns for QCD Jets.*  
 2217       JHEP 10 (2012), p. 162. arXiv: [1208.3676 \[hep-ph\]](#) (cit. on p. 72).
- 2218 [156] G. Avoni et al. *The new LUCID-2 detector for luminosity measurement and moni-*  
 2219       *toring in ATLAS.* JINST 13.07 (2018), P07017 (cit. on p. 74).

- 2220 [157] ATLAS Collaboration. *Tagging and suppression of pileup jets*. ATL-PHYS-PUB-2014-  
2221 001. 2014. URL: <https://cds.cern.ch/record/1643929> (cit. on pp. 75, 77).
- 2222 [158] ATLAS Collaboration. *Measurements of inclusive and differential fiducial cross-sections  
2223 of  $t\bar{t}$  production with additional heavy-flavour jets in proton–proton collisions at  $\sqrt{s} =$   
2224 13 TeV with the ATLAS detector*. JHEP 04 (2019), p. 046. arXiv: 1811.12113 [hep-ex]  
2225 (cit. on p. 79).
- 2226 [159] D. de Florian et al. *Handbook of LHC Higgs Cross Sections: 4. Deciphering the Nature  
2227 of the Higgs Sector*. CERN Yellow Rep. Monogr. 2 (2017), pp. 1–869. arXiv: 1610.  
2228 07922 [hep-ph] (cit. on p. 79).
- 2229 [160] ATLAS Collaboration. *Measurement of the production cross-section of a single top  
2230 quark in association with a Z boson in proton–proton collisions at 13 TeV with the  
2231 ATLAS detector*. ATLAS-CONF-2017-052. 2017. URL: <https://cds.cern.ch/record/2273868> (cit. on p. 79).
- 2233 [161] F. Demartin, B. Maier, F. Maltoni, K. Mawatari, and M. Zaro. *tWH associated  
2234 production at the LHC*. EPJC 77.1 (2017). arXiv: 1607.05862 [hep-ph]. URL: <https://doi.org/10.1140/epjc/s10052-017-4601-7> (cit. on p. 79).
- 2236 [162] ATLAS Collaboration. *Measurement of  $W^\pm Z$  production cross sections and gauge  
2237 boson polarisation in pp collisions at  $\sqrt{s} = 13$  TeV with the ATLAS detector*. Eur.  
2238 Phys. J. C 79 (2019), p. 535. arXiv: 1902.05759 [hep-ex] (cit. on p. 79).
- 2239 [163] G. Cowan, K. Cranmer, E. Gross, and O. Vitells. *Asymptotic formulae for likelihood-  
2240 based tests of new physics*. The European Physical Journal C 71.2 (Feb. 2011). ISSN:  
2241 1434-6052. arXiv: 1007.1727 [physics.data-an]. URL: <http://dx.doi.org/10.1140/epjc/s10052-011-1554-0> (cit. on p. 83).

- 2243 [164] J. Neyman and E. S. Pearson. *IX. On the problem of the most efficient tests of*  
2244 *statistical hypotheses.* Philosophical Transactions of the Royal Society of London.  
2245 Series A, Containing Papers of a Mathematical or Physical Character 231.694-706  
2246 (1933), pp. 289–337 (cit. on p. 83).
- 2247 [165] S. S. Wilks. *The large-sample distribution of the likelihood ratio for testing composite*  
2248 *hypotheses.* Annals of Mathematical Statistics 9.1 (1938), pp. 60–62 (cit. on p. 84).
- 2249 [166] T. Junk. *Confidence level computation for combining searches with small statistics.*  
2250 Nuclear Instruments and Methods in Physics Research Section A: Accelerators, Spec-  
2251 trometers, Detectors and Associated Equipment 434.23 (Sept. 1999), 435443. ISSN:  
2252 0168-9002. arXiv: [hep-ex/9902006 \[hep-ex\]](https://arxiv.org/abs/hep-ex/9902006) (cit. on p. 85).
- 2253 [167] A. L. Read. *Modified frequentist analysis of search results: The CLs method.* Tech.  
2254 rep. CERN-OPEN-2000-205. Presented at Workshop on Confidence Limits, Geneva,  
2255 Switzerland. CERN, 2000. URL: <https://cds.cern.ch/record/451614> (cit. on p. 85).
- 2256 [168] M. van Beekveld, A. Kulesza, and L. Moreno Valero. *Threshold Resummation for the*  
2257 *Production of Four Top Quarks at the LHC.* Phys. Rev. Lett. 131 (21 2023), p. 211901  
2258 (cit. on p. 97).
- 2259 [169] ATLAS Collaboration. *Preliminary analysis of the luminosity calibration of the AT-*  
2260 *LAS 13.6 TeV data recorded in 2022.* ATL-DAPR-PUB-2023-001. 2023. URL: <https://cds.cern.ch/record/2853525> (cit. on p. 97).